



UNIVERSITA' DEGLI STUDI DI PADOVA

FACOLTA' DI SCIENZE MM. FF. NN.
Dipartimento di Geoscienze
Direttore Prof. Fabrizio Nestola

TESI DI LAUREA MAGISTRALE
IN
GEOLOGIA E GEOLOGIA TECNICA

**THERMAL EVOLUTION OF PALEOZOIC AND
TRIASSIC RESERVOIR ROCKS IN THE
GHADAMES-ILLIZI BASIN (ALGERIA)**

Relatore: Prof. Massimiliano Zattin
Correlatore: Dott. Domenico Grigo

Laureanda: Ilaria Benvegnù
Matricola: 1206698

ANNO ACCADEMICO 2019/2020

Contents

Introduction	4
1 Geological Setting	6
1.1 Geographic Overview	6
1.2 Tectonic History	8
1.3 Stratigraphy	13
2 Petroleum Systems in the Ghadames-Illizi basin	25
2.1 Source Rocks	25
2.2 Reservoirs	26
2.3 Seal Rocks	27
2.4 Traps	27
2.5 Petroleum Systems	30
3 Materials and Methods	37
3.1 Thermal maturity	43
3.2 Thermochronology	45
3.3 Thermal modelling	53
4 Results	57
4.1 Maturity profiles of organic matter	57
4.2 Fission-track analysis and interpretation	65
4.3 U-Th/He analysis and interpretation	67

4.4 Constraints from both apatite FT and U-Th/He ages	68
4.5 Thermal modelling results	71
4.6 Discussion	82
5 Conclusions	84
References	86
Appendix	92

Introduction

The Ghadames-Illizi basin is one of the main petroleum systems of the North Africa platform, where 32 BBOE have been discovered by the oil industry in Paleozoic and Mesozoic reservoirs since the 1950s (Dixon et al., 2010). The Illizi basin contains more than 5000 million barrels of oil (Galeazzi et al., 2010) while 9500 million barrels of oil in place are present in the Ghadames basin (Echikh, 1998).

In that region it is still a matter of debate the possible thermal effects on the sedimentary successions of the Tertiary magmatic activity occurred in the neighbouring regions (e.g. Hoggar Dome; English et al., 2017) and its consequence on the petroleum system. This study, resulting from a collaboration with Eni s.p.a., therefore aims to provide new constraints to the reconstruction of the thermal history of the basin.

The work is based on experimental results derived from Vitrinite Reflectance, apatite fission-track analysis and apatite U-Th/He analysis, obtained from samples collected from some boreholes. These data, combined with information derived from stratigraphy of outcrops and subsurface, were used first to develop a burial history for the investigated sedimentary successions. Furthermore, different scenarios have been tested to verify the possible occurrence of a Tertiary thermal event. Despite the results are not fully conclusive (probably as a consequence of a bad definition of the present-day geothermal regime), this work shows the potentialities of such an integrated approach to the study of the thermal history in a sedimentary basin.

Chapter 1

Geological Setting

1.1 Geographic Overview

The Ghadames-Illizi basin is an intracratonic sag basin with a long subsidence and exhumation history which covers an area of about 400 000 km² (Dixon et al., 2010) and contains more than 6000 m of Palaeozoic and Mesozoic sediments (Echikh, 1998; Galeazzi et al., 2010).

The Ghadames-Illizi Basin is located in the North-African Platform, between Libya, Algeria and Tunisia and it is actually composed by two depocenters separated by a structural high. The Ghadames Basin is situated to the east of the Amguid-Hassi Touareg structural axis and south of the Telemzane-Gefara Arch while the eastern boundary is not well defined, being overlapped with the Sirt Basin (Echikh, 1998). The Illizi Basin is located more to the south, flanked by the Amguid-Hassi Touareg structural axis to the west, the Tihemboka Arch to the east and crops out to the south towards the Hoggar Massif (Boote et al., 1998). The southwest to northeast trending Amguid-Hassi Touareg structural axis is a fault and horst system which separates the Illizi basin from the Ahnet Province to the west. The Tihemboka Arch separates the Illizi from the Hamra basin to the east and it is near to the Algeria-Libyan boundary. The Arch does not divide the Ghadames and the Hamra basin, and they are somewhat continuous.

Furthermore, the Ghadames and Illizi basins are divided by a break into the basement rocks slope (Klett, 2000a-b).

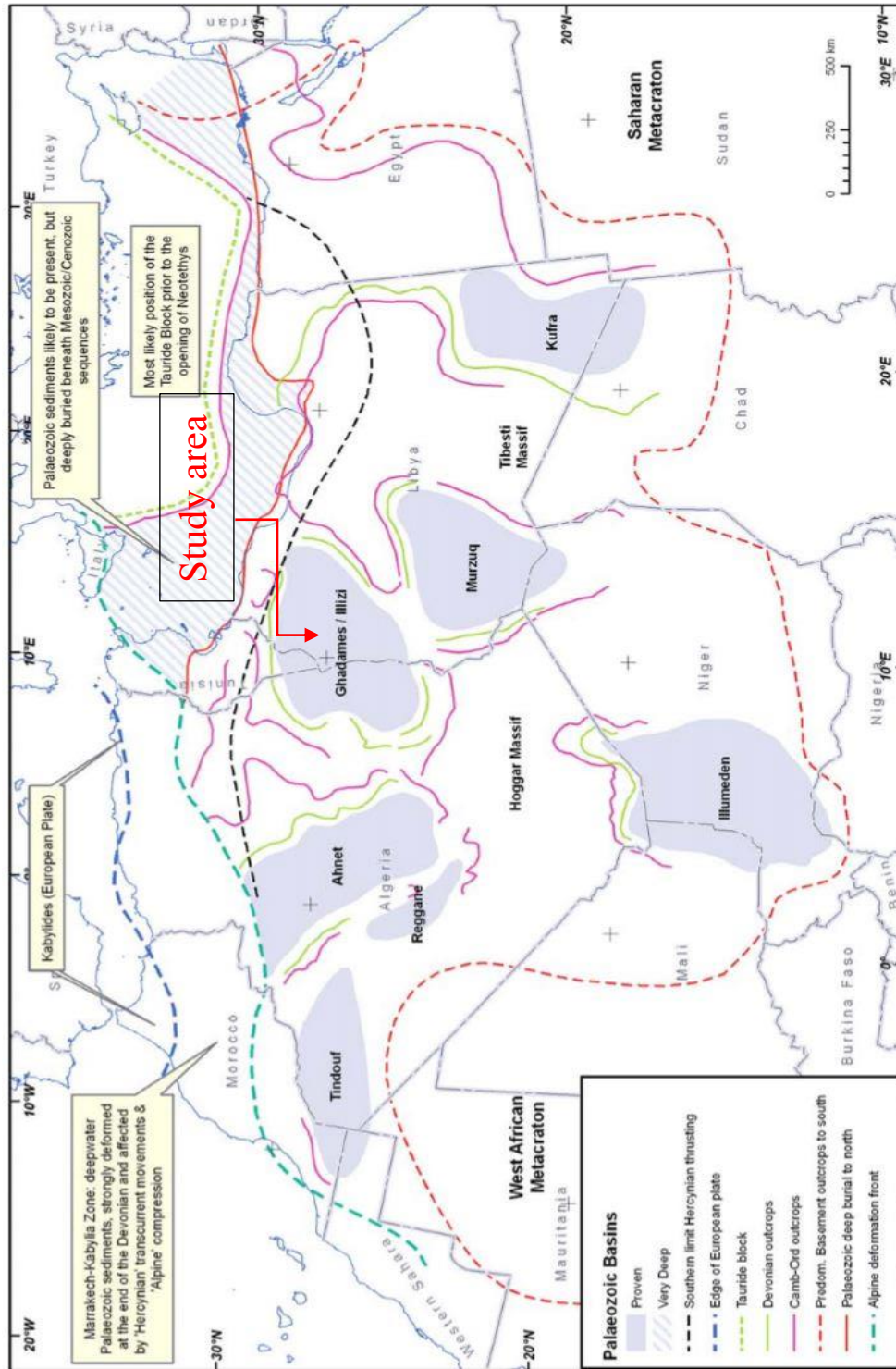


Figure 1.1: The Ghadames-Illizi basin and major tectonic elements (Dixon et al., 2010).

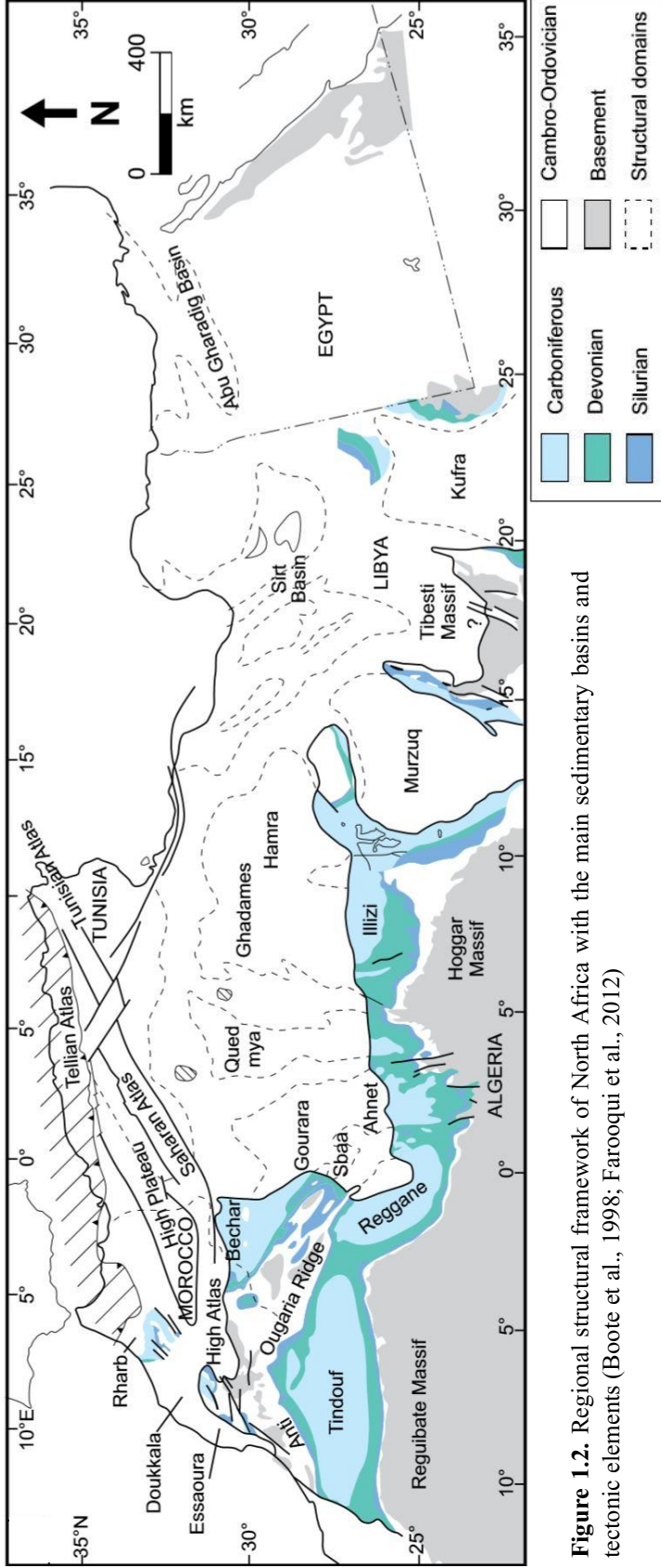


Figure 1.2. Regional structural framework of North Africa with the main sedimentary basins and tectonic elements (Boote et al., 1998; Farooqui et al., 2012)

1.2 Tectonic History

The present-day architecture of Ghadames-Illizi basin is the result of several tectonic events that modified the basin itself, altering the depocenter location (Underdown and Redfern, 2007), associated to a complex history of subsidence and exhumation which generated fault-bounded structural highs that surround a central depression (Underdown, 2007).

The tectonic history determined the petroleum generation, the hydrocarbon migration and the accumulation or the dispersion.

The main deformational events occurred during the Pre-Cambrian (Pan African event), Late Silurian to Early Devonian, Late Devonian (Frasnian event), Carboniferous to Permian (Hercynian event), Early Jurassic, Early Cretaceous (Aptian, Austrian event), Late Cretaceous, and Tertiary (Alpine event).

A classification of the tectonic structures is quite complex but they can be described into several groups (Echikh, 1998):

- Taconic phase: pre-Silurian structures
- Paleozoic structures developed until the Hercynian Orogeny
- Structures related to the Early Jurassic extensional movements
- Austrian phase: latest Barremian structures
- Alpine Tertiary structures

Before the Hercynian Orogeny the North African craton was a large and flat depositional basin (Van De Weerd and Ware, 1994) situated near the South Pole (Wang et al., 2019) and clastic sequences were deposited continuously across the whole region (English et al., 2017).

The Taconic Phase is a period characterized by tectonic instability which is testified by the absence of Cambrian sediments over the main uplifts (e.g. the Tihemboka Arch) and by the presence of volcanic layers related to the tectonic activity. These movements produced a series of overlapping deep erosional troughs and broad folds with active faulting controlling thickness and facies distribution (Echikh, 1998). In fact the Phanerozoic tectonic history is characterized by the Cambrian-Ordovician rifting and the Paleozoic basins developed overlying the rifts (Mann et al., 2005).

In the late Silurian and early Devonian Laurasia separated from Gondwana, resulting in segmentation and erosion of basins (Boote et al., 1998; Klett, 2000a-b). Moreover, in the late Silurian, minor uplift of the Tihemboka Arch and Amguid-Hassi Touareg structural axis, led the development of the Illizi as a discrete basin (Klett, 2000a).

Afterwards, in the late Devonian-early Carboniferous, collision of Laurasia and Gondwana began with consequently erosion and modification of the basin structures.

In the late Carboniferous, the collision between Gondwana and Laurentia (Hercynian Orogeny) and the subsequent closure of the paleo-Thetys Ocean caused uplift and intensive erosion of Paleozoic rocks along north-south trending arches, resulting in segmentation of the African Platform into different intracratonic sag and foreland basins (Klett, 2000a-b; Galeazzi et al., 2010; English et al., 2016). Hercynian erosion penetrate in some case as deep as the Cambrian sequence but a complete Paleozoic sequence is still preserved in the eastern Illizi Basin, even if the original thickness and the pre-Hercynian burial is unknown (English et al., 2016). The Hercynian unconformity separates folded Cambrian-Ordovician rocks from undeformed Permian-Triassic rocks and it can be seen both in the field and at regional seismic scale (Dixon et al., 2010). In addition, this event caused a widespread dispersion of the oil and gas trapped in a pre-Hercynian Petroleum System (Dixon et al., 2010).

After the Hercynian Orogeny, an extensional event, related to break up of Gondwana, the rifting of Tethys and the opening of the Atlantic, took place during the Triassic-Jurassic period. These event caused the reactivation of NNE to SSW trending Pan-African lineaments (Dixon *et al.*, 2010) and the establishment of en echelon normal faults, with associated extrusive volcanism, testified by variations in Triassic sediments thickness (Echikh, 1998). Triassic to Early Cretaceous sediments were deposited in a sag basin called “Triassic Basin” especially in Tunisia, Algeria and Libya (Mann et al., 2005).

It is important to point out that two major flooding events, one in the Silurian and one in the Devonian age, led the deposition of the two main source rocks of the

entire basin. Hydrocarbons were generated during the Carboniferous period within the basin depocenter and the subsequent uplift event brought the generation to an end. After the accumulation, an erosional event removed probably part of the petroleum deposit (Klett, 2000a-b).

After rifting, the area experienced a thermal subsidence stage until the Late Cretaceous, with the deposition of evaporitic and clastic sediments in the Late Triassic and Jurassic. Halite deposits accumulated at the centre of the basin whereas anhydrites with interbedded dolomites and shales were predominant at the edge of the basin. The evaporitic sequence represents therefore an important regional caprock for the underlying Triassic sediments (Dixon et al., 2010).

At the end of Barremian, during the lower Cretaceous, transpressional tectonic movements due to the Austrian phase occurred, proved by the presence of reverse faults along north-south trending existing lineaments (Echikh, 1998); the related unconformity separates the Upper Cretaceous and Paleocene rocks from the lower Cretaceous section. Margins uplifted and eroded during the Austrian phase, were re-buried during the later Cretaceous-early Cenozoic before a new uplift and exhumation event during the Alpine event in the Neogene as a consequence of the collision between Africa-Arabia and Europe (Ruth Underdown and Redfern, 2008). The actual Triassic basin configuration is the result of tilting and movements of the Alpine phase (Klett, 2000b).

The main unconformity yields a Miocene age and it is visible as an angular unconformity cut by some channels on a regional seismic scale. Furthermore the Late Cretaceous and Cenozoic sequences are probably folded due to the reactivation of basement faults in the final phases of the Alpine compression (Dixon et al., 2010).

The most important unconformities are related to the Hercynian and Alpine orogenies which separate the stratigraphic sequence into a Gondwana Supersequence (Paleozoic), followed by a Tethys Supersequence (Mesozoic), covered by an Alpine Supersequence (Tertiary) (Galeazzi et al., 2010).

As a matter of fact, the evolution of Gondwana and Pangea influenced the development of structures during the Paleozoic whereas the evolution of Tethys and

Mediterranean controlled tectonic events during the Mesozoic and Cenozoic (Hallett, 2002).

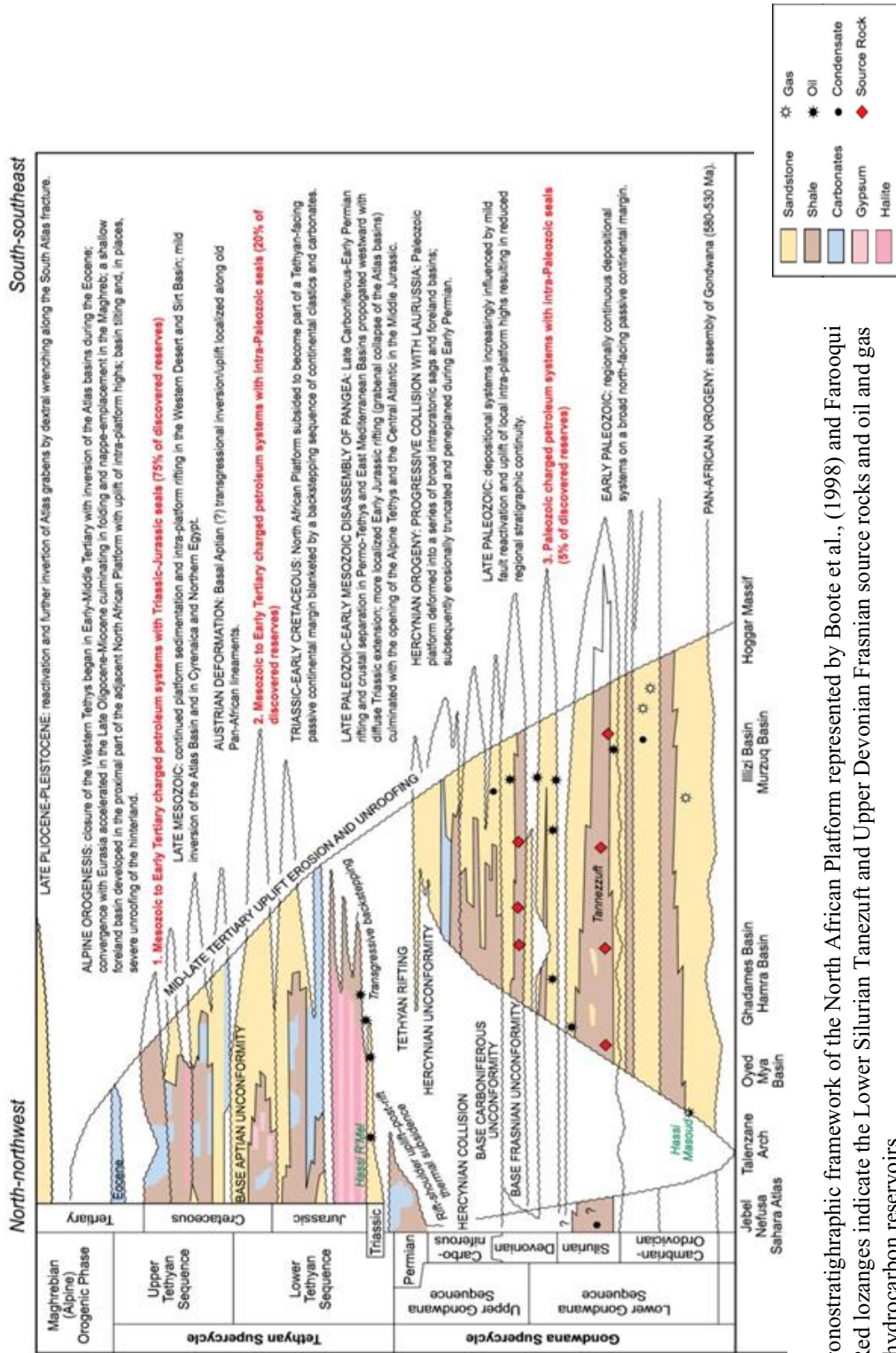


Figure 1.3: chronostratigraphic framework of the North African Platform represented by Boote et al., (1998) and Farooqui et al., (2012). Red lozanges indicate the Lower Silurian Tanezzuft and Upper Devonian Frasnian source rocks and oil and gas symbols show hydrocarbon reservoirs.

1.3 Stratigraphy

The Ghadames-Illizi stratigraphy can be described by dividing the stratigraphic column into supersequences, related to the major tectonic events: Hercynian and Alpine orogenesis.

Gondwana Supersequence: it is formed by up to 4000 m of clastic deposits (Galeazzi et al., 2010) and it covers the Paleozoic period until the Hercynian Orogeny. The Paleozoic succession can be divided itself into two Megasequences: a lower sequence from Cambrian to Silurian (which represents passive margin sedimentation) and an upper one from Devonian to Permian (representing the deposition during the collision between Gondwana and Laurasia) (Hallett, 2002).

-Lower Gondwana Cycle:

- *Hassaouna Formation (also Sidi Toui Fm. in Ghadames Basin; Hassi Leila Fm. or Unit II in Illizi Basin) (Cambrian):* it is separated from the Pan-African basement by the *Infratassilis Unconformity* and it is dominated by transgressive (Boote et al., 1998) medium to coarse-grained fluvial sandstones (Jabir et al., 2020).

Hassaouna Formation can be subdivided into three units. The lower unit is a conglomerate overlain by a cross-bedded sandstone with a clay matrix. The middle unit is fine-grained and siltier. Finally, the upper unit is composed of massive cross-bedded sandstones. This succession represents fluvial and deltaic environment in the lower part, with intertidal and subtidal conditions in the middle section and offshore bars in the upper part. (Hallett, 2002).

- *Ashebiat Formation (In Kraf Fm. or Unit III-1 In Illizi Basin) (Ordovician: Tremadocian):* shallow marine sandstone and maximum flooding shales (Boote et al., 1998) with dark gray silty sequences containing trace fossils representing a marine transgressive unit (Hallett, 2002).

System	Stage	Illizi Basin (van de Weerd and Ware, 1994)	Triassic Basin (Boudjema, 1987)	Ghadames (Berkiné) and Hamra Basins (Montgomery, 1994; Echikh, 1998)	General lithology (Boudjema, 1987)	
Carboniferous	Stephanian	F	Tiguentourine	Dembaba		
	Westphalian		El Adeb Larache			
	Namurian	E	Oubarakat	Assed Jeffar		
		D	Assekaifaf			
	Visean	C	Issendjel	Mrar		
		B				
Tournaisian	A	(Sbaa)				
Devonian	Strunian	F2	Gara Mas Melouki	Tahara (Shatti)		
	Famen - Frasnian	F3	Tin Meras	Aouinet Ouenine		
	Givetian - Eifelian			Ouan Kasa		
	Emsian			Orsine		
Siegenian - Gedinian	F6	Hassi Tabankort	Tadrart			
Silurian			Zone de Passage	Acacus		
		"Argileux"	Oued Imirhou	Tanezzuft		
		Gara Louki	Gres de Remada Argile Microogl.	Bir Tlacin		
Ordovician	Cardocian		Gres d'Oued Saret	Memouniat		
	Llandeilian - Llanvirnian	Edjeleh	M'Kraïta Complex	Argiles d'Azzel	Melez Chograne	
	Arenigian	Hamra		Gres de Ouargla	Haouaz	
			Quartzites De Hamra			
	Tremadocian	In Krafi	Gres d'El Atchane	Achebyat		
		Argile d'El Gassi				
Cambrian		Hassi Leila	Hassi Messaoud	Ro	Hassaouna and Mourizidie	
				R2		
				R3		
Infra-Cambrian			Socle	Infra Tassilian/ Mourizidie		

Fig. 1.4. Paleozoic stratigraphic section of Illizi, Triassic, and Ghadames Basins (from Boudjema, (1987) and Klett (2000). Major reservoir rocks are in yellow, source rocks in gray, and seals in red.

System	Stage	Illizi Basin (Chaouchi and others, 1998)	Triassic, Ghadames (Berkine), and Hamra Basins (Montgomery, 1994)	General lithology (Boudjema, 1987)	
Neogene	Pliocene				
	Miocene				
Paleog.	Oligocene				
	Eocene				
	Paleocene				
Cretaceous	Senonian	Calcaire	Al Hamra Group		
		Marnes			
		Calcaire			
			Argile Gypse		
	Turonian		Nefousa Group		
	Cenomanian	Serie D'In Akamil			
	Albian		Serie de Taouratine	Continental Intercalaire	
Barremian					
Neocomian					
Jurassic	Malm		Scesciuch (Shakshuk)		
	Dogger	Zarzaitine Superieur	Tigi		
	Lias	Zarzaitine Moyen	Saliferous Units		
Triassic		Zarzaitine Inferieur	Argilo-Greseux Superieur (Gassi Touil)		
			Argilo-Carbonate (Oulad Nair)		
			Argilo-Greseux Inferieur (Nezla)		

Fig. 1.5. Mesozoic-Cenozoic stratigraphic section of Illizi, Triassic, and Ghadames Basins (from Boudjema, (1987) and Klett (2000). Major reservoir rocks are in yellow, source rocks in gray, and seals in red.

- *Hawaz Formation (Hamra Fm or Unit III-2/3 in Illizi Basin) (Ordovician: Arenigian-Llandeilian):* basal transgressive lag above which there are repetitions of graptolitic shales and highstand sandstone facies, representing an alternation between tidal deposits and continental shelf strata (Boote et al., 1998; Jabir et al., 2020).

- *Melez Chograne Formation (basal Jefarah Fm. in Ghadames Basin and Edjeleh Fm or Unit III-3 in Illizi Basin) (Ordovician: Caradocian):* marine shales with interbedded sandstone, representing a flooding event (Jabir et al., 2020). There is evidence of subaqueous slumps, liquefaction and turbidity flows (Dardour et al., 2004) and brachiopods are present, thus indicating a cold water environment; that's the reason why the Melez Chograne Fm. represent a first major deglaciation event (Hallett, 2002).

The Taconian unconformity at the base of the Hawaz and the Melez Chograne Fms records the sea-level fall and testifies a reactivation of heterogeneities in the Pan-African basement (Boote et al., 1998; Galeazzi et al., 2012; English et al., 2016).

- *Memouniat Formation (upper Jefarah Fm in Ghadames Basin and Gara Louki Fm or Unit IV in Illizi Basin) (Ordovician: Ashgillian):* deposited at the end of the glacial cycle, when the North-African platform was near the South Pole, as the icecap retreated (Boote et al., 1998). The Memouniat Fm. consists of fine-grained sandstone and coarse-grained conglomeratic-sandstone representing a more proximal periglacial setting (Dardour et al., 2004) whereas the Jefarah Fm. contains of a carbonate sequence (Jabir et al., 2020). The Memouniat Fm. thus represents a basal lowstand system (Boote et al., 1998). Erosional features include glacial valleys and intra-valley channels.

- *Tanezuft Formation (Argileux or Silurian Argileux in Illizi Basin) (Silurian: Llandoveryan):* this succession is related to ice-sheet retreat and global sea-level rise (El Diasty et al., 2017) and corresponds to a transgressive system tract during which a layer of graptolitic black shales was deposited. The Tanezuft Fm. consists of dark micaceous siltstone with interbedded sandstone. In the lowermost part, this formation is also made by radioactive shales due to the

presence of uranium transported by wind as volcanic ash (Van De Weerd and Ware, 1994; Hallett, 2002); this particular rock is present also in surrounding basins such as the Sirte, Hamra and Berkine (Bora and Dubey, 2015). The lower Tanezuft Formation has a high content in organic matter (due to particular anoxic conditions (Wang et al., 2019) and is therefore an ideal source rock (Jabir et al., 2020) with a total organic carbon (TOC) content between 2% and 17% (Boote et al., 1998); hence it is one of the major source for the oil and gas reserves of the Paleozoic (Wang et al., 2019). The upper part is instead characterized by a thick siltstone member showing hummocky cross-stratification separated by hardgrounds, probably representing tempestite deposits (Hallett, 2002).

- *Acacus Formation (Lower F6 in Illizi Basin) (Silurian: Llandoveryan-Ludlovician)*: the Acacus Fm. consists of shelf-coastal/deltaic sandstones and mudstone deposited during the subsequent regression (Underdown, 2007; Jabir et al., 2020; Dardour et al., 2004). The formation is subdivided in a lower and an upper part, separated by a shale layer where the upper Acacus has a ferruginous top and contains plant remains, thus interpreted to be a continental deposit (Hallett, 2002). This Silurian sands are a fair to good reservoir with porosities between 10 and 15% and permeability of 100 mD (Echikh, 1998). These sediments are truncated by the Caledonian unconformity which separates the Silurian deposits from the Devonian succession.

- *Tadtrat Formation (Upper F6 in Illizi Basin) (Devonian: Lochkovian-Pragian)*: lowstand system characterized by continental fluvial medium to coarse sandstones and mudstones that constitute one of the main reservoir in the Ghadames-Illizi basin (Underdown, 2007; Jabir et al., 2020; Boote, David et al., 1998). The sheet sands are cut by sand filled-channels with a good porosity (Hallett, 2002).

- *Ouan Kasa Formation (F5-F4 in Illizi Basin) (Devonian: Emsian)*: succession accumulated during the first stage of a new transgression (Dardour et al., 2004) in a shallow marine environment consisting of fine to medium sandstone, siltstone and dolomites (Boote et al., 1998; Underdown et al., 2007;

Jabir et al., 2020) with subtidal facies variations and alternations of sands, silts and shales (Echikh, 1998).

-*Upper Gondwana Cycle*: determined by collision between Gondwana and Laurasia.

- *Aouinet Ouenine Formation (F3 in Illizi basin) (Devonian: Eifelian-Famennian)*: it resulted from a marine transgression and divided into four cycles (I to IV) of alternating shale, siltstone and sandstone corresponding to the stage Eifelian, Givetian, Frasnian, Famennian. The lower part of the sequence is made up of neritic to coastal deltaic cycles (Dardour et al., 2004). In the Illizi basin, the Givetian age is characterized by the deposition of the F3 sandstones which reflect a barrier island environment and are a good reservoir in the area (Galeazzi et al., 2012). Concerning the petroleum exploration, the uppermost part of Aouinet Ouenine Fm. III (Frasnian) is important because in Ghadames-Illizi Basin corresponds to an organic-rich level, due to particular highstand conditions including rise of the sea level and a warmer climate, which is considered a significant source rock with TOC value ranging between 2% and 14% (Boote et al., 1998; Riboulleau et al., 2018; Jabir et al., 2020).
- *Tahara Formation (F2 in Illizi basin) (Devonian: Strunian)*: sandstone and shales representing shallow marine and deltaic conditions with continental influences. These sandstones are considered a good reservoir in the basin (Underdown, 2007; Jabir et al., 2020).
- *M'rar Formation (B and C members in Illizi basin) (Carboniferous: Tournaisian-Visean)*: fluvial-dominated deltaic formation characterized by a sequence of silty shales and sandstone with interbedded siltstone and limestone. It comprises a basal conglomerate, which becomes more wave-dominated in the uppermost part (Boote et al., 1998; Hallett, 2002; Jabir et al., 2020). In the Illizi area, B and C can be considered as good reservoirs members (Galeazzi et al., 2012).

- *Asadjefar Formation (D and E members in Illizi basin) (Carboniferous: Namurian)*: the lower part of the sequence consists of fluvio-deltaic sandstone, siltstone and dolomitic limestone deposition overlain by marine shales and stromatolitic limestones which reflected a changing in conditions from deltaic to shallow marine environment (Boote et al., 1998; Jabir et al., 2020).
- *Dembaba Formation (F member in Illizi basin) (Carboniferous: Namurian-Westphalian)*: shallow marine carbonates and evaporites deposition with intercalated sandstones containing brachiopods and fusulinid foraminifera (Jabir et al., 2020), divided into two members: the lower member is made up of gypsiferous claystone with beds of limestone, marl and calcarenite while the upper one comprises dolostones, limestones and calcarenites. The Dembaba Fm. represents an oil and gas reservoir (Shaltami et al., 2019).
- *Tiguentourine Formations (Upper F member in Illizi basin) (Carboniferous: Stephanian)*: this formation represents the last Paleozoic regressive event before the Hercynic orogeny and the subsequent erosion of most of the African craton and it has been interpreted to be the result of restricted marine-lagoonal environment which led the deposition of red-brown dolomitic shales, shaly dolomites and anhydrite (Hallett, 2002; Jabir et al., 2020).

Thetyan Supersequence: it is formed by a thick succession of Mesozoic-Tertiary clastic, evaporitic and carbonate sediments deposited within a “Triassic Basin” associated with a generalised extensional regime due to the opening of the Tethys Ocean (Boote et al., 1998; Galeazzi et al., 2010).

-Lower Thethyan Cycle: it is related to the rifting along the northern margin of the African plate during the early Triassic and records the breakup of Gondwana and the initial opening of the Tethys Ocean; extensional faulting controlling the sediment thickness and determined extrusive volcanic activity developed in the northern part of the Ghadames basin (Boote et al., 1998; Galeazzi et al., 2010; Dixon et al., 2010; English et al., 2017).

- *Triassic Argilo-greseux Inferieur (TAGI) Formation (lower Zarzaitine Inferieur Fm. in Illizi basin) (Triassic: Ladinian-Carnian)*: the basal unit above the Hercynian unconformity was deposited in a braided fluvial system. It is given by sand continental deposits characterized by quartz-arenite that grades into sub-arkosic sandstones with excellent reservoir properties due to good primary porosity and minor diagenesis. (Boote et al., 1998; Klett, 2000; Galeazzi et al., 2010). According to Galeazzi et al. (2010), the TAGI Fm. has permeability of 1 Darcy and porosity over 20%.
- *Triassic Argilo-carbonate (TAC) Formation (middle Zarzaitine Inferieur Fm. in Illizi basin) (Triassic: Carnian)*: it covers and seals the TAGI Fm. and is made of lacustrine and shallow marine shales with interbedded carbonates and anhydrite beds (Klett, 2000; Underdown, 2007; Galeazzi et al., 2010).
- *Triassic Argilo-greseux Superior Formation (TAGS) (upper Zarzaitine Inferieur Fm. in Illizi basin) (Triassic: Norian-Rhetian)*: fluvial deposits in the southern part of the basin which change facies from sandstones to interbedded sandstones and siltstones (as terminal fans and floodplain with crevasse splays), to silty shales with anhydrite facies, to salt deposits to the north (Galeazzi et al., 2010). In the Ghadames-Illizi basin, this formation is made of mudstone, siltstone and fine to medium-grained sandstones and some volcanic rocks are also present (Boudjema, 1987; Van De Weerd and Ware, 1994; Klett, 2000).
- *Triassic Argilo-salifere (Zarzaitine Moyen Fm. in Illizi basin) (Upper Triassic-Jurassic: Lias)*: Triassic-Jurassic transgressive marine mudstone and carbonates and regressive evaporites with cyclic sequences of alternating salt, anhydrite, gypsum, dolostone form a regional seal for the underlying Triassic reservoir rocks (Boudjema, 1987; Van De Weerd and Ware, 1994; Klett, 2000; Underdown and Redfern, 2008; Bora and Dubey, 2015).
- *Tigi Group and Shakshuk Formation (Zarzaitine Supérieur Fm. in Illizi basin) (Jurassic: Dogger-Malm)*: the Upper Jurassic is characterized by an

alternation of coastal plain and deltaic sandstones and mudstones, with shallow marine to lacustrine shales dolomites associated with anhydrite layers (Klett, 2000; Galeazzi et al., 2010; Tlig, 2015).

- *Cabao and Continental Intercalaire Formations (Taouratine Fm. in Illizi basin) (Early Cretaceous)*: this interval includes the Cabao Fm (Neocomian) and the Continental Intercalaire (Barremian) and is characterized by the deposition of coarse-grained continental sandstones, specifically sandstones with quartz pebbles and red clays in the Cabao Fm. The Continental Intercalaire is marked on top by the Austrian unconformity (Aptian) due to an east-west transpressional and strike-slip movement that produced high-amplitude structures (Echikh, 1998; Klett, 2000; Galeazzi et al., 2010; Galushkin et al., 2014; Tlig, 2015). At the top of the sequence, after the Austrian unconformity, deposition of a transgressive thin dolostone layer occurred (Aptian) (Klett, 2000).

-*Upper Thethyan Cycle*: it starts above the erosional event, during the upper Cretaceous

- *Nefousa Group (upper Taouratine Fm in Illizi basin) (Cretaceous: Albian)*: the upper Taouratine Fm. is characterized by the deposition of continental and shallow marine coarse-grained sandstones and mudstones with sporadic intercalations of dolostones (Boudjema, 1987; Klett, 2000; Tlig, 2015).
- *Sidi as Sid Formation (Cretaceous: Cenomanian)*: this transgressive formation comprises two members, constituted by mudstones, evaporites and shallow-marine carbonates (Boudjema, 1987; Hallett, 2002; Bodin et al., 2010; Galushkin et al., 2014). These carbonates were deposited in an embayment of the Neo-Tethys (Sahagian, 1988).
- Above Cretaceous deposits Miocene-Pliocene continental sands are present on an erosive contact called “Alpine unconformity”. In fact, much of the Upper Cretaceous to Oligocene section has been eroded during the Alpine (or Pyrenean) deformation specially in the Libyan part of the basin, where

also Miocene-Pliocene deposits are rarely present. The Alpine unconformity is associated to the Alpine orogenic event and is the result of the collision between Africa-Arabia and Europe during the Upper Cretaceous-Eocene (Klett, 2000; Underdown, 2007; Underdown and Redfern, 2008; Bora and Dubey, 2015).

Moreover, during the Eocene-Oligocene, calc-alkaline magmatic activity in the North Africa area caused uplift and the development of some topographic swells, such as the Hoggar dome (Wilson and Guiraud, 1992; English et al., 2017). This magmatic activity could explain the over-maturation of the reservoir rocks in the Ghadames-Illizi basin.

Chapter 2

Petroleum Systems in the Ghadames-Illizi Basin

The Ghadames-Illizi basin is characterized by the presence of various petroleum systems related to the presence of two main source rocks (Silurian and Devonian) associated to Paleozoic and basal Triassic reservoir intervals and sealed by Paleozoic shales or Triassic-Liassic evaporites.

The Tanezuft and Frasnian shales achieved very high maturities values thanks to an increasing in overburden and to elevated heat flow probably associated to the Hercynian volcanic activity (Boote et al., 1998).

A lot of petroleum was generated at this time but much of the oil was dissipated with the subsequent Hercynian erosional event that led almost residual gas accumulations.

When migration occurred, it was both lateral and vertical. Long lateral migration was encouraged by regional sandstone continuity whereas fault-related vertical migration was important along structural axes (Boote et al., 1998).

It is important to point out that the petroleum systems were affected by meteoric invasion caused by tilting and erosion during mid to late Tertiary orogeny which increased water flow through Paleozoic and Triassic aquifers. Thus, part of the petroleum systems (mostly in the south of the basin) was dispersed by remigration and flushing (Boote et al., 1998).

2.1. Source Rocks

The Silurian Tanezuft Formation and Middle to Upper Devonian mudstone are the most important Paleozoic source rocks on the North African Platform. Both were deposited during flooding events which led the accumulation of sediments over Cambro-Ordovician topography, creating a series of anoxic basins (Boote et al., 1998; Macgregor, 1996; Klett, 2000a,b). Their present distribution is the result of the Hercynian deformation.

Silurian kerogen is principally of type II with TOC values average from 0,5 to 8% but exceptionally reach 17% while Devonian TOC ranges between 2-8% but can reach 14% and kerogen is type I and II (Klett, 2000a,b; Hallett, 2002; Hrouda, 2005).

Oil generation, both from Silurian and Devonian source rocks, began during the Carboniferous but was halted by the Hercynian uplift and the erosion removed probably all the oil generated until the Hercynian event (Daniels and Emme, 1995; Klett, 2000a,b; Hallett, 2002). The following Mesozoic subsidence allowed a second Silurian oil generation pulse during the middle Cretaceous period in the northern part of the basin and in the late Jurassic in the central portion. A second peak of oil generation for the Devonian rocks was reached during the Eocene in the central part of the petroleum system and in the Cretaceous period in the eastern and northern area (Klett, 2000a,b; Hallett, 2002).

According to Daniels and Emme (1995), Tanezuft and Devonian source rocks decrease their maturity toward the basin margin.

In the Ghadames basin, vitrinite reflectance (Ro) of the Silurian rocks ranges from 1.1 to 2% while in the Illizi basin is from 1.1 to 1.3%. Middle to Upper Devonian rocks yield Ro values from 1.1 to 1.3% in the Ghadames-Illizi basin (Daniels and Emme, 1995).

2.2 Reservoirs

The Ghadames-Illizi province is characterized by the presence of different reservoir intervals whose quality depends on facies, age and diagenesis.

Known reservoirs are Cambrian-Ordovician, Devonian, Silurian, Carboniferous and Triassic sandstones. Cambrian-Ordovician reservoirs include fluvial sandstone of the Hassi Leila Fm., Hawaz Fm and its laterally equivalent Hamra Fm. and marine and glacial sandstones of the Memouniat Fm. Late Cambrian sandstone has porosities below than 10% and permeabilities of 10 mD whereas Hamra quartzites are productive where fractured or where affected by secondary porosity (Galeazzi et al., 2012).

Devonian reservoirs are sandstone of F2, F3, F4, F5 and F6 members in the Illizi basin (laterally equivalent of Tahara Fm., Ouan Kasa Fm, Tadrat Fm., and Acacus Fm. in the Ghadames basin). The Acacus Fm is an important reservoir in the eastern part of the Ghadames basin. F6 sandstones are good reservoirs in particular in the Illizi basin.

Carboniferous reservoir are B and D sandstone members found in the M'rar Fm. and in the Asadjefar Fm.

Triassic reservoirs include TAGI and TAGS sandstones mostly in the Ghadames basin. TAGI reservoir properties are excellent with good primary porosity and less diagenesis: permeability values of over 1 Darcy are reached and porosities are over than 20% (Galeazzi et al., 2012).

2.3 Seal Rocks

Different seal rocks, depending on the erosional events, are present in the area.

Tanezuft and Devonian mudstones act as seal themselves for Cambro-Ordovician and lower Devonian reservoirs. Their local erosion allowed the migration of hydrocarbons to lower or higher reservoir systems (Boote et al., 1998).

In fact, Paleozoic mudstones can act as primary seals mostly in the Illizi petroleum system whereas seal rocks in the Ghadames petroleum system is characterized by Triassic to Jurassic evaporites, mudstones and carbonate rocks (Boote et al., 1998; Klett, 2000-b; Klett, 2000-a; Hallett, 2002).

2.4 Traps

Traps in the Ghadames-Illizi basin are mainly structural and stratigraphic, particularly beneath the Hercynian unconformity. Echikh (1998) described the different type of traps in the Ghadames-Illizi basin:

- *Structural traps:* The most important oil accumulations are found into structural traps produced by a complex structural history which led the development of different traps of different ages.

Typical structural traps are simple anticline of pre-Hercynian age which forms low-relief structures mainly in the northwest Libya and in the central part of the Ghadames basin. These traps were formed in the Silurian and Devonian periods during the Caledonian and Frasnian events.

Normal and reverse faulted structures can act as structural traps too. The first were formed during the Hercynian deformational event, related to vertical movements of the basement. Instead, the second type of faults was produced during compressional Austrian and Alpine events.

In addition, uplifted faulted blocks of Liassic extensional movements produced structural traps.

- *Stratigraphic traps*: essentially two types of stratigraphic traps can be found in the Ghadames-Illizi area. These can be pinch-out traps or stratigraphic truncations. This trap type is present only in north-western part of Libya where hydrocarbons are trapped in the Acacus reservoir below Triassic strata.

Furthermore, structural and stratigraphic combination traps can occur such as in Libya where both rapid facies changes in Acacus Fm. and structural structures contribute to the entrapment of hydrocarbons.

- *Diagenetic traps*: in the Tiguentourine field in the Illizi basin, a lateral seal due to an increased quartzification, provides an example of permeability barrier in the area.
- *Hydrodynamic traps*: formed by the movement of interstitial fluids known in the Late Silurian-Early Devonian pools.

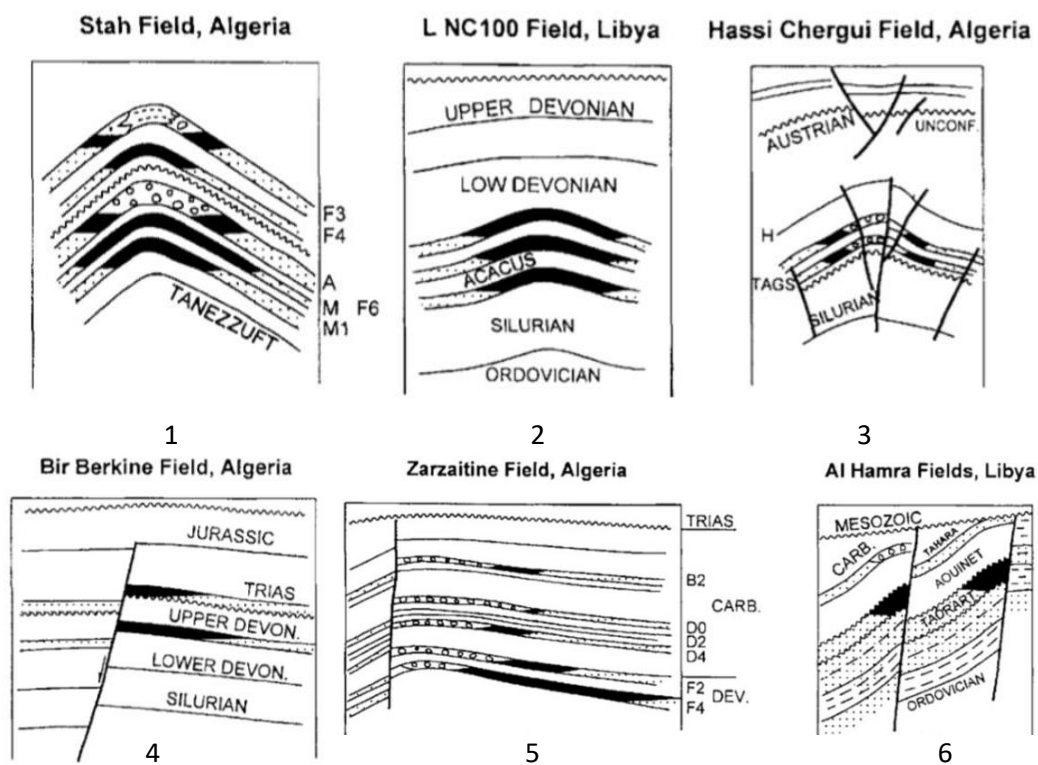
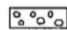



Figure 2.1: Sketch sections of structural and stratigraphic traps from Echikh (1998): 1,2 simple anticlines; 3,6 reverse faults from Austrian and Alpine events; 4 normal faults of Triassic-Jurassic age; 5 normal fault structure from Hercynian event.

 Gas
 Oil

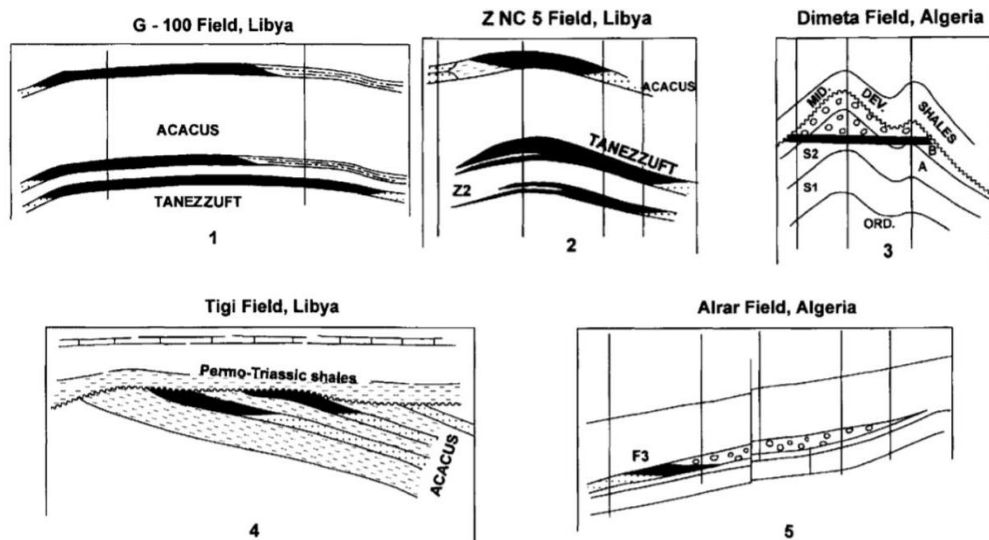




Figure 2.2: Sketch of different trap combinations and stratigraphic traps from Echikh (1998): 1,2 structural traps and pinch-out; 3 unconformity trap; 4 subcrop trap; 5 pinch-out trap.

 Gas
 Oil

2.5 Petroleum Systems

Four main Petroleum Systems are recognized in the Illizi basin: a Cambro-Ordovician system charged by the Lower Tanezuft Fm., a Devonian system charged by the Tanezuft shales and an Upper Devonian-Lower Carboniferous system charged by Frasnian shales (Boote et al., 1998).

- *Lower Tanezuft-Cambro/Ordovician System:* the Tanezuft shale varies in the basin from 200 to 500 m in thickness. To the north, the lowest part of the formation is more organically rich and therefore is the source of petroleum in the underlying Cambro-Ordovician reservoir (Boote et al., 1998).

TOC values vary from less than 2% in the east, to 4% in the north and 8% in the west while maturities (R_o) range from 1.1% in the central part of the basin, to 1.75% in the southwest and northeast. Higher values can be reached in the basin due to magmatic intrusions (Daniels and Emme, 1995). The Tanezuft Fm. is also an important seal for Cambro-Ordovician reservoirs (porosities between 7-14% and permeabilities up to 250 mD). Their lateral continuity allowed a long-distance lateral and updip migration to the west, southwest and south during Mesozoic and Early Tertiary (Boote et al., 1998; Hallett, 2002).

- *Tanezuft-Lower Devonian F6, F*: it is the most important petroleum system within the Ghadames-Illizi basin (Hallett, 2002).

Hydrocarbons were generated in the Tanezuft Fm. and in the overlying Acacus Fm. The combination guaranteed a very prolific source rock system thanks to their thickness, regional extent and a very efficient primary migration. The source rock was deeply buried during the Carboniferous and Mesozoic and in the gas window during the Cenozoic; most of the oil was generated from source rocks on the flank of the basin (Hallett, 2002).

Migration brought hydrocarbons into Devonian reservoirs along conduits within the rocks. The stratigraphic continuity allowed a long distance lateral migrations to the west and the southwest into the F6 reservoir rock (porosities of 18-25% and permeabilities of few darcies). However, the overlying shale seal was eroded along the flank of the Tihemboka Arch and thus the oil migrated updip into the F4 reservoir unit (Boote et al., 1998; Hallett, 2002). In addition, on the northern part of the Ghadames basin, the Devonian sequence is truncated by the Hercynian unconformity, which produced a stratigraphic trap with the overlying Permo-Triassic shales.

During the Cenozoic, the Petroleum System observed a water flushing from the south of the basin which affected the oil accumulation and produced both hydrodynamic and structural traps (Boote et al., 1998; Hallett, 2002).

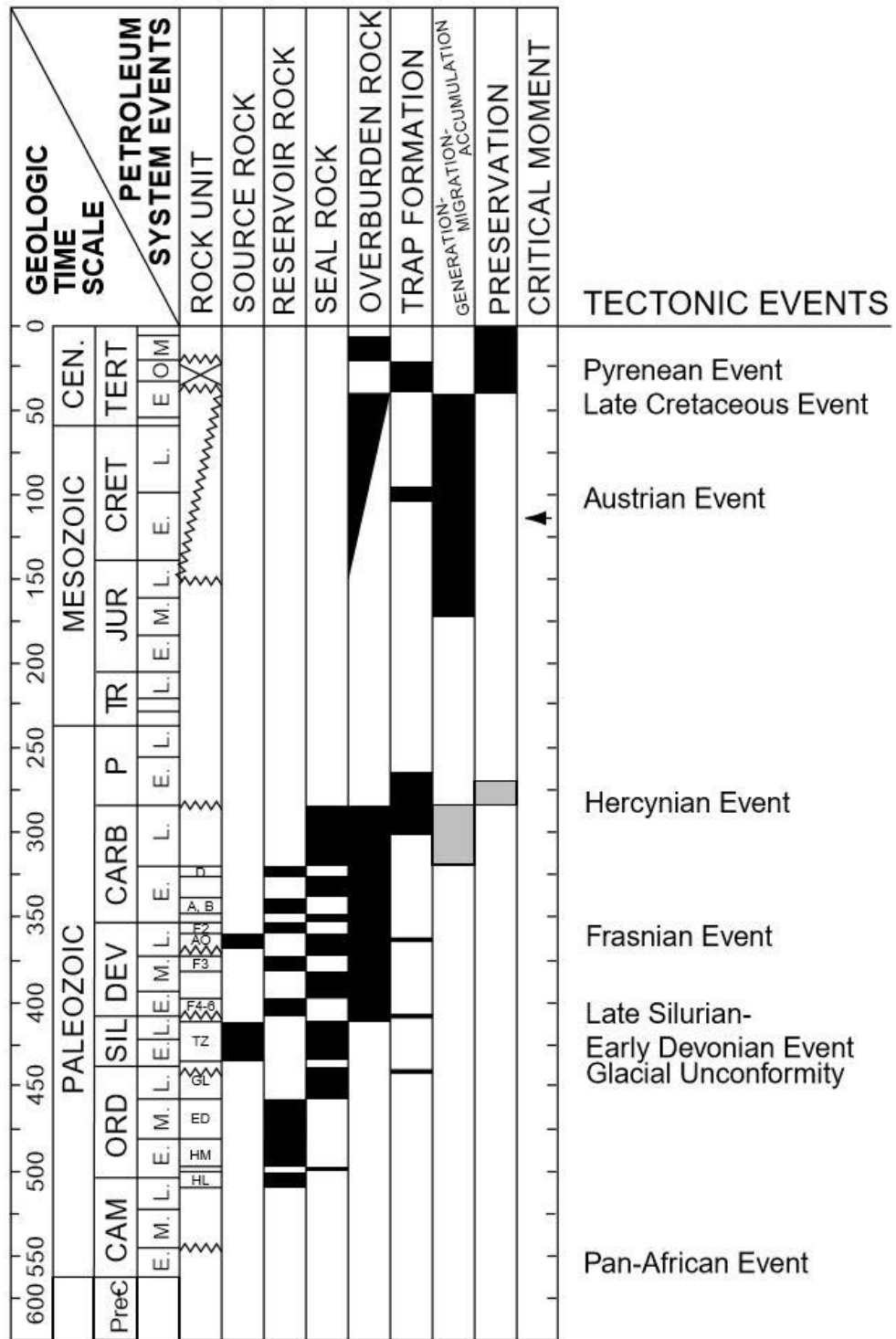


Figure 2.3. Event Chart of the Illizi basin from Klett (2000a). Formation name abbreviations are: A, B, D Lower Carboniferous sandstone members; AO Aouinet Ouenine mudstone; ED Edjeleh sandstone; F2, F3, F4, F5, F6 Devonian sandstone members; GL Gara Louki sandstone and mudstone; HM Hamra sandstone; HL Hassi Leila sandstone; TZ Tanezuft mudstone.

- *Frasnian to Upper Devonian-Carboniferous*: the Frasnian shales vary in thickness between 25 to 110 m thinning locally under structural highs. TOC ranges between less than 2% in the southeast to 4-6% in the north and the west while the maturity starts from 1.1% in the central part and increases to 1.3% in the north-eastern depocenter (Boote et al., 1998).

Oil expulsion charged Upper Devonian and Lower Carboniferous reservoirs such as the F2 sandy member, Tahara sandstones and M'rar Fm. sandy layers. Porosity values are from 15 to 22% in the F2 member, with permeabilities of 50-300 mD while Tahara and Carboniferous sandstones have poorer reservoir qualities.

Lateral migration along structural axes was dominant but on the flank of the Tihemboka Arch, the basin experienced also a vertical migration through Austrian faults.

Hydrodynamic flushing after mid-Tertiary uplift had a less influence on this Petroleum System (Boote et al., 1998; Hallett, 2002).

- *Tanezuft-Triassic and Frasnian-Triassic*: these Petroleum Systems are mainly present in the Ghadames basin. They are described by Boudjema, (1987), Daniels and Emme, (1995) and Boote et al., (1998).

Both Tanezuft and Frasnian source rocks charged Triassic sands, sealed by Triassic to Liassic shales and evaporites.

A shaly Triassic basal facies separates the Tanezuft-Triassic Petroleum system in the northwest and the Frasnian-Triassic Petroleum system in the central part of the basin.

Triassic sands were charged from the section underlying the unconformity, both from the subcropping shales and through Devonian sands.

The basal Tanezuft Fm. is the organically richest layer, characterized by type I-II kerogen and TOC value of 17%. It experienced a peak expulsional event during the upper Cretaceous and early Triassic.

Hydrocarbons migrated in the TAGI reservoir which is characterized by forming a conduit that favoured lateral migration toward the south.

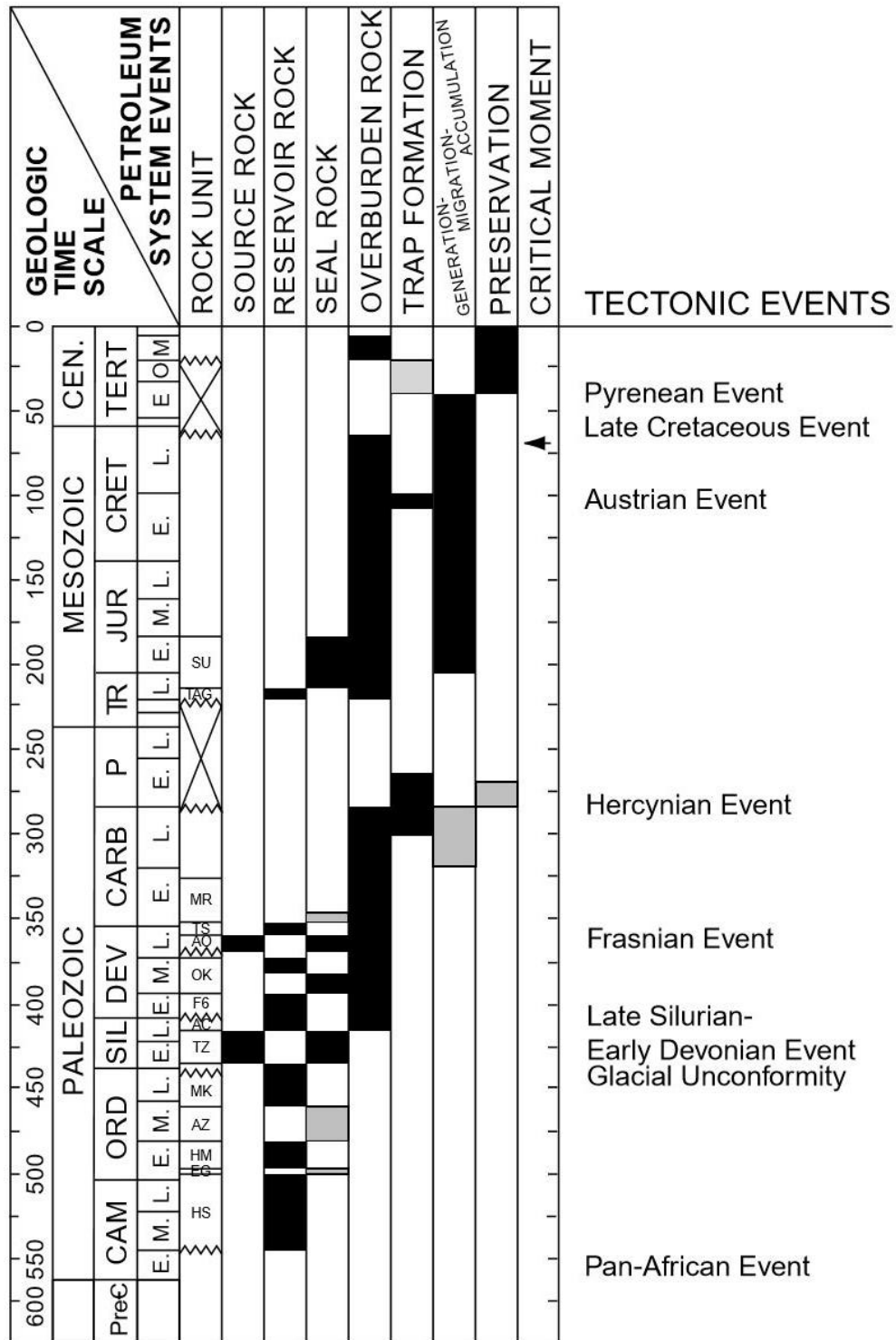


Fig. 2.4.: Event Chart of the Ghadames basin from Klett (2000a). Formation name abbreviations are: AC Acacus sandstone; AO Aouinet Ouenine mudstone; AZ Argiles D’Azzel; SU Saliferous Units; EA Gres D’El Atchane sandstone; EG Argile D’El Grassi; F6 Devonian sandstone members; HM Hamra sandstone; HS Hassaouna sandstone; MK M’Kratra sandstone and mudstone; MR M’rar mudstone and sandstone; OK Ouan Kasa mudstone and sandstone; TAG sandstone; TS Tahara sandstone; TZ Tanezuft mudstone.

Frasnian basal Fm. has value of 8-14% TOC of oil-prone type I-II kerogen and the hydrocarbon expulsion followed a lateral and vertical migration pattern.

Two Triassic reservoirs are present in the Petroleum system: TAGI and TAGS sand members.

In addition, the Frasnian-sourced accumulations were not affected by late Tertiary tilting; therefore, it is guaranteed a trap integrity to the present days.

As a consequence, the system is extremely prolific.

Chapter 3

Materials and Methods

In this thesis work, samples from three wells drilled by Eni in North Africa have been analysed.

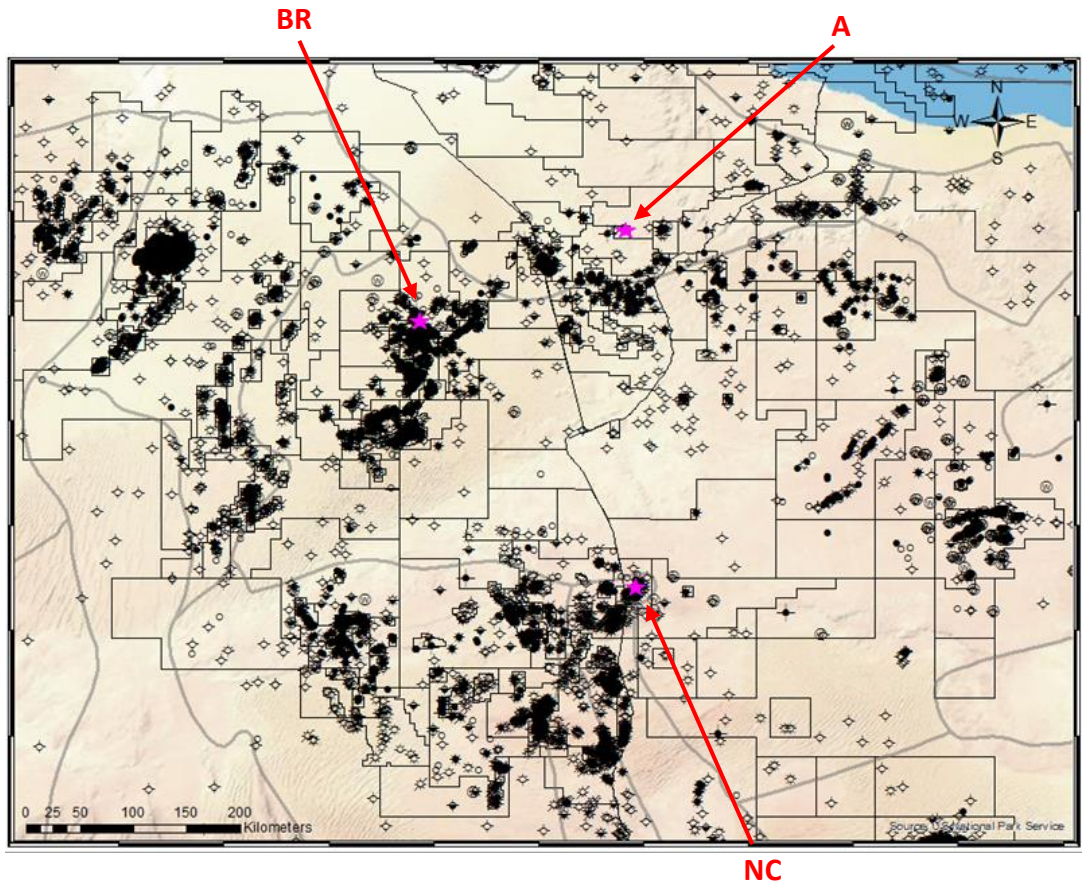


Fig. 3.1. Wells location.

For each well, several investigations on samples have been conducted in order to determine different parameters which characterize the well itself.

Furthermore, samples suitable to apatite fission track and U-Th/He analysis were selected. As a whole, 14 crystals have been prepared for the apatite U-Th/He dating and, since fission track analysis requires a significant number of apatite grains, it has been possible to date only two samples with this technique.



Fig. 3.2. Samples collection at Eni's laboratories



Fig. 3.3. Example of sample. It is reported the short well name and its depth.



Fig 3.4. Core collection example of a well A core at Eni's laboratories. It is reported the depth.

Well	Sample	Depth	Stratigraphic age	(U-Th)/He	AFT
A	S2	2229.5	Middle Trias	X	X
	S3	2240.7	Middle Trias	X	X
BR	B3	3014	Triassic	X	
NC	A2	2612-2617	Middle Devonian	X	

Tab. 3.1. Details of sampled materials for low-T thermochronology analysis

HYDRO_PRES_(Atm)	LITHO_PRES_(Atm)	PRES_(Atm)	DEPTH_(M)	DIMS_(m)	TEMP_(C)	POROS_(%)	COND_(CAL/S*CM*C)	RO%_BURNI	gradP_(MPa/m)	gradT_(C/Km)	Layer
304.463	709.677	304.463	-2711.76	3049.9	104.435	0.102506	0.00486634	0.784078	1.00455	26.4875	1
300.387	700.127	300.387	-2670.66	3008.8	103.347	0.102506	0.00486634	0.773455	1.00455	26.4875	1
300.387	700.127	300.387	-2670.66	3008.8	103.347	0.220099	0.00399402	0.773455	1.00474	32.1013	2
290.967	678.059	290.967	-2575.69	2913.83	100.298	0.220099	0.00399402	0.748947	1.00474	32.1013	2
290.967	678.059	290.967	-2575.69	2913.83	100.298	0.05	0.00661261	0.748947	1.00491	19.5114	3
285.325	664.843	285.325	-2518.81	2856.95	99.1882	0.05	0.00661261	0.741351	1.00491	19.5114	3
285.325	664.843	285.325	-2518.81	2856.95	99.1882	0.111241	0.00411031	0.741351	1.00496	31.4113	4
283.335	660.181	283.335	-2498.75	2836.89	98.5581	0.111241	0.00411031	0.737123	1.00496	31.4113	4
283.335	660.181	283.335	-2498.75	2836.89	98.5581	0.114809	0.00409479	0.737123	1.00516	31.5523	5
271.113	631.562	271.113	-2375.58	2713.72	94.6718	0.114809	0.00409479	0.708304	1.00516	31.5523	5
271.113	631.562	271.113	-2375.58	2713.72	94.6718	0.249882	0.00440417	0.708304	1.00586	28.5386	6
227.442	529.367	227.442	-1935.77	2273.91	82.1202	0.249882	0.00440417	0.617922	1.00586	28.5386	6
227.442	529.367	227.442	-1935.77	2273.91	82.1202	0.192306	0.00462042	0.617922	1.00709	26.5287	7
161.558	375.382	161.558	-1273.07	1611.21	64.5396	0.192306	0.00462042	0.478157	1.00709	26.5287	7
161.558	375.382	161.558	-1273.07	1611.21	64.5396	0.285337	0.00457002	0.478157	1.00908	26.3512	8
35.0888	80.3749	35.0888	-3.46027	341.602	31.0839	0.285337	0.00457002	0.313025	1.00908	26.3512	8
35.0888	80.3749	35.0888	-3.46027	341.602	31.0839	0.384358	0.00359132	0.313025	1.01078	32.7492	9
8.15374	17.6507	8.15374	266.483	71.659	22.2434	0.384358	0.00359132	0.289935	1.01078	32.7492	9
8.15374	17.6507	8.15374	266.483	71.659	22.2434	0.411371	0.00379838	0.289935	1.01128	31.307	10
1	1	1	338.142	0	20	0.411371	0.00379838	0.201897	1.01128	31.307	10

Tab. 3.2. Well A simulated data. From left to right are reported: hydrodynamic pressure, lithological pressure, pressure, depth and depth to zero, temperature, porosity, thermal conductivity, Vitrinite Reflectance, pressure and temperature gradient and the well layer.

PRES. (Atm)	DEPTH. (M)	DIMS. (m)	TEMP. (C)	POROS. (I)	COND. (CAL/S*CM*C)	RO%_BURN(I)	gradP. (MPa/m)	gradT. (C/Km)	Layer
331.492	-2700.3	3329.68	139.469	0.089237	0.00425115	1.61873	0.999562	34.9136	1
330.614	-2691.4	3320.78	139.159	0.089237	0.00425115	1.60849	0.999562	34.9136	1
330.614	-2691.4	3320.78	139.159	0.091225	0.00424209	1.60849	0.999714	35.0067	2
322.459	-2608.77	3238.15	136.266	0.091225	0.00424209	1.51971	0.999714	35.0067	2
322.459	-2608.77	3238.15	136.266	0.214469	0.00433612	1.51971	1.00044	33.6661	3
286.983	-2249.56	2878.94	124.173	0.214469	0.00433612	1.23013	1.00044	33.6661	3
286.983	-2249.56	2878.94	124.173	0.232226	0.00423956	1.23013	1.00144	33.8514	4
264.132	-2018.41	2647.79	116.348	0.232226	0.00423956	1.07613	1.00144	33.8514	4
264.132	-2018.41	2647.79	116.348	0.240375	0.00419597	1.07613	1.00188	33.9593	5
261.633	-1993.14	2622.52	115.49	0.240375	0.00419597	1.05711	1.00188	33.9593	5
261.633	-1993.14	2622.52	115.49	0.124105	0.00409517	1.05711	1.00202	36.5447	6
256.232	-1938.54	2567.92	113.495	0.124105	0.00409517	1.00927	1.00202	36.5447	6
256.232	-1938.54	2567.92	113.495	0.126159	0.00408616	1.00927	1.00216	36.6404	7
254.026	-1916.24	2545.62	112.678	0.126159	0.00408616	0.99011	1.00216	36.6404	7
254.026	-1916.24	2545.62	112.678	0.129561	0.00474515	0.99011	1.00234	31.5298	8
243.882	-1813.72	2443.1	109.445	0.129561	0.00474515	0.924088	1.00234	31.5298	8
243.882	-1813.72	2443.1	109.445	0.180618	0.00392182	0.924088	1.00522	38.4866	9
104.424	-408.355	1037.74	55.3574	0.180618	0.00392182	0.417247	1.00522	38.4866	9
104.424	-408.355	1037.74	55.3574	0.281148	0.00388829	0.417247	1.00813	33.6712	10
94.2645	-306.266	935.65	51.9199	0.281148	0.00388829	0.397646	1.00813	33.6712	10
94.2645	-306.266	935.65	51.9199	0.327419	0.0041091	0.397646	1.00927	32.2503	11
29.9465	339.292	290.092	31.1005	0.327419	0.0041091	0.308509	1.00927	32.2503	11
29.9465	339.292	290.092	31.1005	0.393981	0.00338286	0.308509	1.01081	38.2654	12
1	629.384	0	20	0.393981	0.00338286	0.201897	1.01081	38.2654	12

Tab. 3.3. Well NC simulated data. From left to right are reported: pressure, depth and depth to zero, temperature, porosity, thermal conductivity, Vitrinite Reflectance, pressure and temperature gradient and the well layer.

HYDRO_PRES_(Atm)	LITHO_PRES_(Atm)	PRES_(Atm)	DEPTH_(M)	DIMS_(m)	TEMP_(C)	POROS_(I)	COND_(CAL/S*CM*C)	RO%_BURNI)	PERMX_(DARCY)	PERMY_(DARCY)	PERMZ_(DARCY)	gradP_(MPa/m)	gradT_(C/Km)	Layer
477.843	1116.03	477.843	-4597.33	4798.72	140.297	0.05	0.00443559	1.56584	2.89E-10	2.89E-10	4.82E-12	1.00232	27.7302	1
475.745	1111.11	475.745	-4576.13	4777.52	139.709	0.05	0.00443559	1.54838	2.89E-10	2.89E-10	4.82E-12	1.00232	27.7302	1
475.745	1111.11	475.745	-4576.13	4777.52	139.709	0.05	0.00443559	1.54838	2.89E-10	2.89E-10	4.82E-12	1.00244	27.7471	2
466.611	1089.66	466.611	-4483.83	4685.22	137.148	0.05	0.00443559	1.47984	2.89E-10	2.89E-10	4.82E-12	1.00244	27.7471	2
466.611	1089.66	466.611	-4483.83	4685.22	137.148	0.0541209	0.0052154	1.47984	2.79E-09	2.79E-09	2.60E-11	1.00315	23.6824	3
391.434	913.263	391.434	-3724.68	3926.07	119.17	0.0541209	0.0052154	1.07202	2.79E-09	2.79E-09	2.60E-11	1.00315	23.6824	3
391.434	913.263	391.434	-3724.68	3926.07	119.17	0.0730407	0.00509366	1.07202	1.72E-08	1.72E-08	1.60E-10	1.00411	24.3671	4
350.709	817.797	350.709	-3313.83	3515.22	109.158	0.0730407	0.00509366	0.87715	1.72E-08	1.72E-08	1.60E-10	1.00411	24.3671	4
350.709	817.797	350.709	-3313.83	3515.22	109.158	0.0834738	0.00502775	0.87715	3.88E-08	3.88E-08	3.61E-10	1.00456	24.7396	5
340.003	792.712	340.003	-3205.87	3407.26	106.487	0.0834738	0.00502775	0.841251	3.88E-08	3.88E-08	3.61E-10	1.00456	24.7396	5
340.003	792.712	340.003	-3205.87	3407.26	106.487	0.0890539	0.00425365	0.841251	9.63E-09	9.63E-09	1.60E-10	1.00485	29.325	6
324.621	756.68	324.621	-3050.8	3252.19	101.94	0.0890539	0.00425365	0.783494	9.63E-09	9.63E-09	1.60E-10	1.00485	29.325	6
324.621	756.68	324.621	-3050.8	3252.19	101.94	0.0950828	0.00495541	0.783494	8.58E-08	8.58E-08	7.98E-10	1.00515	25.1604	7
312.708	728.782	312.708	-2930.74	3132.13	98.9192	0.0950828	0.00495541	0.754265	8.58E-08	8.58E-08	7.98E-10	1.00515	25.1604	7
312.708	728.782	312.708	-2930.74	3132.13	98.9192	0.099393	0.00492882	0.754265	1.12E-07	1.12E-07	1.05E-09	1.00533	25.3159	8
305.683	712.334	305.683	-2859.95	3061.34	97.1271	0.099393	0.00492882	0.740147	1.12E-07	1.12E-07	1.05E-09	1.00533	25.3159	8
305.683	712.334	305.683	-2859.95	3061.34	97.1271	0.142285	0.00460292	0.740147	0.000368288	0.000368288	6.41E-06	1.00608	24.4126	9
233.243	542.855	233.243	-2130.57	2331.96	79.321	0.142285	0.00460292	0.595017	0.000368288	0.000368288	6.41E-06	1.00608	24.4126	9
233.243	542.855	233.243	-2130.57	2331.96	79.321	0.21409	0.00480634	0.595017	0.00757101	0.00757101	0.000135197	1.00781	23.1465	10
106.355	246.502	106.355	-855.168	1056.56	49.7999	0.21409	0.00480634	0.382603	0.00757101	0.00757101	0.000135197	1.00781	23.1465	10
106.355	246.502	106.355	-855.168	1056.56	49.7999	0.295081	0.00381368	0.382603	0.0356522	0.0356522	0.000620038	1.00931	28.2598	11
68.7941	158.905	68.7941	-478.182	679.569	39.1464	0.295081	0.00381368	0.338556	0.0356522	0.0356522	0.000620038	1.00931	28.2598	11
68.7941	158.905	68.7941	-478.182	679.569	39.1464	0.365353	0.00388993	0.338556	0.231573	0.231573	0.00413523	1.01057	28.1743	12
1	1	1	201.387	0	20	0.365353	0.00388993	0.201897	0.231573	0.231573	0.00413523	1.01057	28.1743	12

Tab. 3.4. Well BR simulated data. From left to right are reported: hydrodynamic pressure, lithological pressure, pressure, depth and depth to zero, temperature, porosity, thermal conductivity, Vitrinite Reflectance, Permeability along x, y and z axes, pressure and temperature gradient and the well layer.

3.1. Thermal maturity

Vitrinite Reflectance, denoted by R_o (Reflectance of oil), is an indicator of the maximum temperature reached by the rocks (Scotti, 2005; Allen and Allen, 2013). This is a useful optical parameter for the thermal history reconstruction of a basin as it strictly depends on the temperature.

Vitrinite is one of the primary components of coals and other organic matter found in the sedimentary rocks; it is a lignin maceral and it forms by thermal alteration of cellulose component of plant tissues (Allen and Allen, 2013). Vitrinite Reflectance thus records the maximum temperature that a rock has experienced since burial. Under the microscope it appears translucent, with a colour ranging from light to dark brown.

The Vitrinite Reflectance is a measure of the percentage of light reflected by the sample: the higher is the temperature achieved, the higher is the reflectance. In fact, with the increase in temperature, there is a reorganization of the organic matter in the fragments which leads to an even higher capacity for reflection.

Depending on the calculated R_o value, the maturity of the source can be determined: for $R_o < 0,55\%$ the source rock is immature, for R_o between $0,55-0,80\%$ the source is in the stage of oil and gas generation, for R_o between $0,80-1,0\%$ the source is in the oil and gas cracking stage (field of gas-condensate) and for R_o between $1,0-2,5\%$ the source experienced dry gas generation (Allen and Allen, 2013). In a range of R_o between $0,6-1,35\%$ the temperature corresponds to about 120°C and the source rock is considered to be in the “oil window” with a mature kerogen, while if $R_o > 1\%$ is in the “gas window” with a high maturity kerogen (Allen and Allen, 2013).

Samples are washed, dried and treated with strong acids (HCl 37% and HF 40%) to destroy the organic matter. After washing samples with distilled water, they are mounted on resin for vitrinite reflectance analysis. These resin mounts are polished and then analysed in reflected light using oil immersion objectives.

The reflectance of all vitrinite fragments is calculated and a mean value of $R_o\%$ is assigned for each sample.

In addition, a part of each sample is mounted on a slide for kerogen composition analysis after filtering, centrifugation and treatment with ZnCl₂ and KOH used for breaking the organic matter. Slides are then analysed in transmitted light until the kerogen type and the qualitative thermal maturity are defined thanks to the colour of palynomorphs (spores and pollens) (Thermal Alteration Index - TAI).

From light yellow to dark yellow indicates an immature kerogen; light brown - brown indicates the “oil window”; dark brown indicates the “gas window”; black indicates an over mature kerogen (Scotti, 2005).

TAI index supports the vitrinite method in indicating thermal maturity of the sample.

Maturation rank		Paleo Temp. (¹) (°C)	Microscopic parameters					Chemical parameters			
Kerogen	Coal		Vitrinite Reflectance (Ro %)	TAI (²)	SCI (²)	CAI	Fluorescence of alginite	T _{max}	Biomarker Isomerization Sterane Hopane		Hydrocarbon main products
Immature	Peat	50	0.2	1 Yellow	1	1 Yellow	Bue-green	420	0,10	0,10	Immature heavy oil (³)
	Lignite		0.3				Greenish-yellow				
	Sub-bituminous Coal		0.4				Golden yellow				
Mature Very Mature High Maturity	Bituminous Coal	100	0.5 – 0.55	2 Orange	3 4 5 6	2 Light brown	Dull yellow	430	0,50	0,50	Oil (³) and wet gas
			0.7				Orange				
			0.8				Orange				
			1.0				Orange				
			1.35				Orange				
			1.5				Orange				
Overmature	Semi Anthracite	150	1.35	3 Brown	7 8	3 Brown	Red	465	None	None	Wet gas
			1.5				Red				
Organic Methamorphisme	Anthracite	200	2.0	4 Brown/Black	9	4 Dark brown	Nonfluorescent	500	None	None	Dry gas
			2.5								
			3.0								
	Meta Anthracite	250	4.0	5 Black	10	5 Black	Nonfluorescent	None	None	None	Dry gas
			5.0								

Fig. 3.5. Chart by Scotti (2005) regarding the correlation between the most important organic maturity parameters. TAI: Thermal Alteration Index. SCI: Spore Colour Index is a colour scale for spores. CAI: Conodont Alteration Index is a colour scale for Conodonts. Fluorescence of alginite changes as the maturity level increase.

3.2 Thermochronology

The thermal sensitivity of a radioactive system depends on its ability to turn from a closed to an open system with the increasing temperatures. Thermochronometry is an important tool for the sensitivity to a low temperature range with the purpose of providing an evaluation of the thermal history of a sedimentary succession.

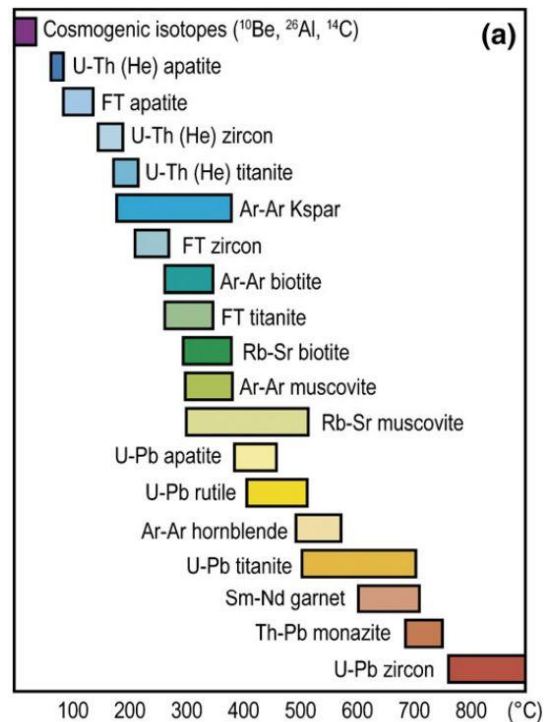


Fig. 3.6. Nominal closure temperatures of various geochronometers and thermochronometers in current use (Cloetingh et al., 2007)

In this study, fission track (AFT) and U-Th/He (AHe) analysis are carried out on clastic apatite grains. Both AFT and AHe methods are based on the radioactive decay of a parent nuclide (basically U and Th) and the accumulation of the daughter product (effect of the fission on the crystal lattice or a nuclide) with the aim of dating the cooling age of a mineral. The cooling age is defined in relation with the effective closure temperature (T_c) of the system, which is the temperature of the rock at its thermochronometric cooling age.

- *Fission track analysis* give information both on temperature of burial and on time of exhumation (Zattin et al, 2002). This technique is based on the accumulations of damage trails in the apatite crystals due to the spontaneous radioactive fission of ^{238}U present in trace in the minerals (Zattin et al., 2005; Allen and Allen, 2013). When a heavy unstable nucleus decays by spontaneous fission it splits into two nuclear fragments which are pushed away to each other by a combination of energy released by the nuclear fission and Coulomb repulsion forces. The fission of ^{238}U produces a damaged zone in the crystal lattice, known as “fission tracks”, which have the same initial length of about 16 μm .

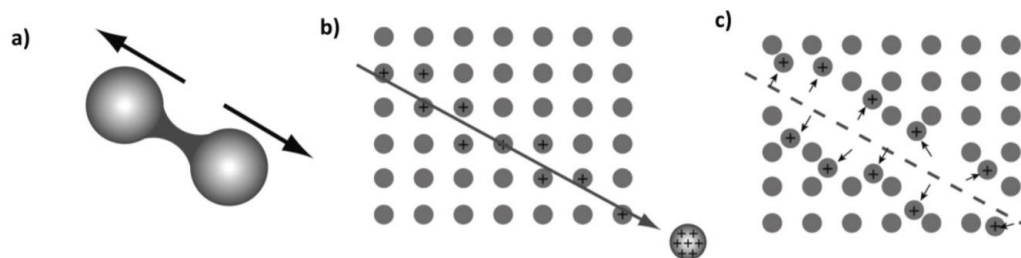


Fig. 3.7. Model for fission tracks formation. a) the heavy nucleus splits into two segments. b) being the two segments positively charged, they pushed away from each other. In this phase they attract electrons from the atoms of the lattice. c) atoms positively charged along the line dislocate from the lattice position due to their repulsive force

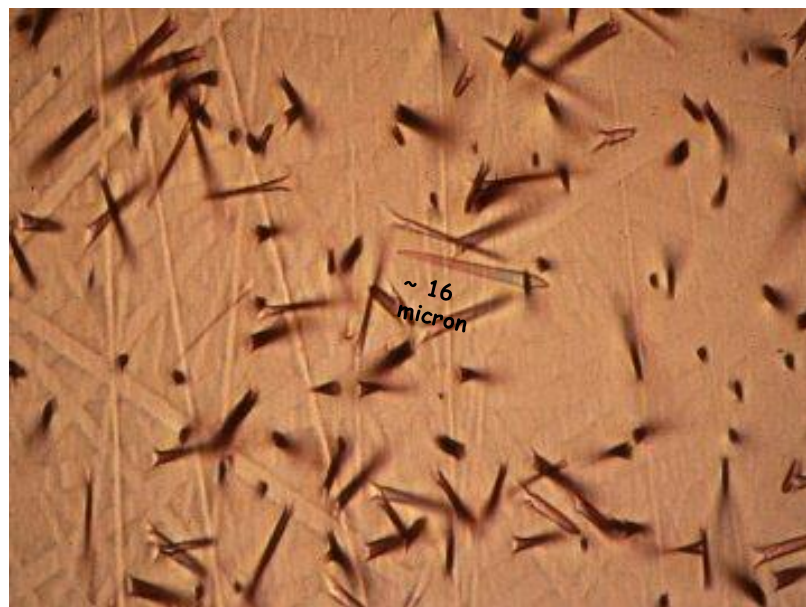


Fig. 3.8. Apatite fission track indicating no annealing. From www.geotrack.com.au

The equation that describe fission tracks accumulation with time is:

$$Ns = \frac{\lambda_F}{\lambda_D} {}^{238}\text{N}(e^{\lambda_D t} - 1)$$

where N_s is the number of spontaneous fission tracks per unit volume, ${}^{238}\text{N}$ is the number of ${}^{238}\text{U}$ atoms per unit volume, λ_F and λ_D are the decay constants for spontaneous nuclear fission and α -decay of ${}^{238}\text{U}$ ($\lambda_F = 8,5 \times 10^{-17} \text{ yr}^{-1}$ and $\lambda_D = 1,5 \times 10^{-10} \text{ yr}^{-1}$) (Tagami and O'Sullivan, 2005)

The fission track density reflects the time since the crystal last cooled sufficiently to retain fission damage and the lengths of the fission tracks reflect the temperatures the crystal experienced during that time.

The AFT age is calculated with the following formula:

$$AFT \text{ age} = \frac{1}{\lambda_d} \ln(1 + \lambda_d \zeta g \rho_d \frac{\rho_{s,i}}{\rho_{i,i}})$$

where λ_d is the total decay constant, ζ is a calibration factor depending on the microscope, the reactor and the operator, g is the geometry factor for spontaneous fission track registration, ρ_d is the induced fission track density for a uranium standard corresponding to the sample position during neutron irradiation, $\rho_{s,i}$ is the spontaneous fission track density for grain i , $\rho_{i,i}$ is the induced fission track density for the grain i (Donelick et al., 2005).

Linear tracks start to be preserved in the crystal lattice below 125°C where the system can be considered closed. Above this temperature, fission tracks disappear (anneal) and partial annealing of fission tracks occurs at temperatures between 60° and 125°C (Gleadow et al, 1986), interval known as “partial annealing zone” (PAZ), where fission tracks get shorter according to the degree and duration of heating (Zattin et al., 2002). Therefore, with greater depths, fission tracks decrease due to the amount of annealing at elevated temperatures (Allen and Allen, 2013). At greater depth and at higher temperatures, fission tracks should be totally annealed and AFT ages should be zero (Ketcham, 2005).

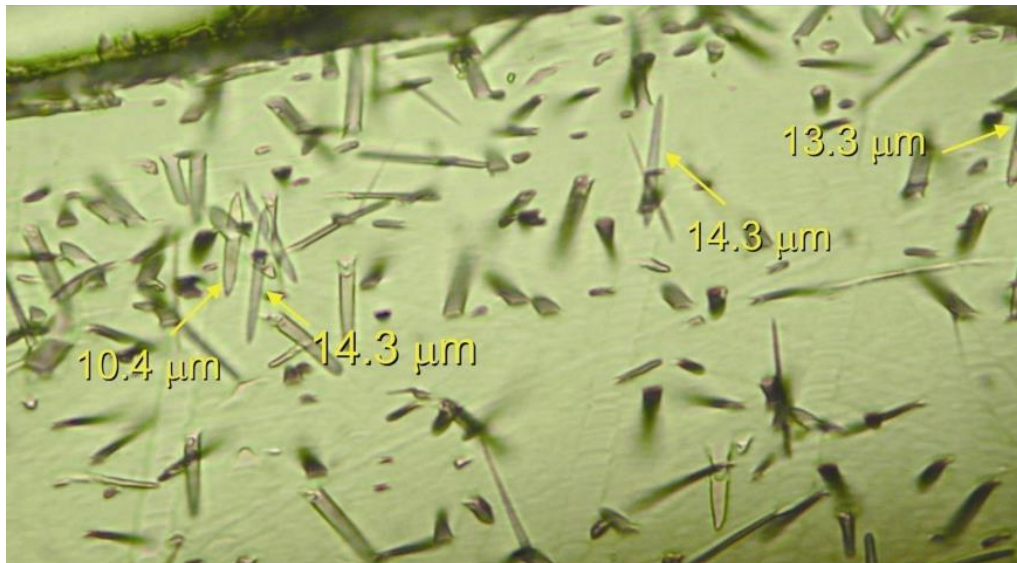


Fig. 3.9. AFT with different lengths. Short tracks are older than long tracks.

AFT analysis are important because this range of annealing temperatures (PAZ) corresponds with hydrocarbon generation temperatures (Ketcham, 2005).

The measurement of fission tracks length, led the reconstruction of the thermal evolution in the PAZ interval (Zattin et al, 2005).

To determine the crystal age, the adopted technique is the External Detector Method (EDM) which main stage are reported in Fig. 3.11.

Samples were crushed with a jaw mill and heavy minerals were separated with a shaking table. Apatite grains (which have a density of 3,16 g/cm³) have been separated using Na-politungstate heavy liquid with a slightly lower density (3,00 g/cm³) and magnetic techniques. Magnetic minerals are separated from the diamagnetic ones (apatite and zircon) through a magnetic separator (Frantz) and then apatites are isolated using Methylene Iodide liquid.

Mounts were ground and polished to expose planar surfaces and then etched with 5N HNO₃ at 20°C for 20s to reveal spontaneous fission tracks.

In order to determine the ²³⁸U concentration, polished mounts are covered with free-U muscovite and were then irradiated with thermal neutrons in the reactor at the Radiation Center of Oregon State University with a nominal neutron fluence of $9 \times 10^{15} \text{ n cm}^{-2}$.

The standard glass CN-5 was used as a dosimeter to measure the neutron fluence. Neutrons hit uranium still present in the apatite grain and caused an artificial fission. After irradiation, induced fission tracks of ^{235}U in the muscovite and glass dosimeter were revealed by etching in 40% HF at 20°C for 40 minutes.

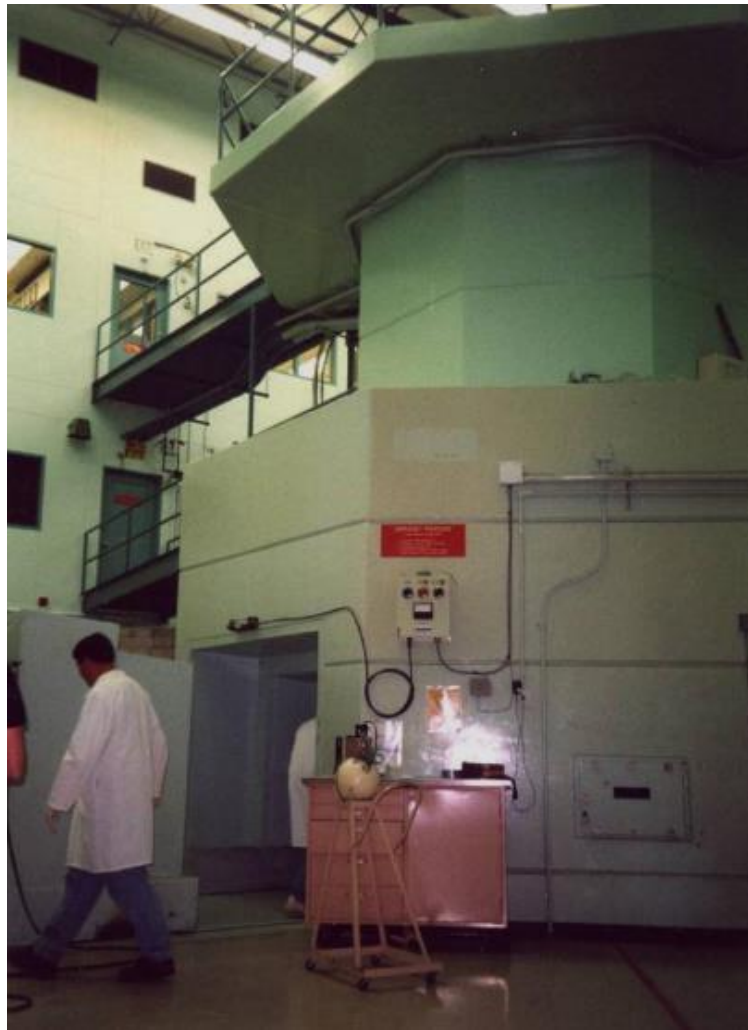


Fig. 3.10. Reactor of the Oregon State University

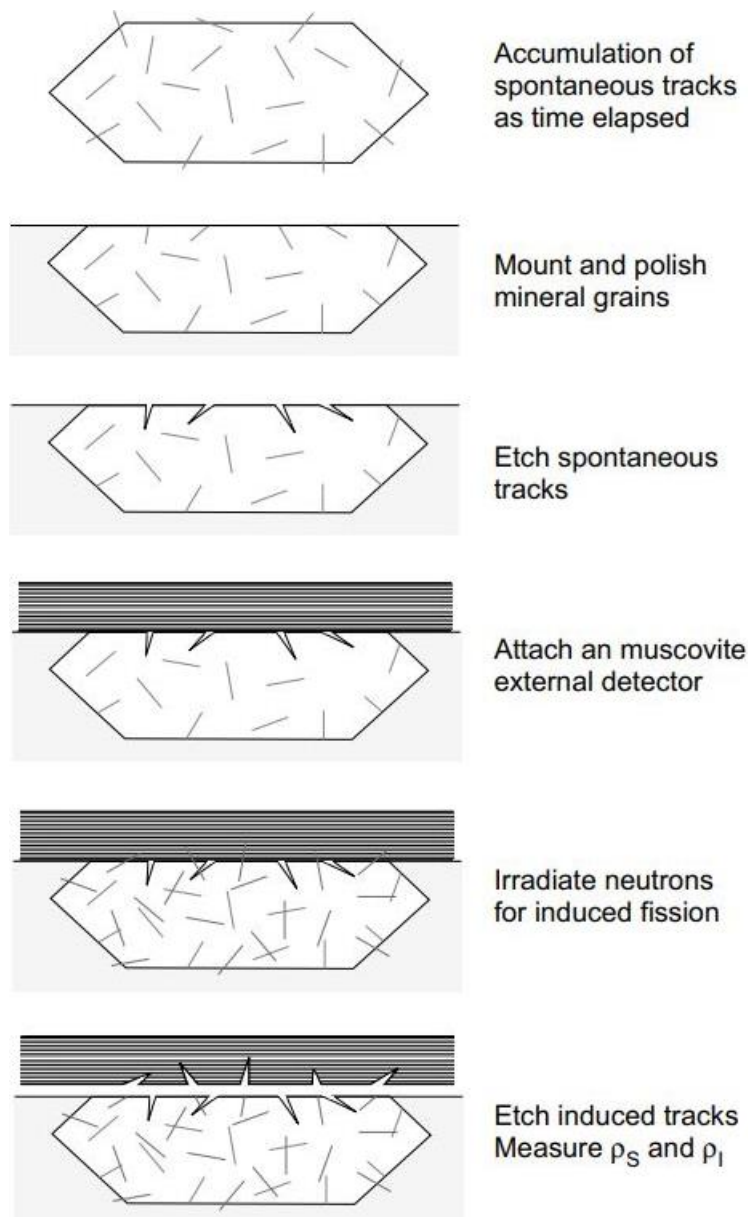


Fig. 3.11. Schematic illustration of fission track analysis with EDM method. ρ_s is the spontaneous fission track density on the apatite mount, ρ_l is the induced fission track density on the muscovite sheet (Tagami and O'Sullivan, 2005).

Fission track density are measured on the apatite and on the muscovite sheet and the ratio between daughter and parent isotope gives the age.



Fig. 3.12. Computer-controlled microscope at Unipd Laboratory.

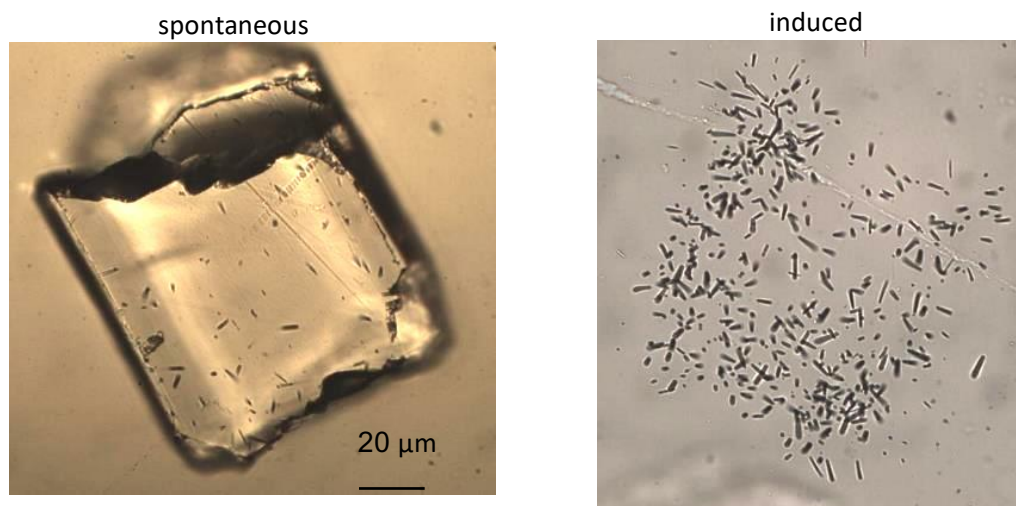


Fig. 3.13 Example of spontaneous and induced fission track on apatite and mica crystals.

AFT dates were calculated using the external-detector and the zeta-calibration method (Hurford and Green, 1983) with IUGS age standards (Durango, Mount Dromedary and Fish Canyon apatites (Hurford, 1990) and a value of 0.5 for the $4\pi/2\pi$ geometry correction factor. The analyses were subjected to the χ^2 test to detect whether the data sets contained any extra-Poissonian error (Galbraith, 1981).

- *U-Th/He method* was performed to quantify the cooling history of the rocks. U-Th/He dating method is based on the α -decay of uranium and thorium elements, which produce ^4He particles (Ehlers and Farley, 2003). This ^4He can be retained within the mineral or can be lost by diffusion to the grain margin as a function of temperature.

^4He nuclei (α particles) are produced by decay of ^{238}U , ^{235}U and ^{232}Th and by α -decay of ^{147}Sm . Therefore, the ingrowth equation is:

$$^4\text{He} = 8^{238}\text{U}(e^{\lambda_{238}t} - 1) + 7\left(\frac{^{238}\text{U}}{137.88}\right)(e^{\lambda_{235}t} - 1) + 6^{232}\text{Th}(e^{\lambda_{232}t} - 1)$$

where ^4He , U and Th refer to present-day amounts, t is the accumulation time or He age, and λ is the decay constant ($\lambda_{238} = 1.551 \times 10^{-10} \text{ yr}^{-1}$, $\lambda_{235} = 9.849 \times 10^{-10} \text{ yr}^{-1}$, $\lambda_{232} = 4.948 \times 10^{-11} \text{ yr}^{-1}$). The factor (1/137.88) is the present-day $^{235}\text{U}/^{238}\text{U}$ ratio and the coefficient preceding the U and Th abundances account for the multiple α particles emitted within each of the decay series (Farley, 2002).

The analysis has been done on samples selected through a stereoscope examination under transmitted and reflected light. 14 grain with a minimum section of 60 μm , euhedral shape, no fracture parallel to the c axis, inclusion and coating free, were selected. After the selection, samples suitable for the analysis have been analyzed at the Institute of Rock Structure and Mechanics of the Czech Academy of Science through the Alphachron (ASI Instruments). Initially, samples have been heated under vacuum through a Nd-YAG laser for total He degassing and to check small helium inclusions. After that, the concentration of ^4He is determined by ^3He isotope dilution and the measurement of the $^4\text{He}/^3\text{He}$ ratio through an Alphachron

quadrupole mass spectrometer. U, Th and Sm concentrations are finally obtained by isotope dilution using an inductively coupled plasma mass spectrometer.

3.3. Thermal modelling

The thermal model of thermochronological data was developed using the HeFTy 1.9.3. program developed by Richard A. Ketcham (2005), created to obtain thermal history information from thermochronometric and related data through forward or inverse modelling. The theory behind the program is presented by Ketcham, 2016. For this thesis work, forward modelling was used in order to predict the expected data distribution for any given thermal history.

The forward model is a process of predicting what thermochronometers measurement should expect for a sample with a given thermal history and it is helpful for solving a particular geological problem.

For this purpose, a time-temperature graph of a single sample or locality can be used for creating a forward model, which can have associated with multiple thermochronometers (Ehlers et al., 2005).

The figure 3.14. shows an example from HeFTy representing a single sample or locality.

Apatite fission track annealing calibrations used to calculate fission track length reduction as a function of time and temperature derive from Laslett et al., 1987 and Ketcham et al., 2007a while C-axis projection model is from Ketcham et al., 2007b. Calculated track length distribution based on the time-temperature path, is shown as a green line in the output panel (Fig 3.14.).

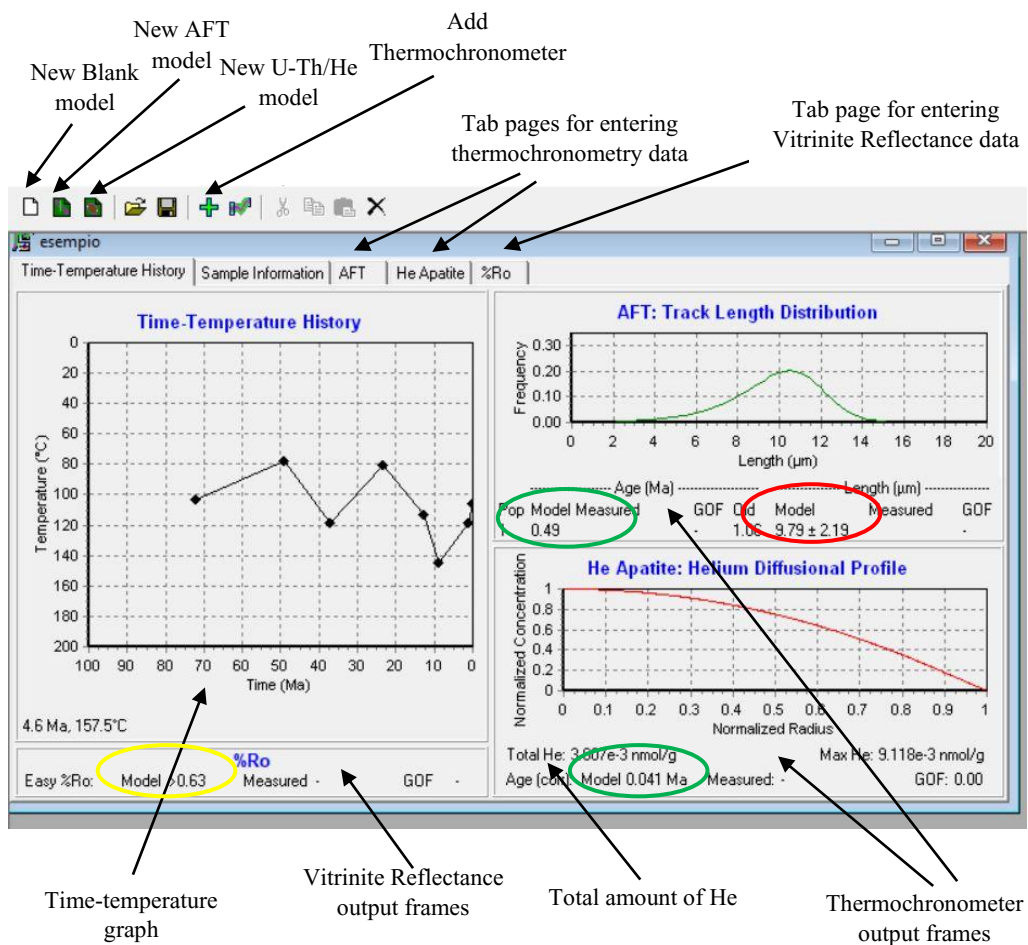


Fig. 3.14. The HeFTy user interface. The values of modelled ages are highlighted in green and the model AFT length is in red. Model %Ro is in yellow.

Below the graph are present values describing the model age (Ma) predicted by HeFTy and the model length (μm) representing the mean and standard deviation of the track length distribution predicted by HeFTy.

U-Th/He calculation is made thanks to Farley, 2000 and Flowers et al., 2009. Graphs show the radial profile of relative He concentration: from left to right corresponds to the progression from core to rim.

Below the graph are shown the model age (Ma) and are reported either the total amount of Helium in the grain (nmol/g) or the effective fission track density (tracks/cm²) if the Flower et al., 2009 model is used.

Vitrinite Reflectance is modelled using the Easy Ro% method of Sweeney and Burnham, 1990. HeFTy begins the calculation from of the deposition age of the sample, defined as the time of minimum temperature that is not present-day. This temperature must be below 25°C. If no deposition event is implied by the time-temperature path, then the entire path is used to calculate %Ro.

Chapter 4

Results

4.1. Maturity profiles of organic matter

Vitrinite Reflectance analyses have been carried out by Eni Laboratories. The maturity trend suggests a paleo-thermal gradient ranging around 50°C/km while the present thermal gradient is ranging around 40°C/km.

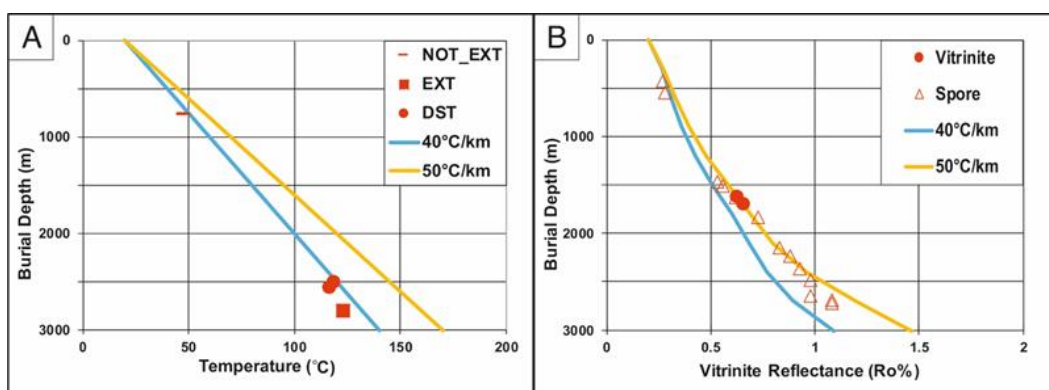


Fig. 4.1. A) Well NC temperature (NOT_EXT=Non extrapolated Log Temperature, EXT=Extrapolated Log Temperature, DST=Production Test Temperature). B) Experimental maturity profile. Vitrinite = Maturity from Vitrinite, Spore = Maturity Ro%eq from spores

The vitrinite profile shows a linear increase with depth although the presence of the Hercynian unconformity with Triassic sediments lying directly on the Paleozoic sequence. This surface is present at a depth of about 1000 m in the well A but the vitrinite reflectance profile does not show the typical gap in the maturity profile between samples below and above the unconformity.

In fact, Ro profiles with a jump in the values usually indicates an unconformity with a large stratigraphic gap, but here the continuity in the organic matter profile suggests that the Hercynian erosion is negligible, or that it was overwritten by the Mesozoic burial and thermal history.

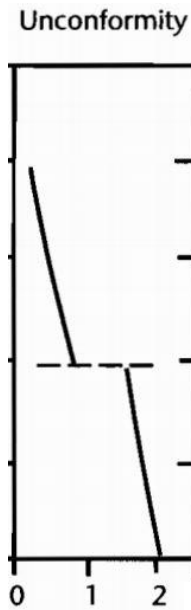


Fig. 4.2. Example of a jump in Ro values, due to an unconformity (Allen and Allen, 2013)

Simulations show that a heating event is needed to match the maturity gradient with the measured values. Moreover, the continuity in the organic matter maturity profile suggest also that the paleo-thermal event affected the entire sedimentary sequence. Since the uppermost samples derives from the *Continental Intercalaire Fm.* of the Late Cretaceous period (located at a depth of around 500 m), the thermal event that characterized the basin must be younger than Late Cretaceous.

In relation of this experimental evidences, three thermal scenarios have been postulated.

The first is a non-realistic scenario where it is assumed a progressive heating with the increase burial depth under constant heat flow.

The other two have been postulated considering a thermal event related to the volcanic activity within the area during the Tertiary time possibly due to the movement of the North African Craton on the hot spot presently active on Canary Islands.

As a matter of fact, in every well simulation, data are not able to discriminate a lower or an upper Tertiary peak event, given that the maturity profile does not show substantial changes.

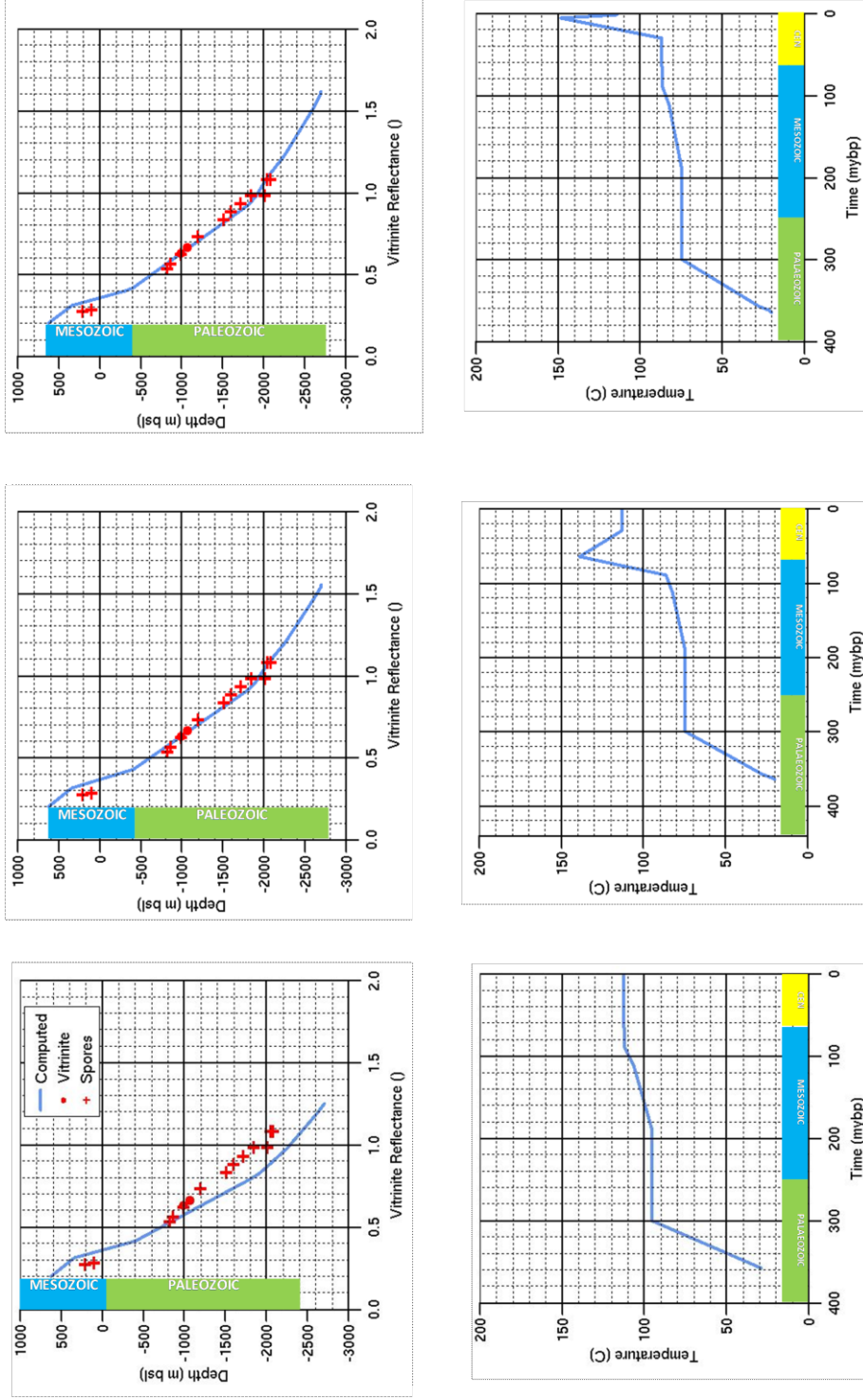


Fig. 4.3. Experimental maturity profile of organic matter in Well NC compared to the maturity profiles predicted by the 3 tested thermal scenarios. A) No Tertiary thermal peak. B) Early Tertiary peak (65 Ma). C) Late Tertiary peak (5.4 Ma). Data were obtained by entering a burial history

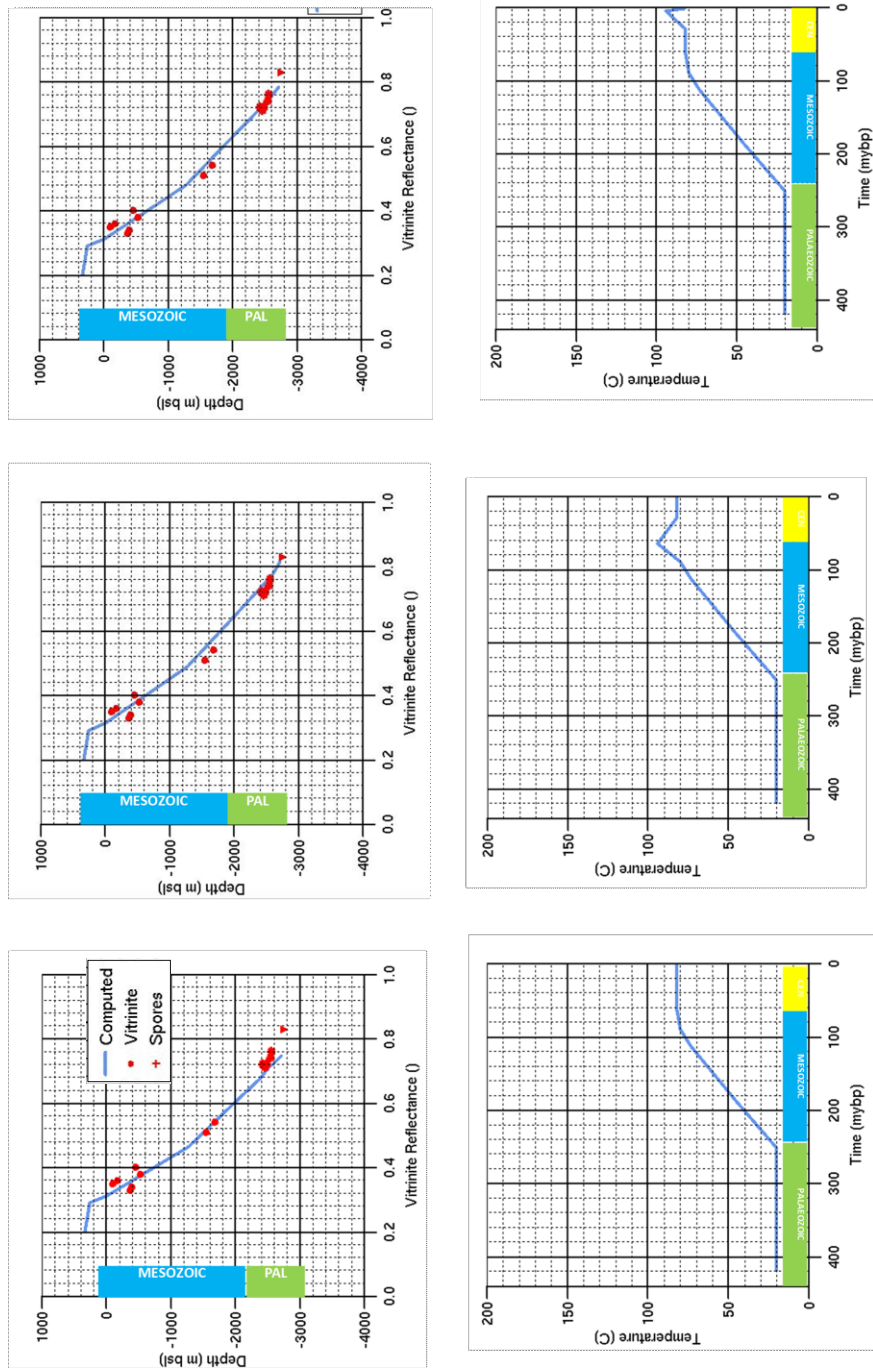


Fig. 4.4. Experimental maturity profile of organic matter in Well A compared to the maturity profiles predicted by the 3 tested thermal scenarios. A) No Tertiary thermal peak. B) Early Tertiary peak (65 Ma). C) Late Tertiary peak (5.4 Ma). Data were obtained by entering a burial history

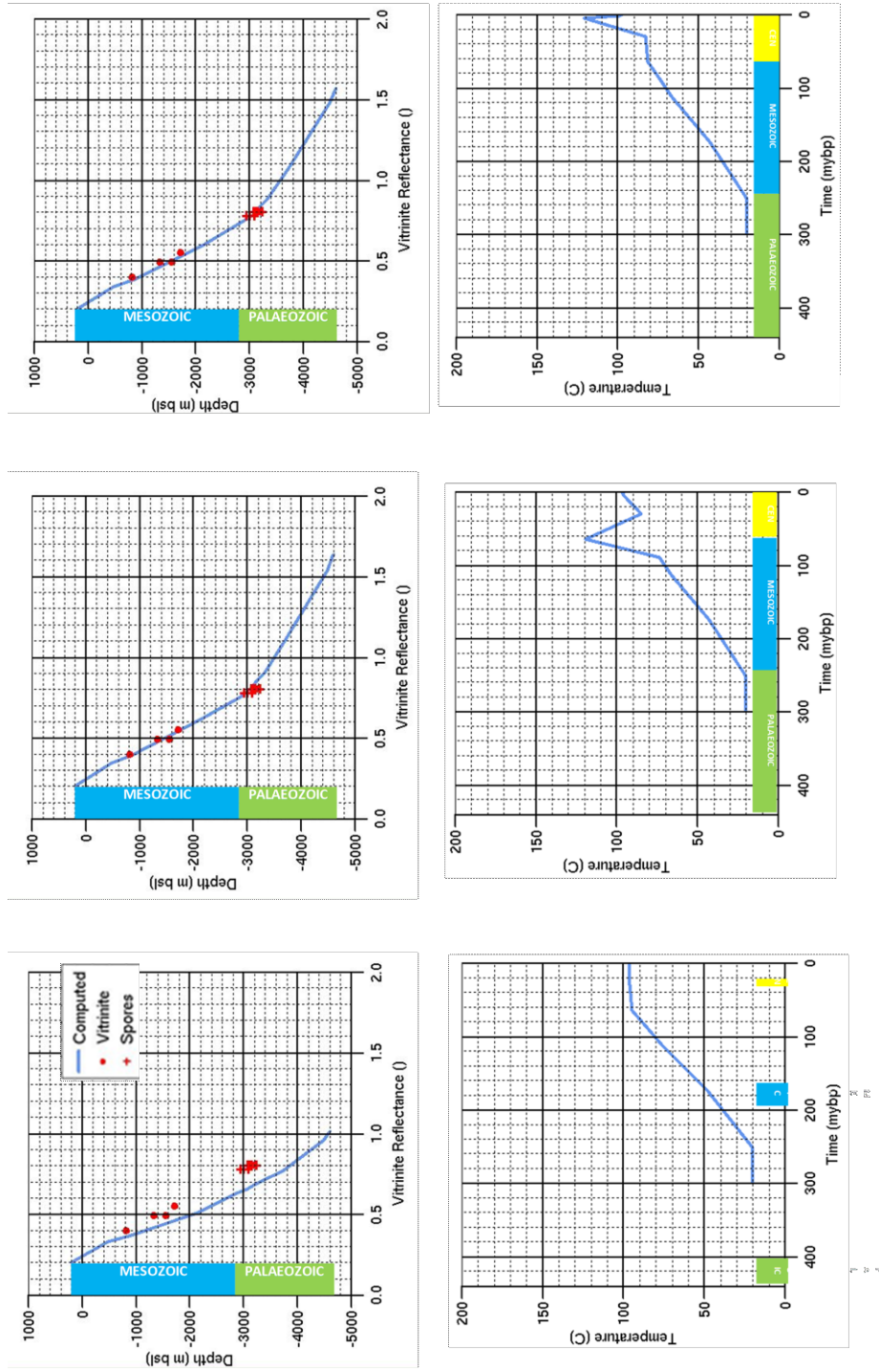


Fig. 4.5. Experimental maturity profile of organic matter in Well BR compared to the maturity profiles predicted by the 3 tested thermal scenarios. A) No Tertiary thermal peak. B) Early Tertiary peak (65 Ma). C) Late Tertiary peak (5.4 Ma). Data were obtained by entering a burial history

Data acquired from inverse modelling show also a change in the trend of the vitrinite maturity which indicates a variation in the heat flow with time.

DIMS_(m)	RO%_BURN()	DIMS_(m)	RO%_BURN()	DIMS_(m)	RO%_BURN()	DIMS_(m)	RO%_BURN()
3329.68	1.61873	3049.9	0.784078	4798.72	1.56584		
3320.78	1.60849	3008.8	0.773455	4777.52	1.54838		
3320.78	1.60849	3008.8	0.773455	4777.52	1.54838		
3238.15	1.51971	2913.83	0.748947	4685.22	1.47984		
3238.15	1.51971	2913.83	0.748947	4685.22	1.47984		
2878.94	1.23013	2856.95	0.741351	3926.07	1.07202		
2878.94	1.23013	2856.95	0.741351	3926.07	1.07202		
2647.79	1.07613	2836.89	0.737123	3515.22	0.87715		
2647.79	1.07613	2836.89	0.737123	3515.22	0.87715		
2622.52	1.05711	2713.72	0.708304	3407.26	0.841251		
2622.52	1.05711	2713.72	0.708304	3407.26	0.841251		
2567.92	1.00927	2273.91	0.617922	3252.19	0.783494		
2567.92	1.00927	2273.91	0.617922	3252.19	0.783494		
2545.62	0.99011	1611.21	0.478157	3132.13	0.754265		
2545.62	0.99011	1611.21	0.478157	3132.13	0.754265		
2443.1	0.924088	341.602	0.313025	3061.34	0.740147		
2443.1	0.924088	341.602	0.313025	3061.34	0.740147		
1037.74	0.417247	71.659	0.289935	2331.96	0.595017		
1037.74	0.417247	71.659	0.289935	2331.96	0.595017		
935.65	0.397646	0	0.201897	1056.56	0.382603		
935.65	0.397646			1056.56	0.382603		
290.092	0.308509			679.569	0.338556		
290.092	0.308509			679.569	0.338556		
0	0.201897			0	0.201897		

Tab. 4.1. Vitrinite Reflectance values obtained from forward modelling. From left to right are well NC, well A and well BR data.

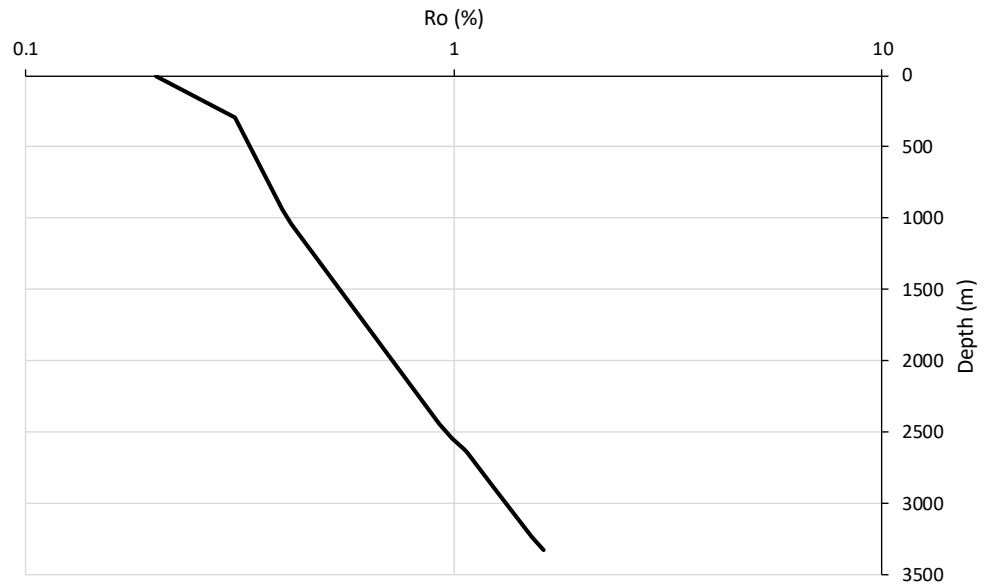


Fig. 4.6. Vitrinite profile of well NC obtained from forward modelling of a thermal history

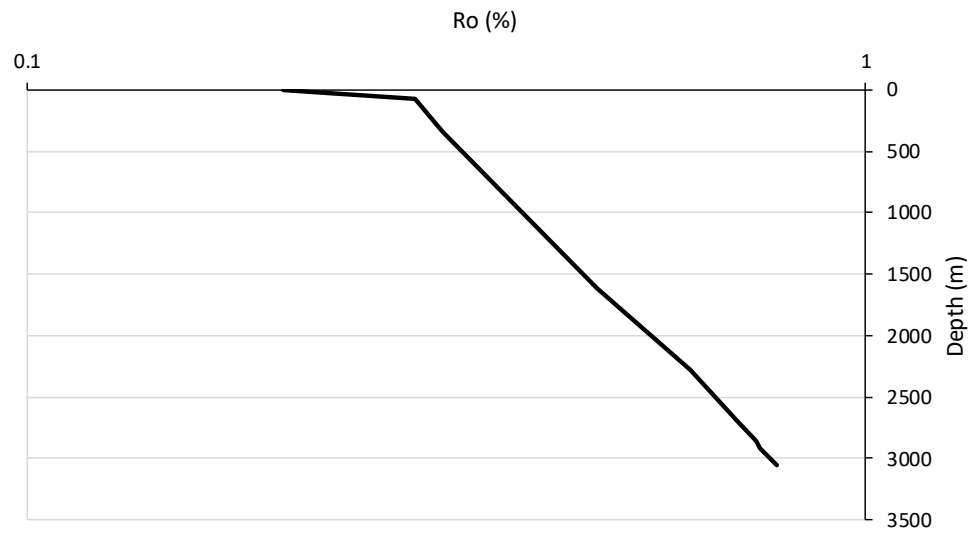


Fig. 4.7. Vitrinite profile of well A obtained from forward modelling of a thermal history

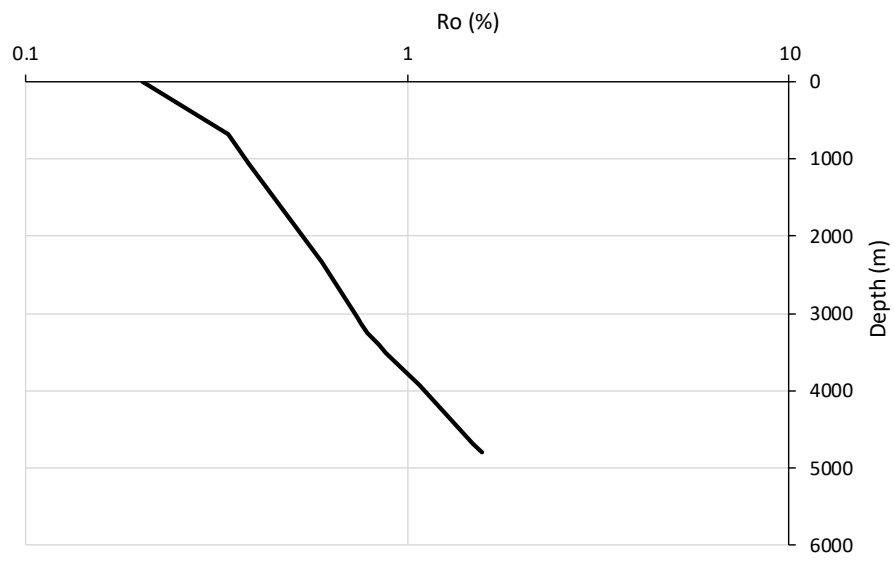


Fig. 4.8. Vitrinite profile of well BR obtained from forward modelling of a thermal history

4.2. Fission track analysis and interpretation

This analysis needs a significant number of apatite grains (usually more than 20), but, given the small amount of available core material, it was possible to date only two samples (Tab 3.1.).

Single grain data age is calculated with dedicated software and AFT data can be then visualized in a radial plot. The y -axis represents the standard error of the single grain age related to the central age of the whole population, while the x -axis represents the relative error increasing toward the y -axis.

Every “+” symbol indicates a single grain and its age is read on the intercept with the radial axis. The accuracy of the data is increasing toward the radial scale.

The AFT age is usually calculated as a weighted mean age derived from the individual single grain ages (“Central age”, Galbraith, 1981). The accuracy of the central age depends on the crystal size and on its uranium content: the larger it is and the higher is its uranium content, the better the age data.

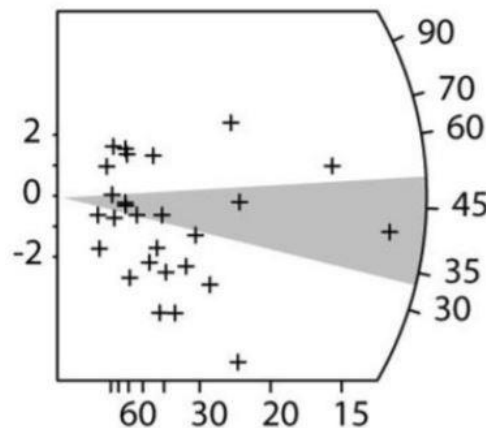


Fig. 4.9. Example of a radial plot.

The χ -square test (Galbraith, 1981) is used to understand if all the grains belong to the single population of age. A probability ($P\chi^2$) of less than 5% indicates a large dispersion in the radial plot which, in sample derived from sedimentary rocks, means the presence of grains derived from different sources. If the probability is 100%, grains belong to the same population.

The χ -square test is also important to determine the burial depth of the sediments as the single grain age dispersion tends to decrease with the increase of burial. If the

probability is close to 5%, (i.e. high dispersion), it means that the burial temperature is on the order of about 70-80°C while if all the crystals belong to the same population, we can infer a burial temperature of more than 120°C (assuming that crystals derived from sources with different thermal histories).

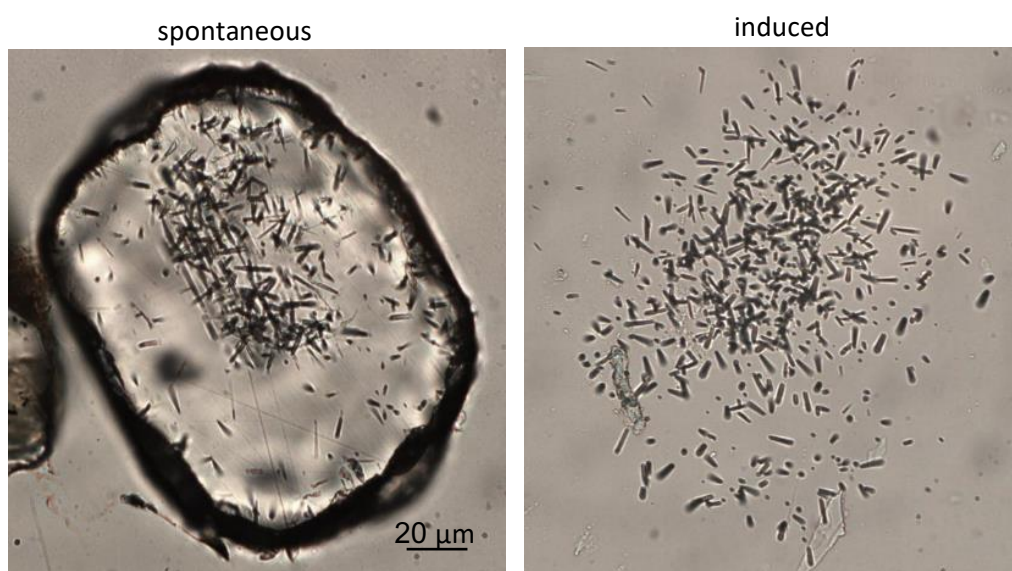


Fig. 4.10. Apatite and mica analyzed for spontaneous and induced fission track density and age

The two samples analysed at the University of Padua, show a very similar central age (of about 145 Ma) but, in both the cases, the χ -square test is failed, thus indicating a significant spread of single grain ages.

Sample number	No of crystals	Spontaneous		Induced		$P(\chi)^2$	Dosimeter		Age (Ma) $\pm 1\sigma$	P1	P2
		ρ_s	N_s	ρ_i	N_i		ρ_d	N_d			
S2	21	6.02	532	0.88	602	0.0	0.99	5154	149.5 \pm 15.8	91.5 \pm 10.7	207.4 \pm 16.6
S3	20	13.01	969	1.55	1301	0.0	0.99	4798	141.4 \pm 16.6	78.8 \pm 5.5	191.9 \pm 11.7

Tab. 4.2. Thermochronologic data from apatite fission track analysis. Central ages calculated using a dosimeter glass CN-5 and ζ -CN5=355.02 \pm 4.36. ρ_s is the spontaneous track density ($\times 10^5 \text{ cm}^{-2}$). N_s is the total number of spontaneous tracks; ρ_i and ρ_d are induced and dosimeter track densities ($\times 10^6 \text{ cm}^{-2}$) on external mica detectors. N_i and N_d are the total number of tracks. $P(\chi^2)$ is the probability of obtaining χ^2 -value for n degrees of freedom (n is the number of crystals-1); a probability >5% indicates a homogeneous population. P1 and P2 are the binomial peak-fit ages in Ma.

The presence of multiple age populations and the broad dispersion are therefore indications for burial temperatures lower than the thermochronology reset temperature (i.e. about 120°C).

4.3. U-Th/He analysis and interpretation

Distribution of U-Th/He ages is complex due to the fact that very few crystals suitable for dating could be found. Obtained data show a large variety of ages, ranging from 0.4 Ma to 1602.3 Ma.

Sample grain no.	Raw age (Ma)	$\pm\sigma$ (Ma)	U (ppm)	Th (ppm)	Sm (ppm)	⁴ He (moles)	eU (ppm)	FT	fully FT corrected age (Ma)	$\pm\sigma$ (Ma)
S2_A p1	2.50	0.04	23.3	88.5	32.8	3.42 E-15	44.1	0.58	4.3	0.1
S2_A p2	3.00	0.23	39.9	34.9	26.1	7.68 E-15	48.1	0.64	4.7	0.4
S2_A p3	4.02	0.17	151.8	98.4	675.9	2.01 E-14	174.9	0.58	7.0	0.3
S2_A p4	2.51	0.08	36.9	55.4	43.7	3.95 E-15	49.9	0.58	4.4	0.1
S3_A p1	92.50	1.17	25.5	74.0	68.2	2.00 E-13	42.8	0.64	144.1	1.8
S3_A p2	20.00	1.13	162.8	41.0	68.3	2.50 E-13	172.4	0.67	29.7	1.7
S3_A p3	1.66	0.02	86.9	147.9	68.8	1.83 E-14	121.7	0.69	2.4	0.0
S3_A p4	1.90	0.03	27.2	76.1	18.4	6.03 E-15	45.1	0.64	3.0	0.1
B3_A p1	0.26	0.00	37.2	33.5	16.1	1.94 E-15	45.1	0.73	0.4	0.0
B3_A p2	0.73	0.02	47.4	50.6	7.2	2.47 E-15	59.3	0.60	1.2	0.0
B3_A p3	3.84	0.12	40.6	20.9	86.4	2.61 E-14	45.5	0.71	5.4	0.2
B3_A p4	3.65	0.17	30.6	20.8	31.0	1.09 E-14	35.5	0.68	5.3	0.3
B5_A p1	220.30	2.31	3.5	53.1	2.9	6.30 E-13	15.9	0.73	301.4	3.2
A2_A p1	1262.64	49.36	1.3	3.0	0.3	6.44 E-13	2.0	0.79	1602.3	62.6

Tab. 4.3. Thermochronologic data from apatite U-Th/He analysis. Raw age is the age of the grain before the correction. U, Th, Sm (ppm) are U, Th, Sm contents. ⁴He is the concentration of He measured by the mass spectrometer. eU is the Effective Uranium quantity; it is used to represent the concentration of U and Th. It is calculated according to the formula $eU=[U]+0.235x[Th]$. FT is the alpha-ejection correction factor. Fully corrected age is the age of the crystal after the alpha-ejection correction.

- **Sample S2:** four crystals could be analysed. Three of them show very similar ages (between 4.3 and 4.7 Ma) while a fourth crystal yielded an age of 7.0 Ma but, because of its high U and Sm content, its data are not fully reliable and thus this crystal will be not considered in the discussion.

- **Sample S3:** four crystals could be analysed. Two of them show coherent ages of 2.4 and 3.0 Ma while the other two yield much older ages of 29.7 and 144.1 Ma. This is probably due to the presence of inclusions or coating. These latter crystals are not taken in account for the discussion.
- **Sample B3:** four crystals could be analysed. They show a broad range of ages, ranging from 0.4 Ma to 5.4 Ma. The parameters do not allow a exclusion of any crystal.
- **Sample B5:** only one crystal could be dated. The obtained age shows a much older age than the other described crystals, due to the low U content. Because of the impossibility to compare this crystal with other grains, it is not possible to consider it in the discussion.
- **Sample A2:** only one crystal could be dated. This crystal shows results very similar to sample B5. This grain is not taken into account also for the high analytical error.

4.4. Constraints from both apatite FT and U-Th/He ages

Only S2 and S3 samples have been dated with both U-Th/He and fission track analysis. Both the samples show two fission track age populations that are younger than the stratigraphic age. However, their presence implies temperature not higher than 120°C. On the other hand, these samples show very young U-Th/He ages, indicating maximum temperature higher than the reset temperature for the U-Th/He system.

A better definition of the thermal history has been carried out using the HeFTy software.

The present-day temperature in well A is not available, thus it has been hypothesized on the basis of a geothermal gradient of 30°/Km and a surface temperature of 10°C. The thermal path has been therefore forced to pass at a temperature of 10°C at 240-250 Ma (depositional age) and at a temperature of 70±10°C at 0 Ma. Results obtained from inverse modelling show that the modelled age fits well with the experimental ages and that the present-day temperature

corresponds to the maximum burial temperature experienced by the sediments. These results have been obtained from both S2 and S3 samples.

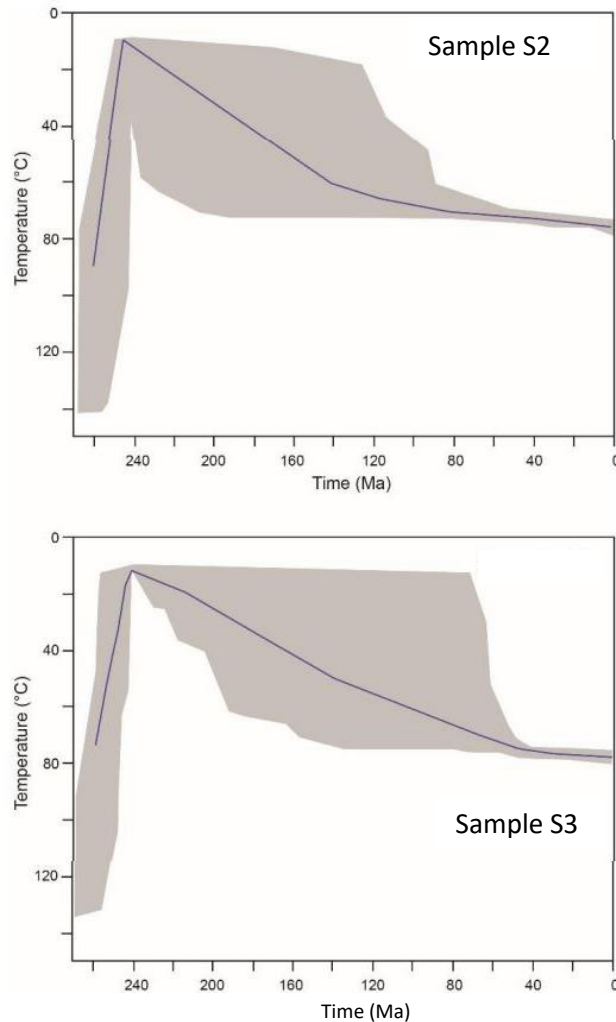


Fig. 4.11. Time-temperature paths obtained from inverse modelling using the HeFTy program (Ketcham, 2005), which generates possible T-t paths using a Monte Carlo algorithm. Shaded areas mark envelopes of statistically good fit (goodness-of-fit [GOF] > 0.5) and thick lines correspond to the weighted mean path. The shaded area between 200 and 60 Ma indicates that these data do not constrain in detail the post-depositional history (i.e. the burial) but the present-day temperature corresponds to the maximum temperature that affected these sediments.

However, results obtained by inverse modelling show a quite large spread of possible thermal path. In order to better constrain the thermal history, some forward

modelling has been performed to test different burial temperatures and thermal paths (Fig. 4.12.).

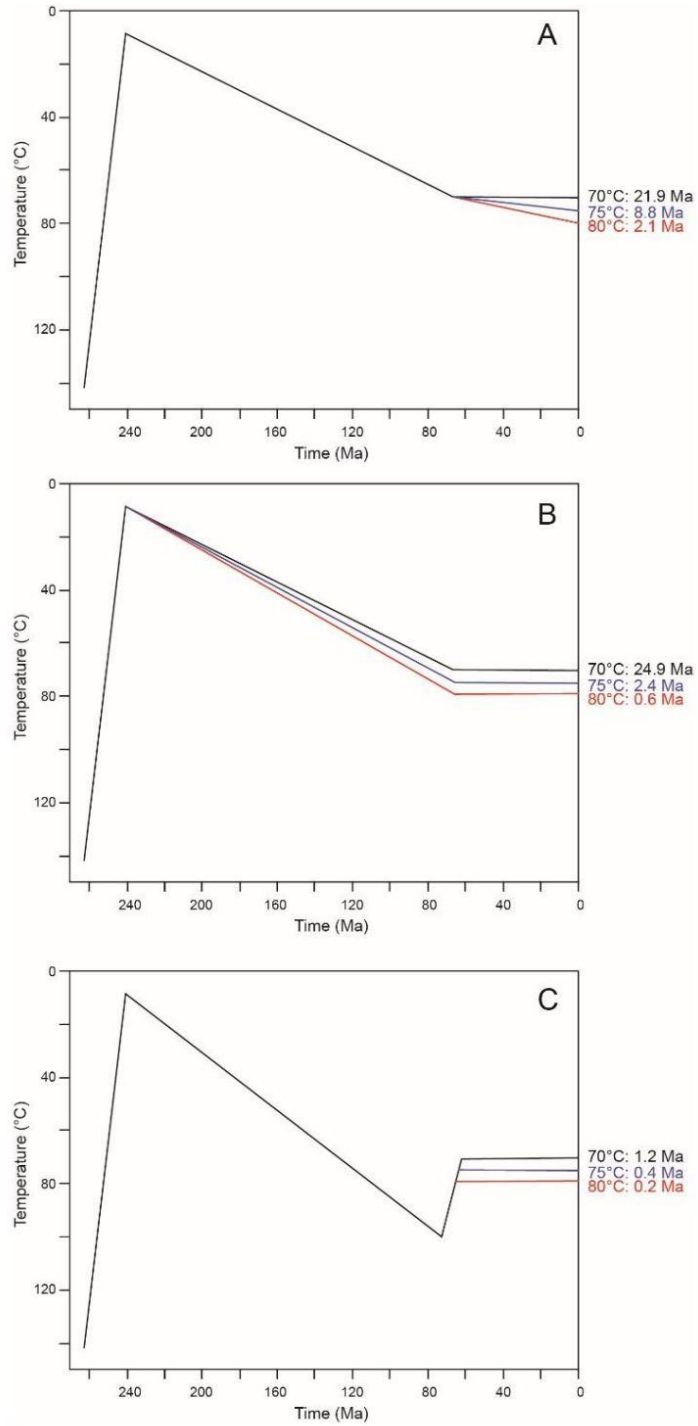


Fig. 4.12. Results obtained from forward modelling of U-Th/He data for a crystal of sample S3 dated at 2.38 Ma

The models of figure 4.12.A are based on a progressive and uninterrupted burial, with a change of burial rates at the end of Cretaceous. The obtained age is compatible with a maximum temperature of about 80°C reached at t=0 Ma.

Figure 4.12.B shows three different thermal histories with three distinct temperature peaks reached at the end of Cretaceous. In this case a temperature of 80°C seems to be too high whereas a better fit is obtained with a temperature of 75°C.

Models shown in figure 4.12.C have a thermal peak of 100°C at 65Ma and a progressive cooling until 70-80°C. In this case, no thermal path fit well with the experimental data.

Interpretation of data from well BR is much more complex. The deepest sample (B5) shows an age much older than the shallower samples. However, the reliability of data from B5 is very low due to the low U content and the Paleozoic age of the apatites. In fact, data from very old samples are often affected by many issues that make the reliability of the results quite low.

Age data from B3 are quite young and this dataset is compatible with an advanced degree of reset, in which very small variations in the apatite kinetics give rise to very different ages.

Very complex is also the interpretation of A2 data because there are not very reliable apatites due to their low U and Th content. This age is thus not considered.

4.5. Thermal modelling results

Forward modelling technique has been applied on data obtained from an inverse modelling made by Eni laboratories.

For each well, a thermal history was made for those samples that had been analyzed with thermochronology methods.

Two simulations with two different hypotheses were developed from which the thermal histories were derived: one with an Upper Tertiary peak and one with a Lower Tertiary one.

1803		
Time(mybp)	DEPTH_(M)	TEMP_(C)
238.960784	0	20
187	-663	41
112	-1884	70
90	-2089	77
65	-2141	78
30	-2141	78
5.4	-2141	90
1.6	-2141	79
0	-1803	79

1855.5		
Time(mybp)	DEPTH_(M)	TEMP_(C)
244.107843	0	18
187	-729	43
112	-1938	72
90	-2142	78
65	-2193	80
30	-2193	80
5.4	-2193	92
1.6	-2193	81
0	-1855	80

1866.7		
Time(mybp)	DEPTH_(M)	TEMP_(C)
245.205882	0	20
187	-743	43
112	-1950	72
90	-2153	78
65	-2205	80
30	-2205	80
5.4	-2205	92
1.6	-2205	81
0	-1867	80

2627.5		
Time(mybp)	DEPTH_(M)	TEMP_(C)
451.736842	0	20
444	-79	23
443	-135	24
440	-178	27
433	-374	35
419	-904	51
382	-904	52
372	-904	52
362	-904	52
358	-904	52
300	-904	52
252	-904	52
187	-1626	71
112	-2727	94
90	-2918	100
65	-2966	102
30	-2966	102
5.4	-2966	118
1.6	-2966	103
0	-2628	102

2628.3		
Time(mybp)	DEPTH_(M)	TEMP_(C)
451.854737	0	20
444	-80	23
443	-136	24
440	-180	27
433	-375	35
419	-905	51
382	-905	52
372	-905	52
362	-905	52
358	-905	52
300	-905	52
252	-905	52
187	-1626	71
112	-2727	94
90	-2919	100
65	-2967	102
30	-2967	102
5.4	-2967	118
1.6	-2967	103
0	-2629	102

Tab. 4.4. Thermal history calculated for samples 1803, 1855.5, 1866.7, 2627.5, 2628.3 of well A with an Upper Tertiary thermal peak.

1803		
Time(mybp)	DEPTH_(M)	TEMP_(C)
238.960784	0	20
187	-663	41
112	-1884	70
90	-2089	77
65	-2141	90
30	-2141	79
5.4	-2141	78
1.6	-2141	78
0	-1803	78

1855.5		
Time(mybp)	DEPTH_(M)	TEMP_(C)
244.107843	0	20
187	-729	43
112	-1938	72
90	-2142	78
65	-2193	92
30	-2193	80
5.4	-2193	80
1.6	-2193	80
0	-1855	80

1866.7		
Time(mybp)	DEPTH_(M)	TEMP_(C)
245.205882	0	20
187	-743	43
112	-1950	72
90	-2153	78
65	-2205	92
30	-2205	81
5.4	-2205	80
1.6	-2205	80
0	-1867	80

2627.5		
Time(mybp)	DEPTH_(M)	TEMP_(C)
451.736842	0	20
444	-79	23
443	-135	24
440	-178	27
433	-374	35
419	-904	51
382	-904	52
372	-904	52
362	-904	52
358	-904	52
300	-904	52
252	-904	52
187	-1626	71
112	-2727	94
90	-2918	100
65	-2966	118
30	-2966	103
5.4	-2966	102
1.6	-2966	102
0	-2628	102

2628.3		
Time(mybp)	DEPTH_(M)	TEMP_(C)
451.854737	0	20
444	-80	23
443	-136	24
440	-180	27
433	-375	35
419	-905	51
382	-905	52
372	-905	52
362	-905	52
358	-905	52
300	-905	52
252	-905	52
187	-1626	71
112	-2727	94
90	-2919	100
65	-2967	118
30	-2967	103
5.4	-2967	102
1.6	-2967	102
0	-2629	102

Tab. 4.5. Thermal history calculated for samples 1803, 1855.5, 1866.7, 2627.5, 2628.3 of well A with a Lower Tertiary thermal peak.

2793.8		
Time(mybp)	DEPTH_(M)	TEMP_(C)
295.706996	0	18
252	0	18
174	-872	41
112	-2176	65
90	-2495	72
65	-2996	81
30	-2996	82
5.4	-2996	119
1.6	-2996	98
0	-2795	96

2796		
Time(mybp)	DEPTH_(M)	TEMP_(C)
295.851852	0	18
252	0	18
174	-875	41
112	-2179	65
90	-2497	72
65	-2998	81
30	-2998	82
5.4	-2998	119
1.6	-2998	98
0	-2797	96

2800		
Time(mybp)	DEPTH_(M)	TEMP_(C)
275.720165	0	18
252	0	18
174	-880	41
112	-2183	65
90	-2501	72
65	-3002	81
30	-3002	82
5.4	-3002	119
1.6	-3002	98
0	-2801	96

2801.7		
Time(mybp)	DEPTH_(M)	TEMP_(C)
276.419753	0	20
252	0	20
174	-882	41
112	-2185	65
90	-2503	73
65	-3004	81
30	-3004	82
5.4	-3004	119
1.6	-3004	99
0	-2803	96

3616.1		
Time(mybp)	DEPTH_(M)	TEMP_(C)
409.525854	0	20
383	-464	34
380	-618	39
374	-818	45
372	-966	49
300	-1051	51
252	-1051	51
174	-1830	65
112	-3035	84
90	-3337	91
65	-3818	98
30	-3818	99
5.4	-3818	147
1.6	-3818	119
0	-3617	117

3627.3		
Time(mybp)	DEPTH_(M)	TEMP_(C)
410.509268	0	20
383	-481	35
380	-633	39
374	-833	45
372	-981	49
300	-1065	51
252	-1065	51
174	-1843	65
112	-3047	85
90	-3349	91
65	-3829	98
30	-3829	99
5.4	-3829	147
1.6	-3829	120
0	-3628	117

3656.1		
Time(mybp)	DEPTH_(M)	TEMP_(C)
413.038049	0	20
383	-525	36
380	-673	40
374	-871	46
372	-1017	50
300	-1101	52
252	-1101	52
174	-1876	66
112	-3077	85
90	-3378	92
65	-3858	99
30	-3858	100
5.4	-3858	148
1.6	-3858	120
0	-3657	118

Tab. 4.6. Thermal history calculated for samples 2793.8, 2796, 2800, 2801.7, 3616.1, 3627.3, 3656.1 of well BR with an Upper Tertiary thermal peak.

2793.8		
Time(mybp)	DEPTH_(M)	TEMP_(C)
273.168724	0	20
252	0	20
174	-872	41
112	-2176	65
90	-2495	72
65	-2996	117
30	-2996	84
5.4	-2996	94
1.6	-2996	95
0	-2795	95

2796		
Time(mybp)	DEPTH_(M)	TEMP_(C)
300	0	20
252	0	20
174	-875	41
112	-2179	65
90	-2497	72
65	-2998	117
30	-2998	84
5.4	-2998	94
1.6	-2998	95
0	-2797	95

2800		
Time(mybp)	DEPTH_(M)	TEMP_(C)
275.720165	0	20
252	0	20
174	-880	41
112	-2183	65
90	-2501	72
65	-3002	117
30	-3002	84
5.4	-3002	94
1.6	-3002	95
0	-2801	95

2801.7		
Time(mybp)	DEPTH_(M)	TEMP_(C)
276.419753	0	20
252	0	20
174	-882	41
112	-2185	65
90	-2503	73
65	-3004	117
30	-3004	84
5.4	-3004	94
1.6	-3004	95
0	-2803	95

3616.1		
Time(mybp)	DEPTH_(M)	TEMP_(C)
409.525854	0	15
383	-464	34
380	-618	39
374	-818	45
372	-966	49
300	-1051	51
252	-1051	51
174	-1830	65
112	-3035	84
90	-3337	91
65	-3818	145
30	-3818	101
5.4	-3818	115
1.6	-3818	116
0	-3617	116

3627.3		
Time(mybp)	DEPTH_(M)	TEMP_(C)
410.509268	0	20
383	-481	35
380	-633	39
374	-833	45
372	-981	49
300	-1065	51
252	-1065	51
174	-1843	65
112	-3047	85
90	-3349	91
65	-3829	146
30	-3829	101
5.4	-3829	115
1.6	-3829	116
0	-3628	116

3656.1		
Time(mybp)	DEPTH_(M)	TEMP_(C)
413.038049	0	17
383	-525	36
380	-673	40
374	-871	46
372	-1017	50
300	-1101	52
252	-1101	52
174	-1876	66
112	-3077	85
90	-3378	92
65	-3858	147
30	-3858	102
5.4	-3858	116
1.6	-3858	117
0	-3657	117

Tab. 4.7. Thermal history calculated for samples 2793.8, 2796, 2800, 2801.7, 3616.1, 3627.3, 3656.1 of well BR with a Lower Tertiary thermal peak.

1941		
Time(mybp)	DEPTH_(M)	TEMP_(C)
365.15625	0	20
372	-1	20
364.5	-5	20
362	-53	22
358	-217	28
300	-1772	75
252	-1772	75
187	-1842	75
112	-2359	83
90	-2571	87
65	-2571	87
30	-2571	87
5.4	-2571	149
1.6	-1942	115
0	-1942	114

1941		
Time(mybp)	DEPTH_(M)	TEMP_(C)
365.15625	0	20
372	-1	20
364.5	-5	20
362	-53	22
358	-217	28
300	-1772	75
252	-1772	75
187	-1842	75
112	-2359	83
90	-2571	87
65	-2571	139
30	-2571	113
5.4	-2571	113
1.6	-2571	113
0	-1942	113

1958		
Time(mybp)	DEPTH_(M)	TEMP_(C)
365.15625	0	20
372	-1	20
364.5	-5	20
362	-53	22
358	-217	28
300	-1772	75
252	-1772	75
187	-1842	75
112	-2359	83
90	-2571	87
65	-2571	87
30	-2571	87
5.4	-2571	149
1.6	-1942	115
0	-1942	114

1958		
Time(mybp)	DEPTH_(M)	TEMP_(C)
365.15625	0	20
372	-1	20
364.5	-5	20
362	-53	22
358	-217	28
300	-1772	75
252	-1772	75
187	-1842	75
112	-2359	83
90	-2571	87
65	-2571	139
30	-2571	113
5.4	-2571	113
1.6	-2571	113
0	-1942	113

1913		
Time(mybp)	DEPTH_(M)	TEMP_(C)
363.2	0	20
349.6	-39	22
336.8	-170	26
277.4	-1742	74
224	-1742	74
167.6	-1813	75
102.6	-2331	82
78	-2543	86
53.08	-2543	128
24.32	-2543	107
4.32	-2543	119
1.28	-2417	113
0	-1914	113

1913		
Time(mybp)	DEPTH_(M)	TEMP_(C)
363.2	0	20
349.6	-39	22
336.8	-170	26
277.4	-1742	74
224	-1742	74
167.6	-1813	75
102.6	-2331	82
78	-2543	86
53.08	-2543	138
24.32	-2543	113
4.32	-2543	112
1.28	-2543	112
0	-1914	112

Tab. 4.8. and Tab. 4.9. Thermal history calculated for samples 1941, 1958, 1912 of well NC with an Upper Tertiary thermal peak on the left and with a Lower Tertiary thermal peak on the right.

Based on the thermal models provided by Eni (Tab. 4.4, 4.5, 4.6, 4.7, 4.8, 4.9), thermal histories were produced by forward modelling both for a Lower and an Upper Tertiary thermal peak. Thermal histories are shown in the Appendix from fig. A1 to A31.

AFT ages have been determined with the equations of Laslett et al., 1987 or Ketcham et al., 2007a whereas AHe ages with equations of Farley, 2000 or Flowers et al., 2009. Two different models have been applied as the resulting ages also depend on the equations used.

Results are reported in tab 4.10 and 4.11 where are shown Tmax reached, Ro modelled values, AFT and AHe modelled ages.

Thermal histories have been also produced at the same depths at which samples have been analyzed with thermochronology methods (Tab. 3.1.) and are reported in the Appendix from fig. A31 to A34.

	Tmax	Ro (Ketcham-Farley)	Ro (Laslett-Flowers)	AFT age (Ketcham et al. 2007)	AFT age (Laslett et al. 1987)	He age (Farley 2000)	He age (Flowers et al. 2009)
WellA_UT 1803	90	0.58	0.58	22.1	151	1.1	0.92
WellA_UT 1855.5	92	0.6	0.6	13.9	143	0.937	0.542
WellA_UT 1866.7	92	0.6	0.6	13.9	144	0.937	0.542
WellA_UT 2627.5	118	>0.62	>0.67	1.03	3.02	0.069	0.042
WellA_UT 2628.3	118	>0.62	>0.67	1.03	3.02	0.069	0.042
WellA_LT 1803	90	0.6	0.6	30	146	1.43	0.968
WellA_LT 1855.5	92	0.62	0.62	26.2	142	1.09	0.598
WellA_LT 1866.7	92	0.62	0.62	25.3	141	1.09	0.586
WellA_LT 2627.5	118	>0.62	>0.7	1.38	12.9	0.07	0.042
WellA_LT 2628.3	118	>0.62	>0.7	1.38	12.9	0.07	0.042
WellBR_UT 2793.8	119	>0.62	>0.69	2.05	3.81	0.139	0.078
WellBR_UT 2796	119	>0.62	>0.69	2.05	3.81	0.139	0.078
WellBR_UT 2800	119	>0.62	>0.69	2.03	3.85	0.139	0.078
WellBR_UT 2801.7	119	>0.62	>0.69	1.92	3.78	0.138	0.078
WellBR_UT 3616.1	147	>0.52	>0.68	0	0.61	0.013	0.009
WellBR_UT 3627.3	147	>0.63	>0.68	0.07	0.55	0.013	0.009
WellBR_UT 3656.1	148	>0.0	>0.69	0	0.55	0.011	0.008

Tab. 4.10. Comparison table for well A with an Upper and a Lower Tertiary peak and for well BR with an Upper Tertiary peak. Compared data are Tmax achieved, Ro value (calculated with both Ketcham-Farley and Laslett-Flowers equations, AFT age (calculated from Ketcham and Laslett equations) and AHe (calculated from Farley or Flowers equations)

	Tmax	Ro (Ketcham-Farley)	Ro (Laslett-Flowers)	AFT age (Ketcham et al. 2007)	AFT age (Laslett et al. 1987)	He age (Farley 2000)	He age (Flowers et al. 2009)
WellBR_LT 2793.8	117	>0.63	>0.69	5.1	31.2	0.162	0.089
WellBR_LT 2796	117	>0.63	>0.69	5.1	31.1	0.162	0.089
WellBR_LT 2800	117	>0.63	>0.69	5.1	31.2	0.162	0.089
WellBR_LT 2801.7	117	>0.63	>0.69	5.1	31.2	0.162	0.089
WellBR_LT 3616.1	145	>0.69	>0.69	0	1.11	0.014	0.01
WellBR_LT 3627.3	146	>0	>0.69	0	1.11	0.014	0.01
WellBR_LT 3656.1	147	>0.69	>0.69	0	1	0.013	0.009
WellNC_UT 1913	128	>0.63	>0.7	0.05	1.61	0.02	0.014
WellNC_UT 1941	149	>0.69	>0.69	0	0.99	0.018	0.012
WellNC_UT 1958	149	>0.69	>0.69	0	0.99	0.018	0.012
WellNC_LT 1913	139	>0.63	>0.7	0.1	2.65	0.022	0.015
WellNC_LT 1941	139	>0	>0.69	0	2.02	0.018	0.014
WellNC_LT 1958	138	>0.64	>0.69	0	2.02	0.02	0.014

Tab. 4.11. Comparison table for well BR with an Upper and a Lower Tertiary peak and for well NC with an Upper Tertiary peak. Compared data are Tmax achieved, Ro value (calculated with both Ketcham-Farley and Laslett-Flowers equations, AFT age (calculated from Ketcham and Laslett equations) and AHe (calculated from Farley or Flowers equations)

Well NC has not been modelled as there was only a single grain dated with the U-Th/He method, furthermore not very reliable for its low content in U and Th. Ages derived from the model are always younger than those analyzed both with the hypothesis of maximum temperatures reached at the end of the Cretaceous period, and with the thermal peak in the late Miocene. The reason is due mainly to the present-day temperature, which has been set up to high values.

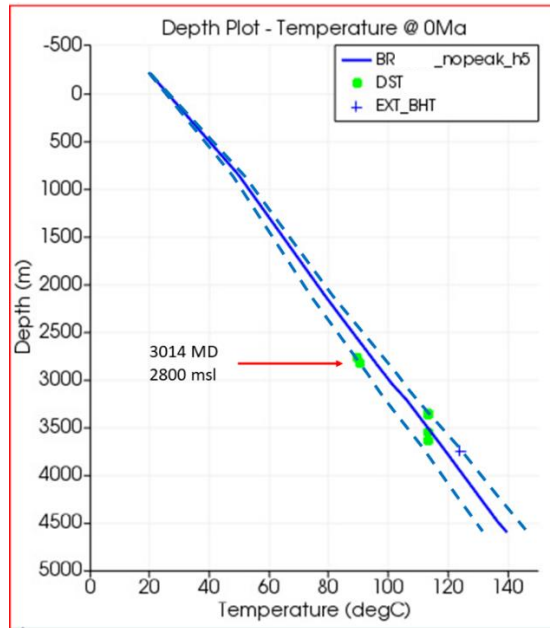


Fig. 4.13. Depth plot of well BR. At depth 3014 (2800 msl), where the calculated temperature is of about 95°C, the range of temperature could vary from 90° to 100°C. EXT=Extrapolated Log Temperature, DST=Production Test Temperature

For this reason, a new set of simulations has been carried out reducing of 5% the present-day temperature values. These thermal histories are shown in the Appendix from fig. A34 to A38.

	Tmax	Ro (Ketcham-Farley)	Ro (T-5%) (Ketcham-Farley)	Ro calculated	Ro (Laslett-Flowers)	Ro (T-5%) (Laslett-Flowers)
WellA 2229.6	80			0.6		
WellA 2240.7	80			0.6		
WellBR 3014	95			0.7		
WellA_LT 2229.6	103	>0.64	>0.64		0.69	0.65
WellA_LT 2240.7	103	>0.64	>0.64		0.69	0.65
WellA_UT 2229.6	105	>0.62	>0.61		0.68	0.64
WellA_UT 2240.7	105	>0.62	>0.61		0.68	0.64
WellBR_LT 3014	126	>0.62	>0.63		>0.69	>0.69
WellBR_UT 3014	128	>0.62	>0.62		>0.69	>0.68

Tab. 4.12. Comparison table for A and BR wells with an Upper and a Lower Tertiary peak. Here are compared Ro calculated data with Ro modelled data with both Ketcham-Farley and Laslett-Flowers equations also obtained with lowering of T by 5%.

	AFT age (Ketcham et al. 2007)	AFT age (T-5%) (Ketcham)	AFT age calculated	AFT age (Laslett et al. 1987)	AFT age (T-5%) (Laslett)
WellA 2229.6			149.5±15.8		
WellA 2240.7			141.4±16.6		
WellBR 3014					
WellA_LT 2229.6	7.25	13.4		69.3	109
WellA_LT 2240.7	7.25	13.4		69.3	109
WellA_UT 2229.6	3.32	4.86		71.2	109
WellA_UT 2240.7	3.32	4.86		71.2	109
WellBR_LT 3014	1.83	3.69		20.1	28.1
WellBR_UT 3014	1.18	1.81		2.62	3.38

Tab. 4.13. Comparison table for A and BR wells with an Upper and a Lower Tertiary peak. Here are compared AFT calculated ages with AFT modelled ages with both Ketcham and Laslett equations also obtained with lowering of T by 5%.

	He age (Farley 2000)	He age (T-5%) (Farley)	He age calculated	He age (Flowers et al. 2009)	He age (T-5%) (Flowers)
WellA 2229.6			4.3-4.7±0.1-0.4		
WellA 2240.7			2.4-3.0±0.0-1.8		
WellBR 3014			0.4-5.4±0.0-0.3		
WellA_LT 2229.6	0.265	0.499		0.138	0.249
WellA_LT 2240.7	0.265	0.499		0.138	0.249
WellA_UT 2229.6	0.258	0.465		0.135	0.234
WellA_UT 2240.7	0.258	0.465		0.135	0.234
WellBR_LT 3014	0.07	0.128		0.042	0.072
WellBR_UT 3014	0.069	0.124		0.041	0.071

Tab. 4.14. Comparison table for A and BR wells with an Upper and a Lower Tertiary peak. Here are compared AHe calculated ages with AHe modelled ages with both Farley and Flowers equations also obtained with lowering of T by 5%.

4.6. Discussion

Results do not show a good fit between thermochronology data and thermal histories deduced by stratigraphy, vitrinite data and present-day temperature, both considering an early and a late Tertiary thermal overprint.

In fact, in both the scenarios, the predicted AFT and U-Th/He ages are younger than measured data.

Considering sample S2 (Tab. 3.1.), the two U-Th/He simulations give very similar ages of about 0.5 Ma (Tab. 4.14.), quite far from the 4.4-4.7 Ma measured on three crystals (Tab. 4.3.) and also AFT data (Tab. 4.13) are lower than those measured (109 Ma compared with 150 Ma; Tab. 4.2.).

Sample S3 (Tab. 3.1.) shows modelled U-Th/He ages of about 0.5 Ma (Tab. 4.14) that do not match with measured 2.4-3.0 Ma (Tab. 4.3.).

Also sample B3 (Tab. 3.1.) shows U-Th/He ages lower than those measured (0.2 Ma compared to 0.4-5.4 Ma; Tab. 4.14 and 4.3.).

The impossibility of a good fit is due to the present-day temperature which is too high to predict ages older than 0.5 Ma. In fact, the last part of thermal history of the well A is in a critic temperature interval, that is inside the retention temperature interval for the U-Th/He system.

This means few degrees of differences can cause ages to vary greatly.

Therefore, we infer that the lack of fit could be related to the lack of direct measurements of borehole temperature. In fact, a decrease of the present-day temperature of the order of 5°C would have strong effects on the predicted ages, which rapidly increase up to the measured values.

It is noteworthy also that the kinetics of He diffusion is still not well known and this could lead some failure of predictions in the thermal modelling.

Chapter 5

Conclusions

This thesis work aimed to give solid constraints to reconstruction of the thermal history of the Ghadames-Illizi Basin through the integration of thermochronology data and their modelling with stratigraphic data and maturity indicators.

A simple model with progressive heating due to increasing of the burial depth does not explain the experimental data. In particular, a significant amount of heating due to burial following the Hercynian erosion can not be hypothesized, due to the maturity profile of the organic matter across the Hercynian surface.

A Tertiary overprint is thus assumed in order to solve the organic matter profile.

From stratigraphic and vitrinite data, a thermal history for samples belonging to A, BR and NC wells has been produced, with two different simulations: one with a thermal event in the lower Tertiary (end of Upper Cretaceous) and one in the upper Tertiary period (end of Miocene).

Thermochronological data have been then modelled by forward modelling techniques in order to validate the thermal history simulations.

Thermochronology data consist of four samples dated with U-Th/He method and two sample dated also with fission-track analysis, both on apatites collected from borehole samples.

Modelled data do not fit well with the measured ones, therefore not allowing to define precisely the time of the possible Tertiary thermal overprint which determination has strong implications on maturation of the source rock. The reason is probably related to a not precise determination of the present-day temperature at sample depth.

Further development of this study may focus on fluid inclusions which could allow a more precise quantification of thermal history.

References

- Allen, P.A.A. and Allen, J.R. (2013) 'Basin Analysis: Principles and Application to Petroleum Play Assessment', Wiley-Blackwell.
- Bodin, S. et al. (2010) 'Timing of early to mid-cretaceous tectonic phases along North Africa: New insights from the Jeffara escarpment (Libya – Tunisia)', *Journal of African Earth Sciences*. Elsevier Ltd, 58(3), pp. 489–506. doi: 10.1016/j.jafrearsci.2010.04.010.
- Boote, D.R.D. et al. (1998) 'Palaeozoic petroleum systems of North Africa', *Geological Society Special Publication*, 132(132), pp. 7–68. doi: 10.1144/GSL.SP.1998.132.01.02.
- Bora, D. and Dubey, S. (2015) 'New insight on petroleum system modeling of Ghadames basin, Libya', *Journal of African Earth Sciences*. Elsevier Ltd, 112, pp. 111–128. doi: 10.1016/j.jafrearsci.2015.08.020.
- Boudjema, A. (1987) 'Evolution structurale du bassin petrolier «Triasique» du Sahara Nord Oriental (Algerie)', *Thèse a l'Universite de ParisSud, Centre d'Orsay*.
- Daniels, R.P. and Emme, J.J. (1995), 'Petroleum system model, eastern Algeria, from source rock to accumulation; when, where, and how?: Proceedings of the Seminar on Source Rocks and Hydrocarbon Habitat in Tunisia'; *Entreprise Tunisienne d'Activités Pétrolières Memoir 9*, p. 101–124
- Dardour, A.M. et al. (2004) 'Stratigraphic controls on palaeozoic petroleum systems, Ghadames Basin, Libya', *Journal of Petroleum Geology*, 27(2), pp. 141–162. doi: 10.1111/j.1747-5457.2004.tb00050.x.
- El Diasty, W.S. et al. (2017) 'Organic Geochemistry of the Lower Silurian Tanezzuft Formation and Biomarker Characteristics of Crude Oils From the Ghadames Basin, Libya', *Journal of Petroleum Geology*, 40(3), pp. 299–318. doi: 10.1111/jpg.12677.
- Dixon, R.J. et al. (2010) 'Integrated petroleum systems and play fairway analysis

in a complex Palaeozoic basin: Ghadames-Illizi Basin, North Africa', *Geological Society London Petroleum Geology Conference series*, 7(0), pp. 735–760. doi: 10.1144/0070735.

Donelick, R.A. et al. (2005) 'Apatite fission-track analysis', *Reviews in Mineralogy and Geochemistry*, 58, pp. 49–94. doi: 10.2138/rmg.2005.58.3.

Echikh, K. (1998) 'Geology and hydrocarbon occurrences in the Ghadames Basin, Algeria, Tunisia, Libya', *Geological Society Special Publication*, 132(132), pp. 109–129. doi: 10.1144/GSL.SP.1998.132.01.06.

Ehlers, T.A. et al. (2005) 'Computational tools for low-temperature thermochronometer interpretation', *Reviews in Mineralogy and Geochemistry*, 58, pp. 589–622. doi: 10.2138/rmg.2005.58.22.

Ehlers, T.A. and Farley, K.A. (2003) 'Apatite (U-Th)/He thermochronometry: Methods and applications to problems in tectonic and surface processes', *Earth and Planetary Science Letters*, 206(1–2), pp. 1–14. doi: 10.1016/S0012-821X(02)01069-5.

English, K.L. et al. (2016) 'Constraining burial history and petroleum charge in exhumed basins: New insights from the Illizi Basin, Algeria', *AAPG Bulletin*, 100(4), pp. 623–655. doi: 10.1306/12171515067.

English, K.L. et al. (2017) 'Intraplate uplift: new constraints on the Hoggar dome from the Illizi basin (Algeria)', *Basin Research*, 29(3), pp. 377–393. doi: 10.1111/bre.12182.

Farley, K.A. (2000) 'Helium diffusion from apatite: General behavior as illustrated by Durango fluorapatite', *Journal of Geophysical Research: Solid Earth*, 105(B2), pp. 2903–2914. doi: 10.1029/1999jb900348.

Farley, K.A. (2002) '(U-Th)/He dating: Techniques, calibrations, and applications', *Reviews in Mineralogy and Geochemistry*, 47. doi: 10.2138/rmg.2002.47.18.

Flowers, R.M. et al. (2009) 'Apatite (U-Th)/He thermochronometry using a

radiation damage accumulation and annealing model', *Geochimica et Cosmochimica Acta*. Elsevier Ltd, 73(8), pp. 2347–2365. doi: 10.1016/j.gca.2009.01.015.

Galbraith, R.F. (1981) 'On statistical models for fission track counts', *Journal of the International Association for Mathematical Geology*, 13(6), pp. 471–478. doi: 10.1007/BF01034498.

Galeazzi, S. et al. (2010) 'Regional geology and petroleum systems of the Illizi-Berkine area of the Algerian Saharan Platform: An overview', *Marine and Petroleum Geology*, 27(1), pp. 143–178. doi: 10.1016/j.marpetgeo.2008.10.002.

Galeazzi, S. et al. (2012) 'The Illizi and Berkine Basins in Southern Algeria' *Regional Geology and Tectonics*. doi: 10.1016/B978-0-444-56357-6.00018-4.

Gallagher, K. (2012) 'Transdimensional inverse thermal history modeling for quantitative thermochronology' *Journal of Geophysical Research*, 117, pp. B02408. doi: 10.1029/2011JB008825

Galushkin, Y. et al. (2014) 'Burial and thermal history modelling of the murzuq and ghadames basins (Libya) using the galo computer programme', *Journal of Petroleum Geology*, 37(1), pp. 71–93. doi: 10.1111/jpg.12570.

Gleadow, A.J.W. et al. (1986) 'Confined fission track lengths in apatite: a diagnostic tool for thermal history analysis' *Contribution of mineralogy and petrology*, 94, pp. 405-415. doi: 10.1007/BF00376334.

Hallett, D. (2002) 'Petroleum Geology of Libya', Elsevier Science

Hrouda, M. (2005) *The hydrocarbon source potential of the Palaeozoic rocks of the Ghadames Basin, NW Libya, Newcastle University*.

Hurford, A.J. (1990) 'Standardization of fission track dating calibration: Recommendation by the Fission Track Working Group of the I.U.G.S. Subcommittee on Geochronology', *Chemical Geology: Isotope Geoscience Section*, 80(2), pp. 171–178. doi: 10.1016/0168-9622(90)90025-8.

Hurford, A.J. and Green, P.F. (1983) 'The zeta age calibration of fission-track dating.', *Isotope Geoscience*, 1(4), pp. 285–317.

Jabir, A. et al. (2020) 'Stratigraphy, sedimentology and paleogeography of a Paleozoic succession, Ghadames and Jefarah basin, Libya and Tunisia', *Journal of African Earth Sciences*. Elsevier, 163(September 2016), p. 103642. doi: 10.1016/j.jafrearsci.2019.103642.

Ketcham, R.A. (2005) 'Forward and inverse modeling of low-temperature thermochronometry data', *Reviews in Mineralogy and Geochemistry*, 58, pp. 275–314. doi: 10.2138/rmg.2005.58.11.

Ketcham, R.A. et al. (2007a) 'Improved measurement of fission-track annealing in apatite using c-axis projection', *American Mineralogist*, 92(5–6), pp. 789–798. doi: 10.2138/am.2007.2280.

Ketcham, R.A. et al. (2007b) 'Improved modeling of fission-track annealing in apatite', *American Mineralogist*, 92(5–6), pp. 799–810. doi: 10.2138/am.2007.2281.

Ketcham, R.A. (2016) 'HeFTy Version 1.9.1'.

Klett, T.R. (2000a) 'Total Petroleum Systems of the Illizi Province , Algeria and Libya-Tanezzuft-Illizi', *USGS Bulletin 2202-A*, p. 79. doi: <https://doi.org/10.3133/b2202A>.

Klett, T.R. (2000b) 'Total petroleum systems of the Trias/Ghadames Province, Algeria, Tunisia, and Libya; the Tanezzuft-Oued Mya, Tanezzuft-Melrhir, and Tanezzuft-Ghadames', *USGS Bulletin 2202-C*, p. 118 p. doi: 10.3133/b2202C.

Laslett, G.M. et al. (1987) 'Thermal annealing of fission tracks in apatite 2. A quantitative analysis', *Chemical Geology: Isotope Geoscience Section*, 65(1), pp. 1–13. doi: 10.1016/0168-9622(87)90057-1.

Macgregor, D.S. (1996) 'The hydrocarbon systems of North Africa', *Marine and Petroleum Geology*, 13(3), pp. 329–340. doi: 10.1016/0264-8172(95)00068-2.

Mann, P. et al. (2005) 'Tectonic setting of the world's giant oil and gas fields', *AAPG Memoir*, (78), pp. 15–105.

Morrow, D.W. and Issler, D.R. (1993) 'Calculation of vitrinite reflectance from thermal histories: A comparison of some methods' *AAPG Bulletin*, 77(4)

Riboulleau, A. et al. (2018) 'Organic matter deposition in the Ghadames Basin (Libya) during the Late Devonian—A multidisciplinary approach', *Palaeogeography, Palaeoclimatology, Palaeoecology*. Elsevier, 497(February), pp. 37–51. doi: 10.1016/j.palaeo.2018.02.004.

Sahagian, D. (1988) 'Epeirogenic motion of Africa as inferred from Cretaceous shoreline deposits', *Tectonic*, 7(1), pp. 125–138.

Scotti, P. (2005) 'Thermal Constraints Suggested By the Study of the Organic Matter and Thermal Modelling Strategies. A Case History From Southern Alps', *Atti Ticinensi di Scienze della Terra*, 10, pp. 21–35.

Shaltami, O.R. et al. (2019) 'Petroleum geochemistry of the Dembaba Formation in well M2-NC115 , Marzuq Basin, SW Libya', *Eastern Mediterranean Gas Conference 2019*, (June).

Sweeney, J.J. and Burnham, A.K. (1990) 'Evaluation of a simple model of vitrinite reflectance based on chemical kinetics', *American Association of Petroleum Geologists Bulletin*, 74(10), pp. 1559–1570. doi: 10.1306/0C9B251F-1710-11D7-8645000102C1865D.

Tagami, T. and O'Sullivan, P.B. (2005) 'Fundamentals of fission-track thermochronology', *Reviews in Mineralogy and Geochemistry*, 58(1992), pp. 19–47. doi: 10.2138/rmg.2005.58.2.

Tlig, S. (2015) 'The Upper Jurassic and Lower Cretaceous series of southern Tunisia and northwestern Libya revisited', *Journal of African Earth Sciences*, 110, pp. 100–115. doi: 10.1016/j.jafrearsci.2015.06.014.

Underdown, R. and Redfern, J. (2007) 'The importance of constraining regional

exhumation in basin modelling: A hydrocarbon maturation history of the Ghadames Basin, North Africa', *Petroleum Geoscience*, 13(3), pp. 253–270. doi: 10.1144/1354-079306-714.

Underdown, R. and Redfern, J. (2008) 'Petroleum generation and migration in the Ghadames Basin, north Africa: A two-dimensional basin-modeling study', *American Association of Petroleum Geologists Bulletin*, 92(1), pp. 53–76. doi: 10.1306/08130706032.

Underdown, R. et al. (2007) 'Constraining the burial history of the Ghadames Basin, North Africa: An integrated analysis using sonic velocities, vitrinite reflectance data and apatite fission track ages', *Basin Research*, 19(4), pp. 557–578. doi: 10.1111/j.1365-2117.2007.00335.x.

Wang, Z. et al. (2019) 'Shale oil and gas exploration potential in the Tanezzuft Formation, Ghadames Basin, North Africa', *Journal of African Earth Sciences*. Elsevier, 153(January), pp. 83–90. doi: 10.1016/j.jafrearsci.2019.02.026.

Van De Weerd, A.A. and Ware, P.L.G. (1994) 'A review of the east Algerian Sahara oil and gas province (Triassic, Ghadames and Illizi Basins)', *First Break*, 12(7), pp. 363–373. doi: 10.3997/1365-2397.1994023.

Wilson, M. and Guiraud, R. (1992) 'Magmatism and rifting in Western and Central Africa, from Late Jurassic to Recent times', *Tectonophysics*, 213(1–2), pp. 203–225. doi: 10.1016/0040-1951(92)90259-9.

Zattin, M. et al. (2005) 'Fission-track evidence for late Oligocene and mid-Miocene activity along the North Anatolian Fault in south-western Thrace', *Terra Nova*, 17(2), pp. 95–101. doi: 10.1111/j.1365-3121.2004.00583.x.

Zattin, M., et al. (2002) 'Fission-track reconstruction of the front of the Northern Apennine thrust wedge and overlying Ligurian unit', *American Journal of Science*, 302(4), pp. 346–379. doi: 10.2475/ajs.302.4.346.

Appendix

The following figures report the thermal histories derived from forward modelling. Starting from the thermal histories, Ro values have been modelled, fission track ages have been determined with both Ketcham et al., 2007a and Laslett et al., 1987 equations and helium ages have been determined with both and Farley, 2000 and and Flowers et al., 2009 equations and are shown in tab. 4.10 and 4.11.

Thermal histories at depth of samples analysed with thermochronological methods are reported (fig. A31-A34) also with a reduction of 5% of the present-day temperature since ages derived from the model are always younger than those analyzed and the present-day temperature has been set up to high values (fig. A34-A38).

Ro values, fission track ages and helium modelled ages are shown in tab. 4.12, 4.13 and 4.14.

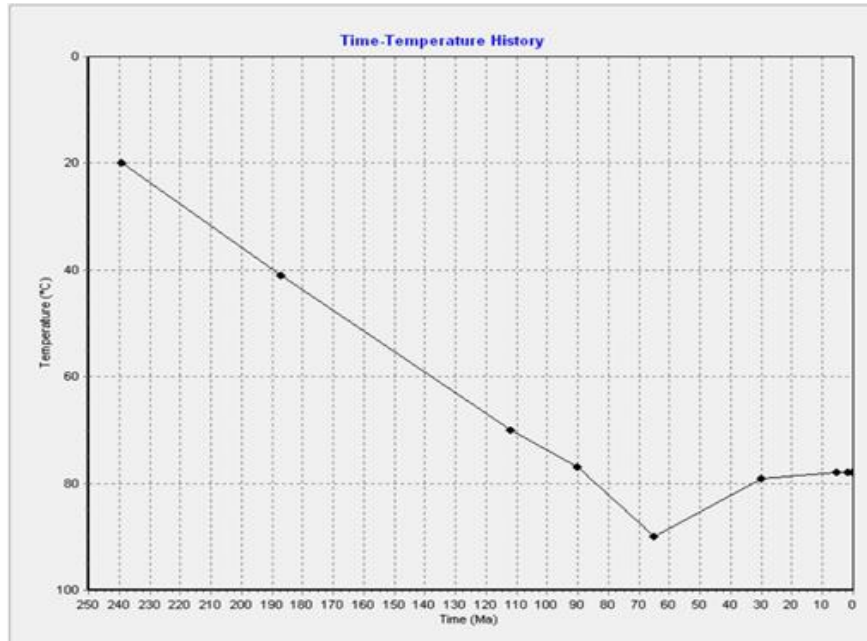


Fig. A1. Thermal history of the well A_LT 1803. Ketcham et al., 2007a and Laslett et al., 1987 equations have been used to determine AFT ages and Farley, 2000 and Flowers et al., 2009 equations have been used to determine AHe ages.

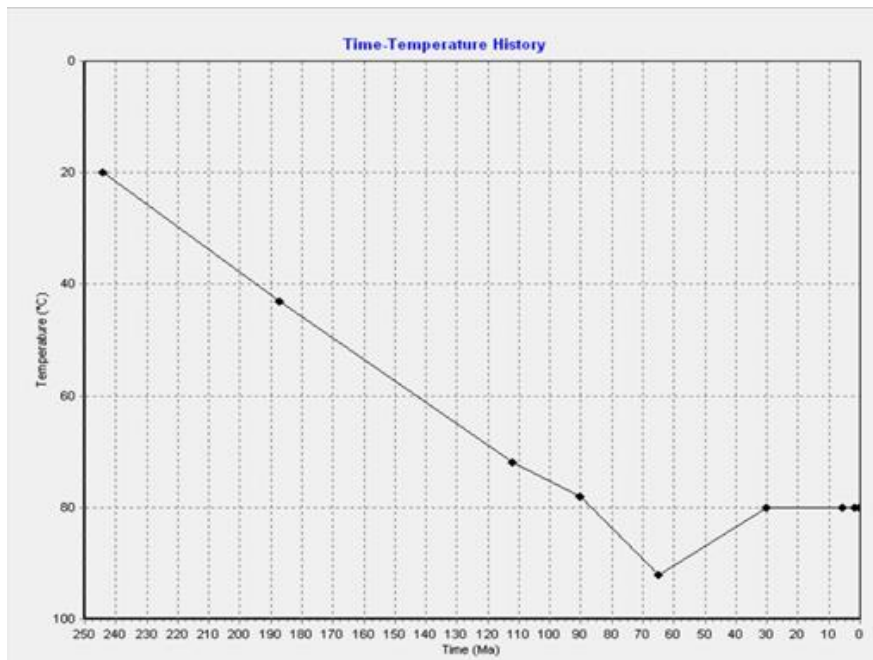


Fig. A2. Thermal history of the well A_LT 1855.5. Ketcham et al., 2007a and Laslett et al., 1987 equations have been used to determine AFT ages and Farley, 2000 and Flowers et al., 2009 equations have been used to determine AHe ages.

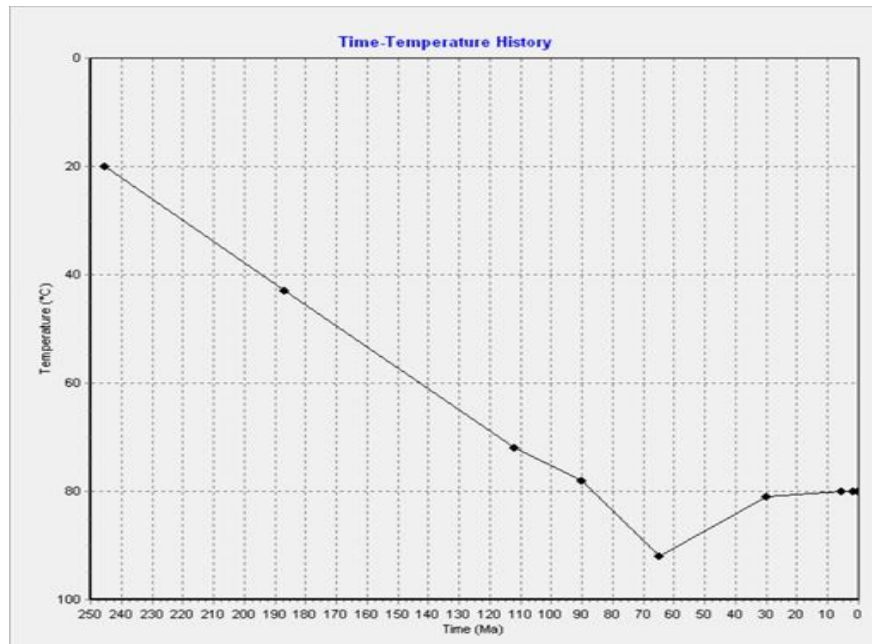


Fig. A3. Thermal history of the well A_LT 1866.7. Ketcham et al., 2007a and Laslett et al., 1987 equations have been used to determine AFT ages and Farley, 2000 and Flowers et al., 2009 equations have been used to determine AHe ages.

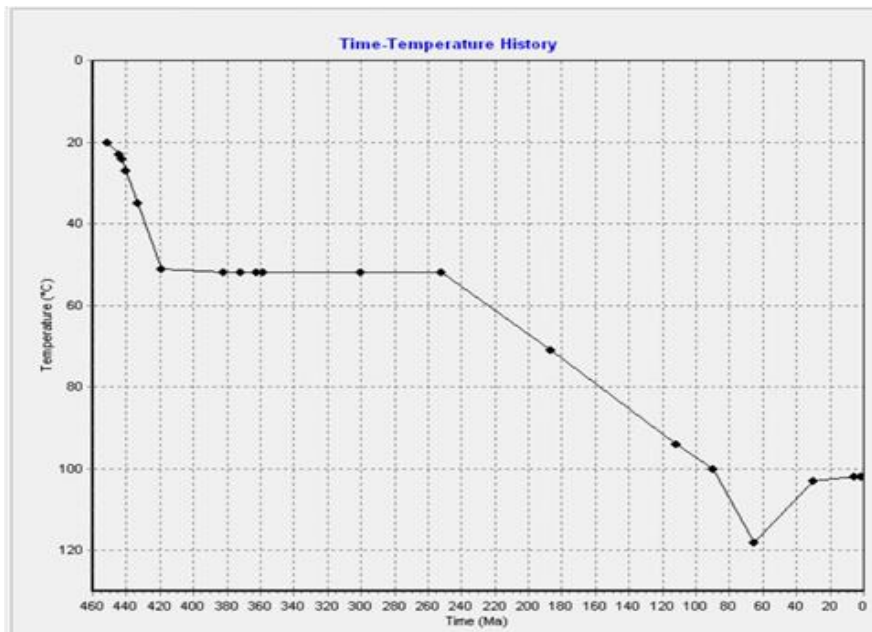


Fig. A4. Thermal history of the well A_LT 2627.5. Ketcham et al., 2007a and Laslett et al., 1987 equations have been used to determine AFT ages and Farley, 2000 and Flowers et al., 2009 equations have been used to determine AHe ages.

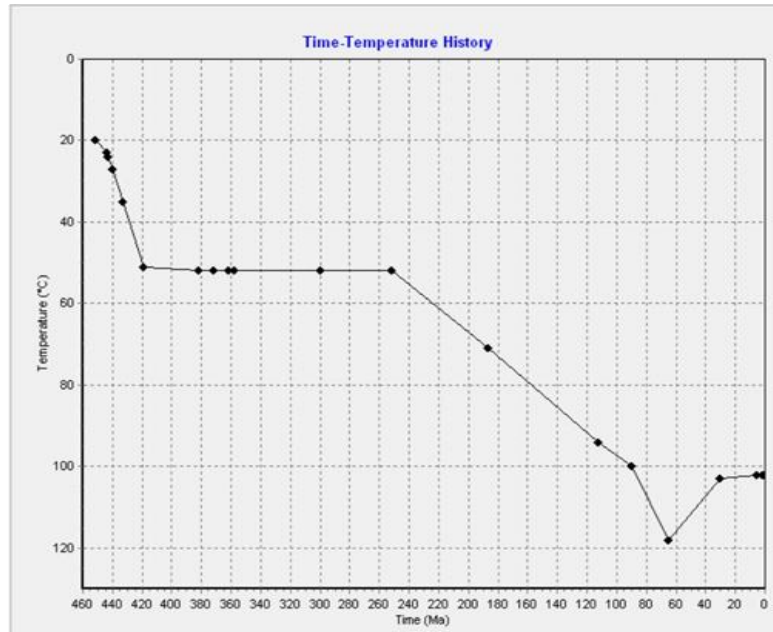


Fig. A5. Thermal history of the well A_LT 2628.3. Ketcham et al., 2007a and Laslett et al., 1987 equations have been used to determine AFT ages and Farley, 2000 and Flowers et al., 2009 equations have been used to determine AHe ages.

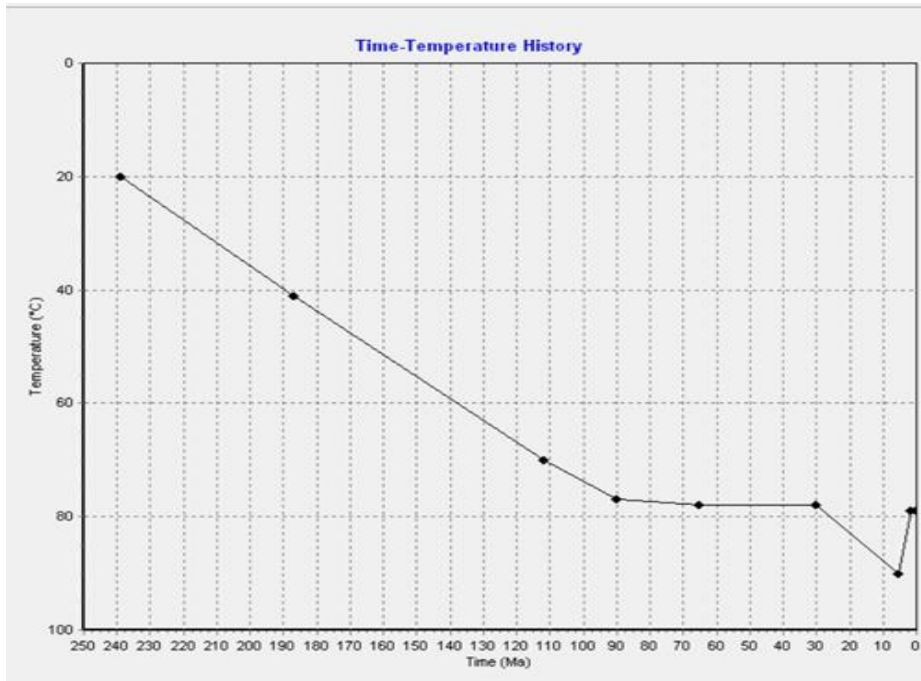


Fig. A6. Thermal history of the well A_UT 1803. Ketcham et al., 2007a and Laslett et al., 1987 equations have been used to determine AFT ages and Farley, 2000 and Flowers et al., 2009 equations have been used to determine AHe ages.

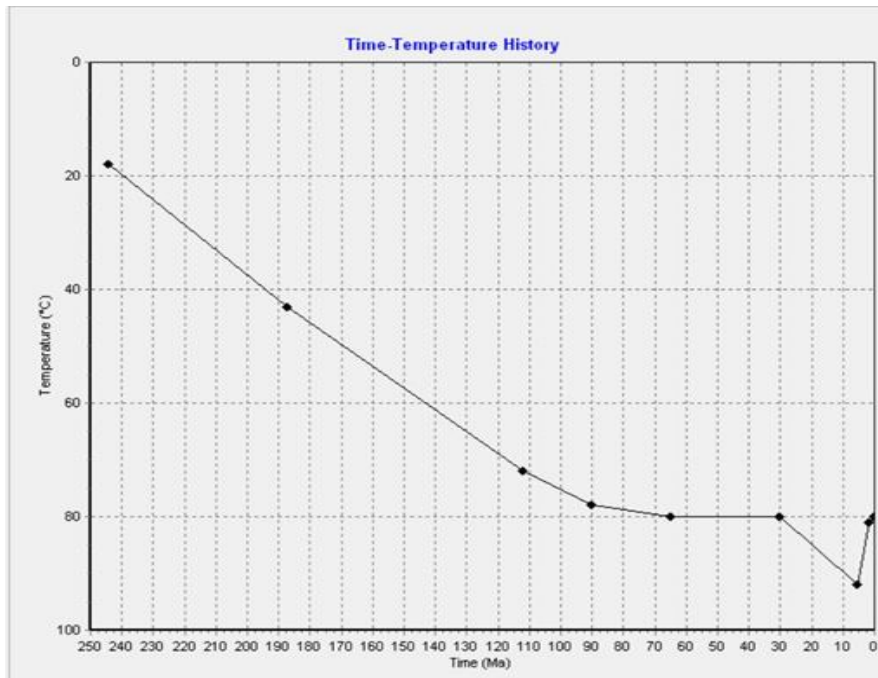


Fig. A7. Thermal history of the well A_UT 1855.5. Ketcham et al., 2007a and Laslett et al., 1987 equations have been used to determine AFT ages and Farley, 2000 and Flowers et al., 2009 equations have been used to determine AHe ages.

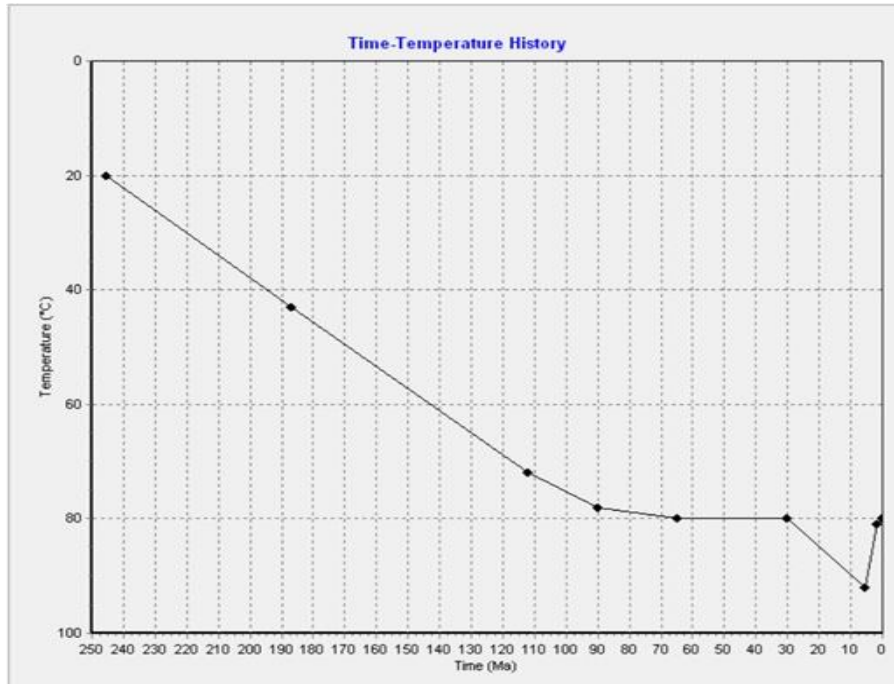


Fig. A8. Thermal history of the well A_UT 1866.7. Ketcham et al., 2007a and Laslett et al., 1987 equations have been used to determine AFT ages and Farley, 2000 and Flowers et al., 2009 equations have been used to determine AHe ages.

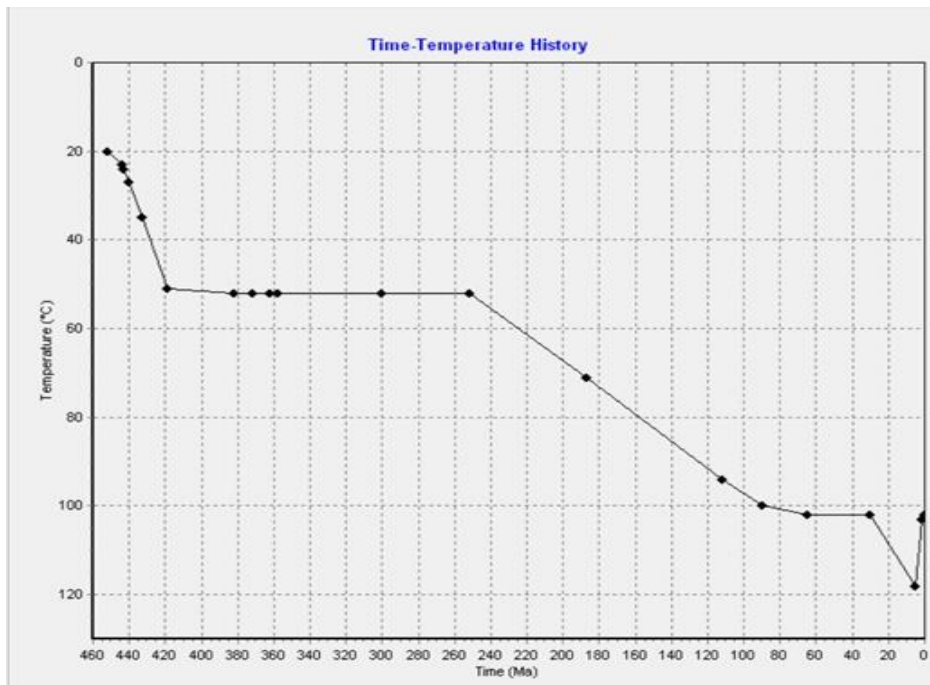


Fig. A9. Thermal history of the well A_UT 2627.5. Ketcham et al., 2007a and Laslett et al., 1987 equations have been used to determine AFT ages and Farley, 2000 and Flowers et al., 2009 equations have been used to determine AHe ages.

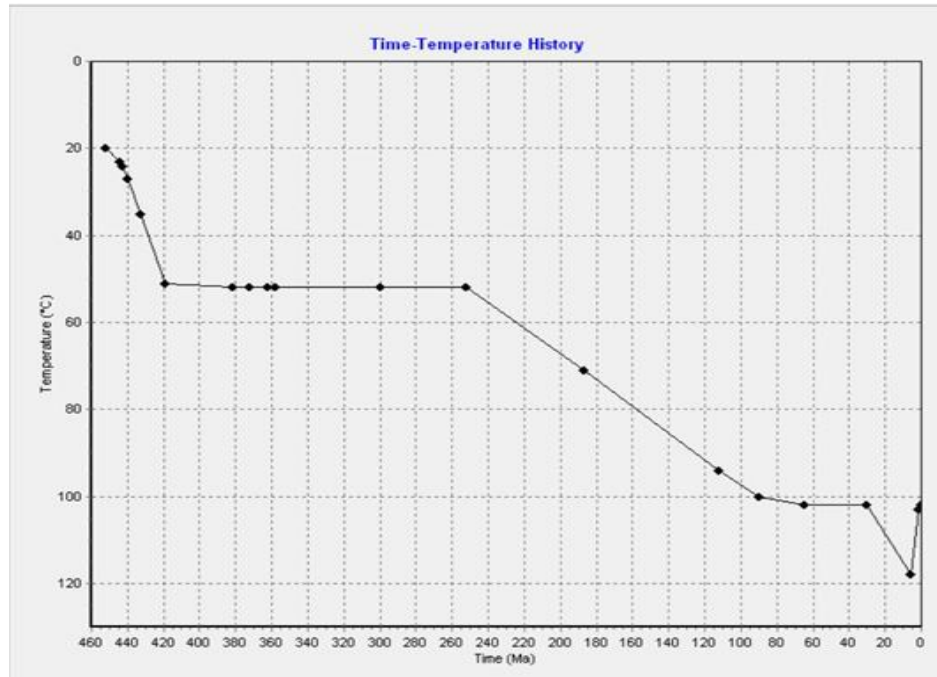


Fig. A10. Thermal history of the well A_UT 2628.3. Ketcham et al., 2007a and Laslett et al., 1987 equations have been used to determine AFT ages and Farley, 2000 and Flowers et al., 2009 equations have been used to determine AHe ages.

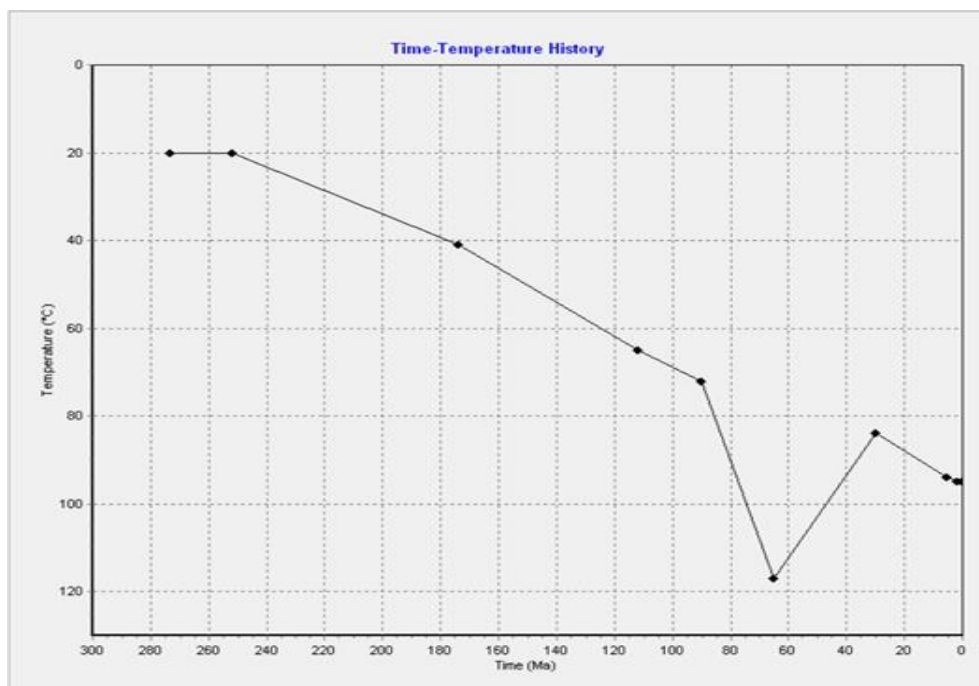


Fig. A11. Thermal history of the well BR_LT 2793.8. Ketcham et al., 2007a and Laslett et al., 1987 equations have been used to determine AFT ages and Farley, 2000 and Flowers et al., 2009 equations have been used to determine AHe ages.

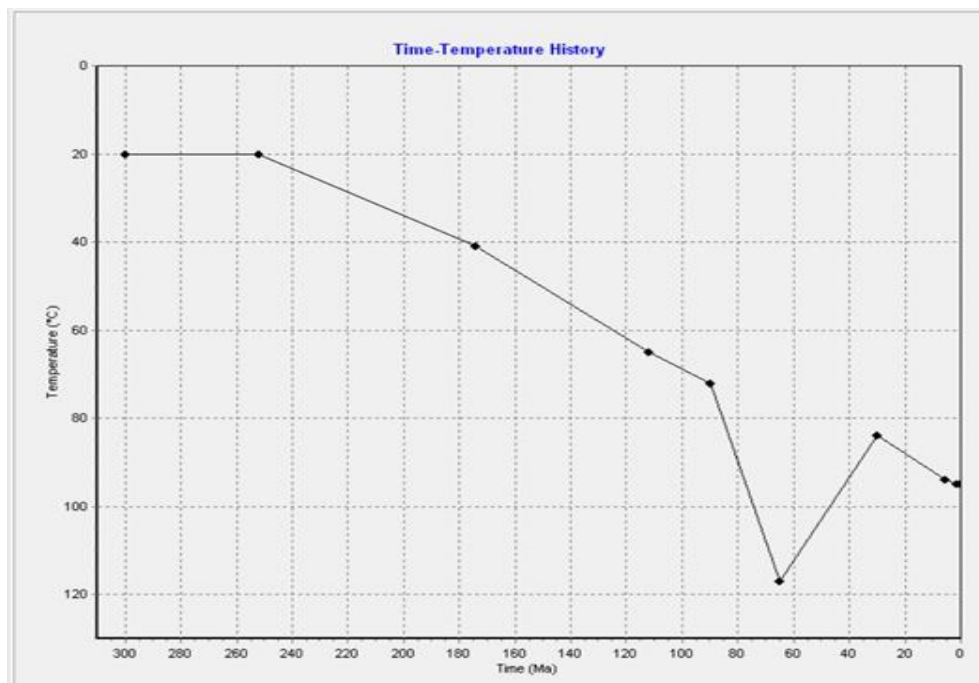


Fig. A12. Thermal history of the well BR_LT 2796. Ketcham et al., 2007a and Laslett et al., 1987 equations have been used to determine AFT ages and Farley, 2000 and Flowers et al., 2009 equations have been used to determine AHe ages.



Fig. A13. Thermal history of the well BR_LT 2800. Ketcham et al., 2007a and Laslett et al., 1987 equations have been used to determine AFT ages and Farley, 2000 and Flowers et al., 2009 equations have been used to determine AHe ages.

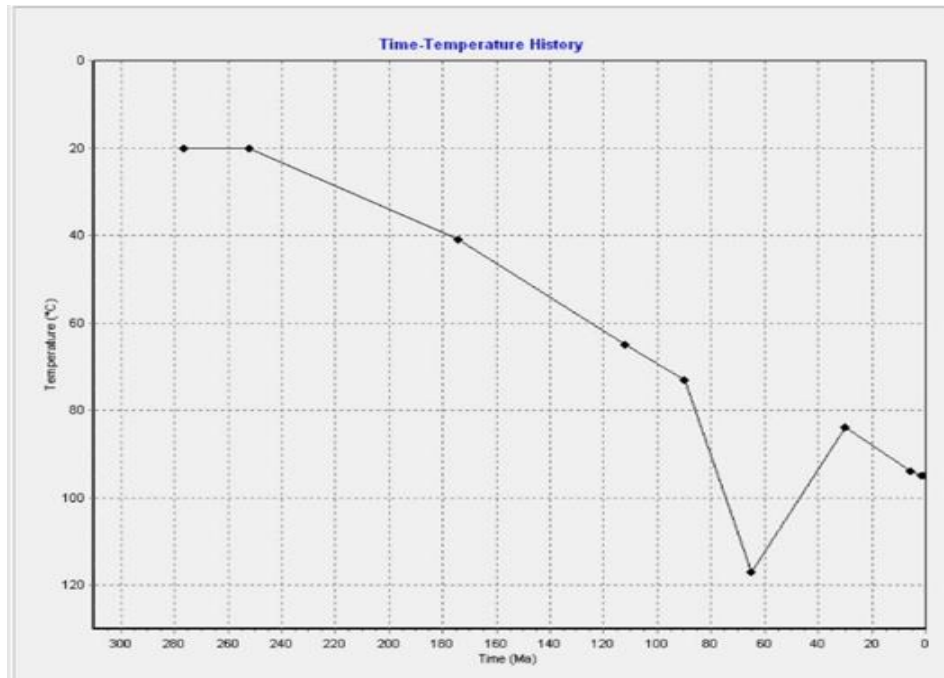


Fig. A14. Thermal history of the well BR_LT 2801.7. Ketcham et al., 2007a and Laslett et al., 1987 equations have been used to determine AFT ages and Farley, 2000 and Flowers et al., 2009 equations have been used to determine AHe ages.

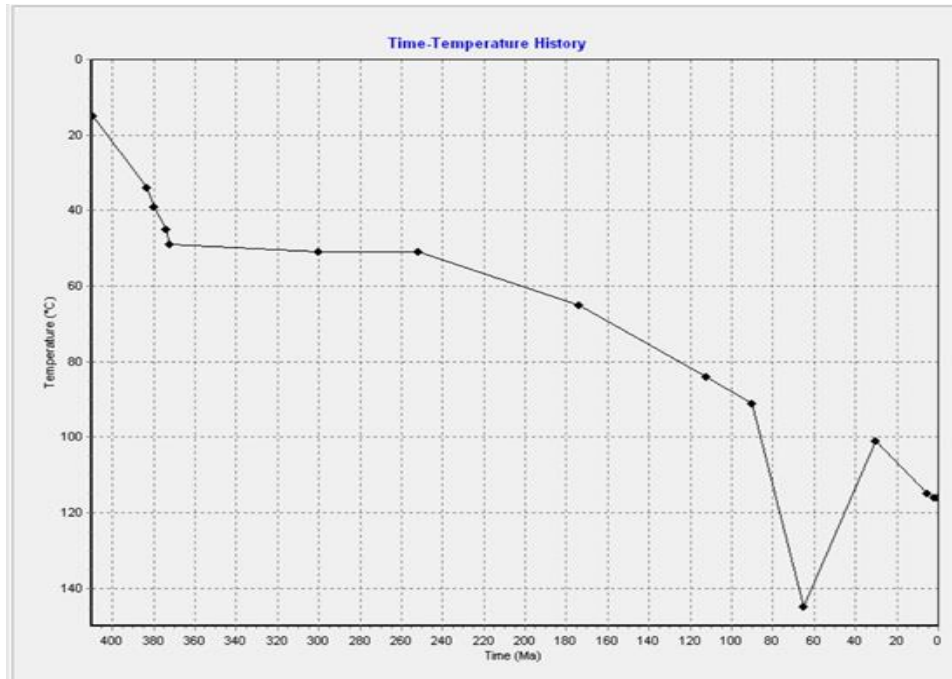


Fig. A15. Thermal history of the well BR_LT 3616.1. Ketcham et al., 2007a and Laslett et al., 1987 equations have been used to determine AFT ages and Farley, 2000 and Flowers et al., 2009 equations have been used to determine AHe ages.

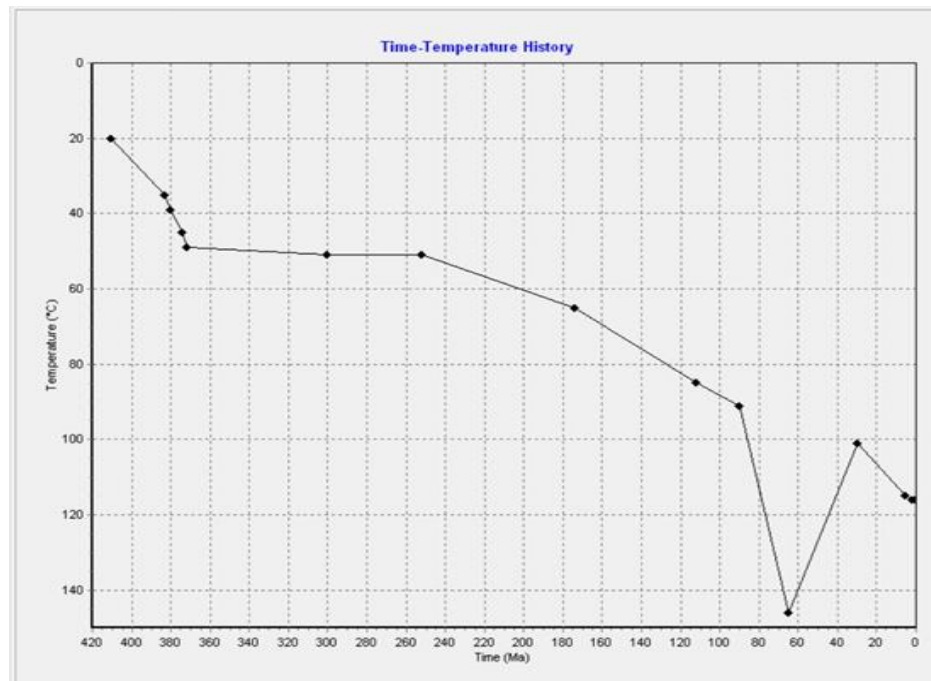


Fig. A16. Thermal history of the well BR_LT 3627.2. Ketcham et al., 2007a and Laslett et al., 1987 equations have been used to determine AFT ages and Farley, 2000 and Flowers et al., 2009 equations have been used to determine AHe ages.

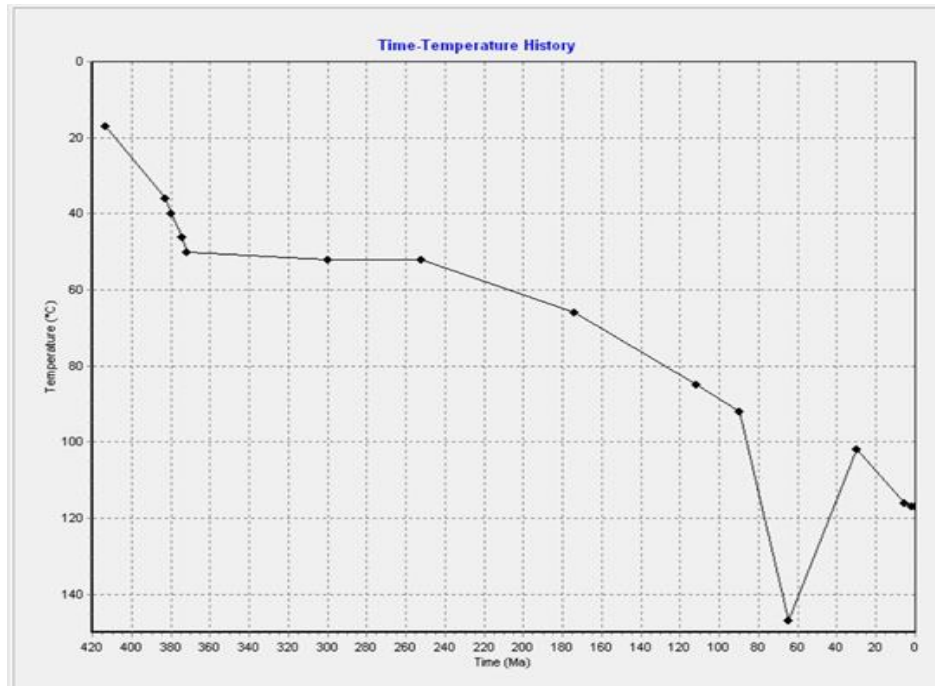


Fig. A17. Thermal history of the well BR_LT 3656.1. Ketcham et al., 2007a and Laslett et al., 1987 equations have been used to determine AFT ages and Farley, 2000 and Flowers et al., 2009 equations have been used to determine AHe ages.

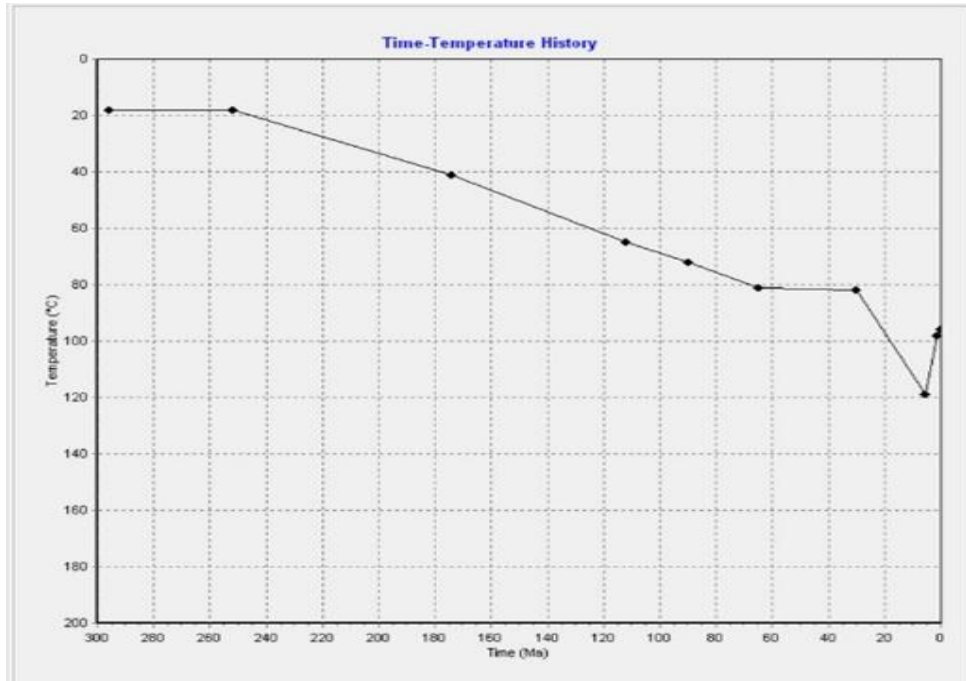


Fig. A18. Thermal history of the well BR_UT 2793.8. Ketcham et al., 2007a and Laslett et al., 1987 equations have been used to determine AFT ages and Farley, 2000 and Flowers et al., 2009 equations have been used to determine AHe ages.

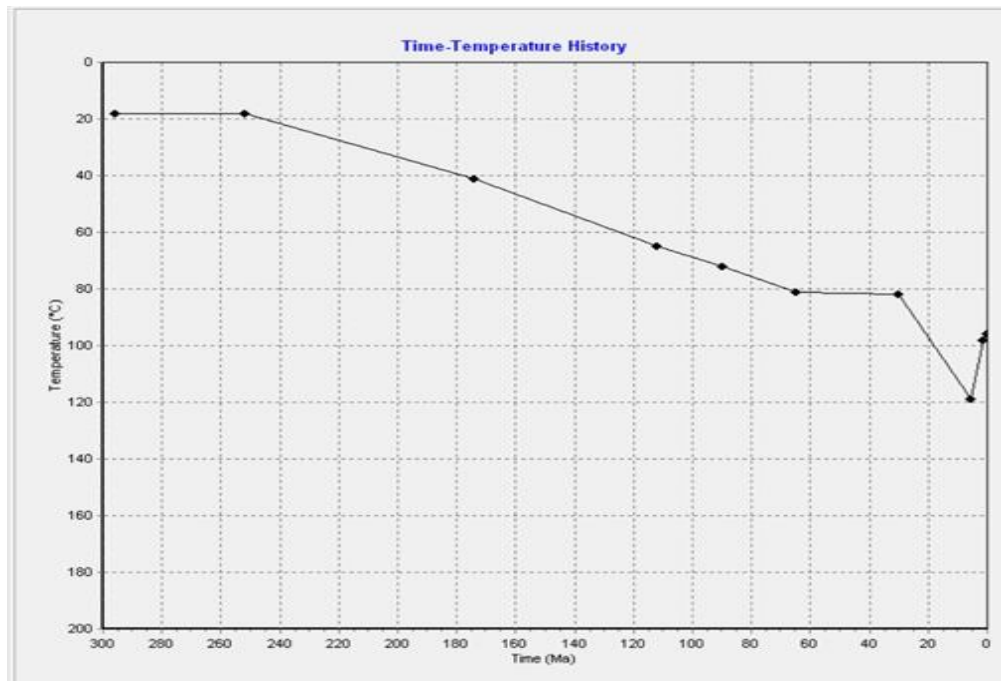


Fig. A19. Thermal history of the well BR_UT 2796. Ketcham et al., 2007a and Laslett et al., 1987 equations have been used to determine AFT ages and Farley, 2000 and Flowers et al., 2009 equations have been used to determine AHe ages.

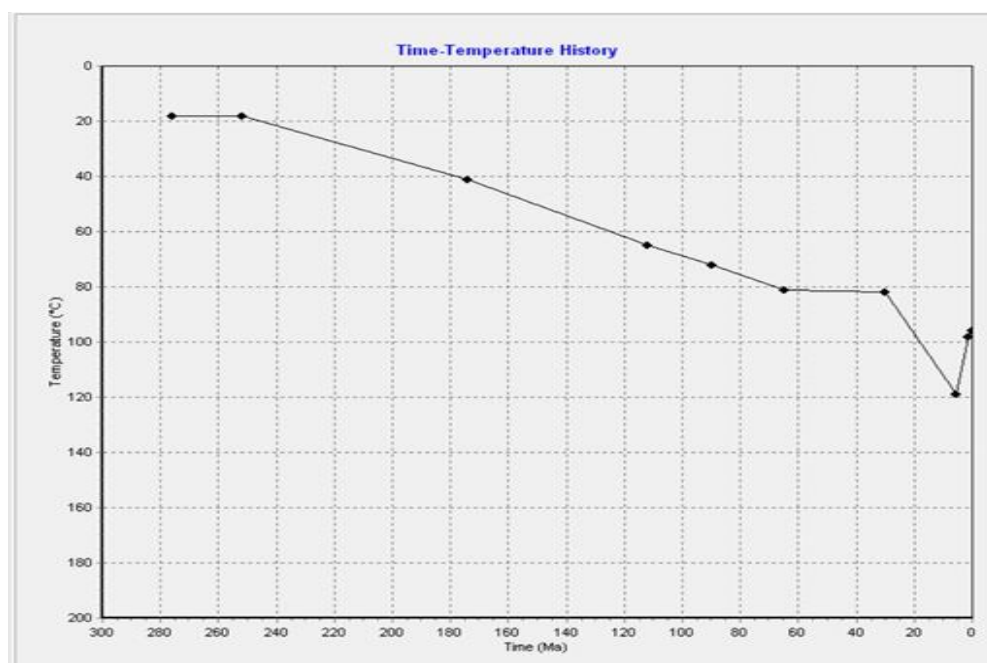


Fig. A20. Thermal history of the well BR_UT 2800. Ketcham et al., 2007a and Laslett et al., 1987 equations have been used to determine AFT ages and Farley, 2000 and Flowers et al., 2009 equations have been used to determine AHe ages.

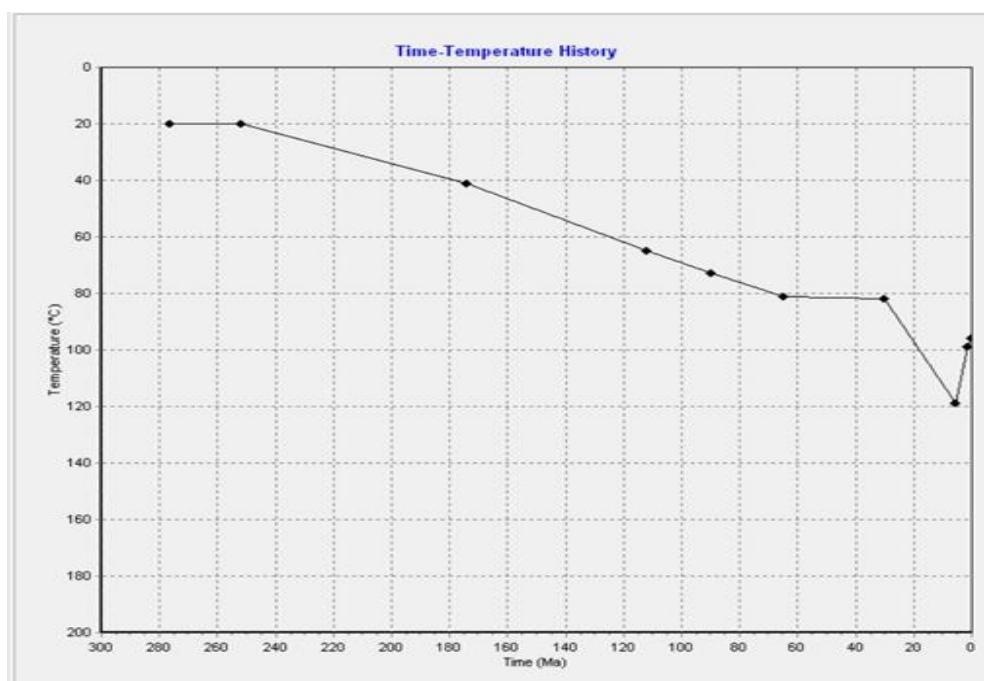


Fig. A21. Thermal history of the well BR_UT 2801.7. Ketcham et al., 2007a and Laslett et al., 1987 equations have been used to determine AFT ages and Farley, 2000 and Flowers et al., 2009 equations have been used to determine AHe ages.

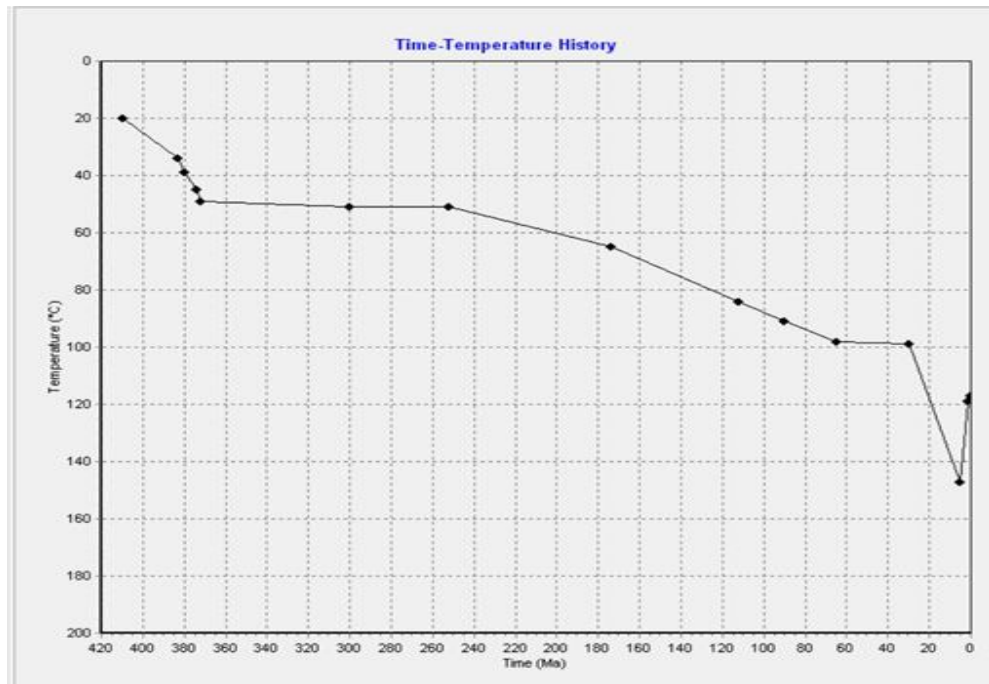


Fig. A22. Thermal history of the well BR_UT 3616.1. Ketcham et al., 2007a and Laslett et al., 1987 equations have been used to determine AFT ages and Farley, 2000 and Flowers et al., 2009 equations have been used to determine AHe ages.

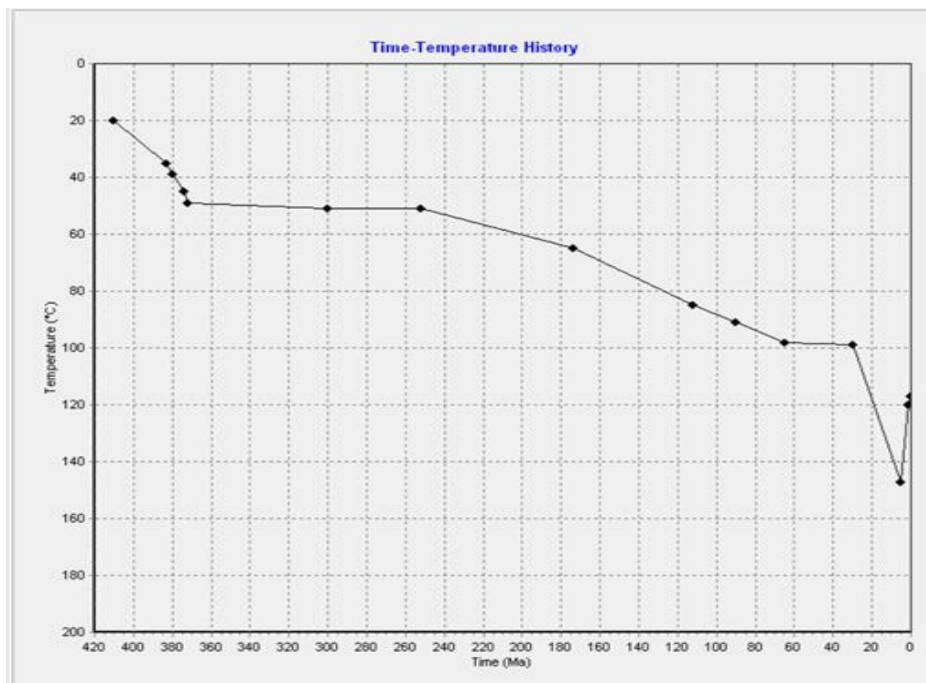


Fig. A23. Thermal history of the well BR_UT 3627.3. Ketcham et al., 2007a and Laslett et al., 1987 equations have been used to determine AFT ages and Farley, 2000 and Flowers et al., 2009 equations have been used to determine AHe ages.

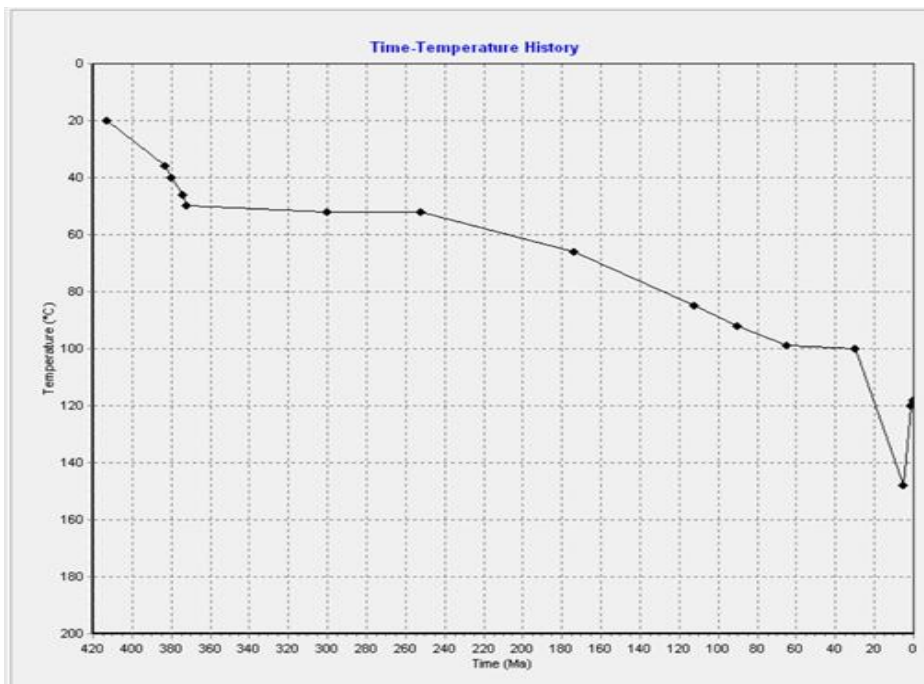


Fig. A24. Thermal history of the well BR_UT 3656.1. Ketcham et al., 2007a and Laslett et al., 1987 equations have been used to determine AFT ages and Farley, 2000 and Flowers et al., 2009 equations have been used to determine AHe ages.

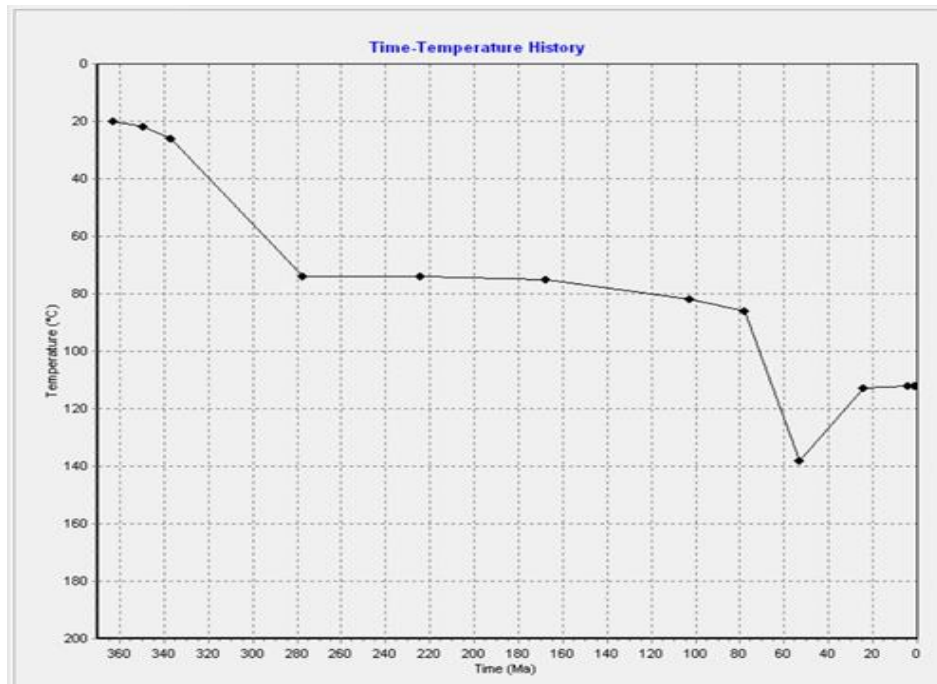


Fig. A25. Thermal history of the well NC_LT 1913. Ketcham et al., 2007a and Laslett et al., 1987 equations have been used to determine AFT ages and Farley, 2000 and Flowers et al., 2009 equations have been used to determine AHe ages.

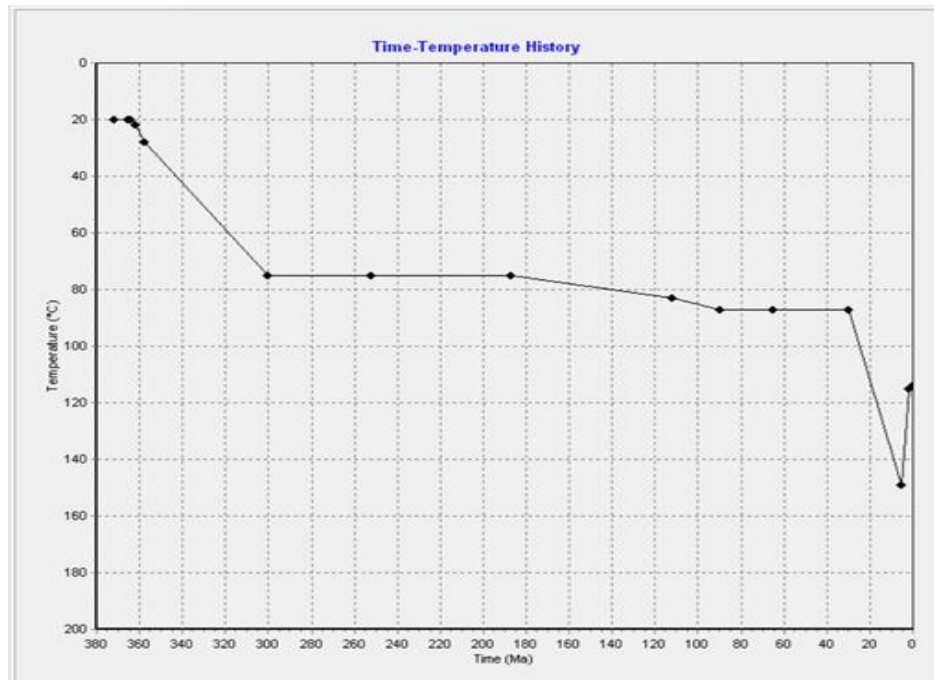


Fig. A26. Thermal history of the well NC_LT 1941. Ketcham et al., 2007a and Laslett et al., 1987 equations have been used to determine AFT ages and Farley, 2000 and Flowers et al., 2009 equations have been used to determine AHe ages.

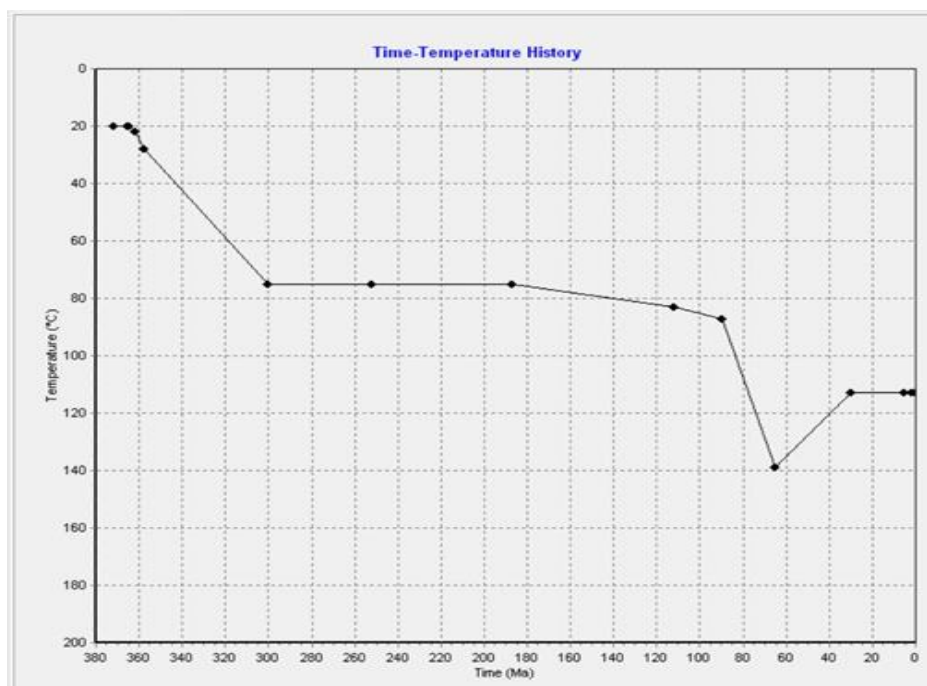


Fig. A27. Thermal history of the well NC_LT 1958. Ketcham et al., 2007a and Laslett et al., 1987 equations have been used to determine AFT ages and Farley, 2000 and Flowers et al., 2009 equations have been used to determine AHe ages.

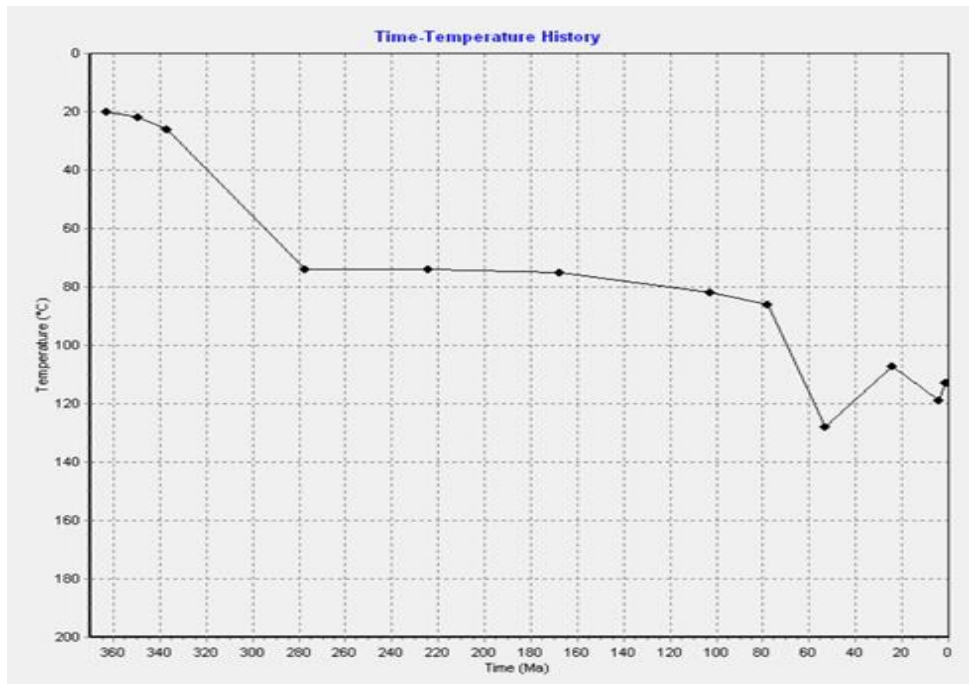


Fig. A28. Thermal history of the well NC_UT 1913. Ketcham et al., 2007a and Laslett et al., 1987 equations have been used to determine AFT ages and Farley, 2000 and Flowers et al., 2009 equations have been used to determine AHe ages.

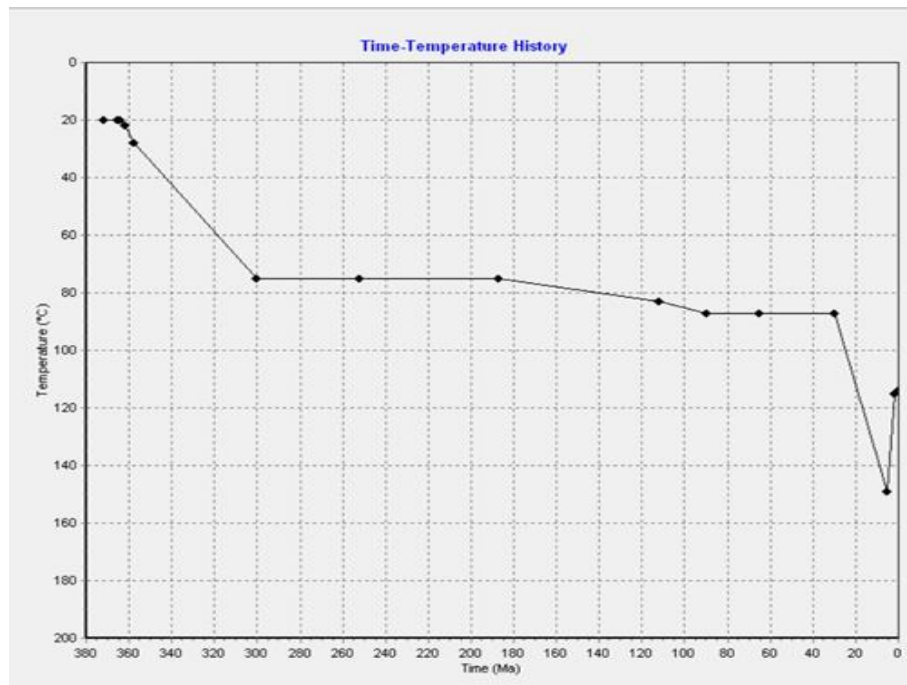


Fig. A29. Thermal history of the well NC_UT 1941. Ketcham et al., 2007a and Laslett et al., 1987 equations have been used to determine AFT ages and Farley, 2000 and Flowers et al., 2009 equations have been used to determine AHe ages.

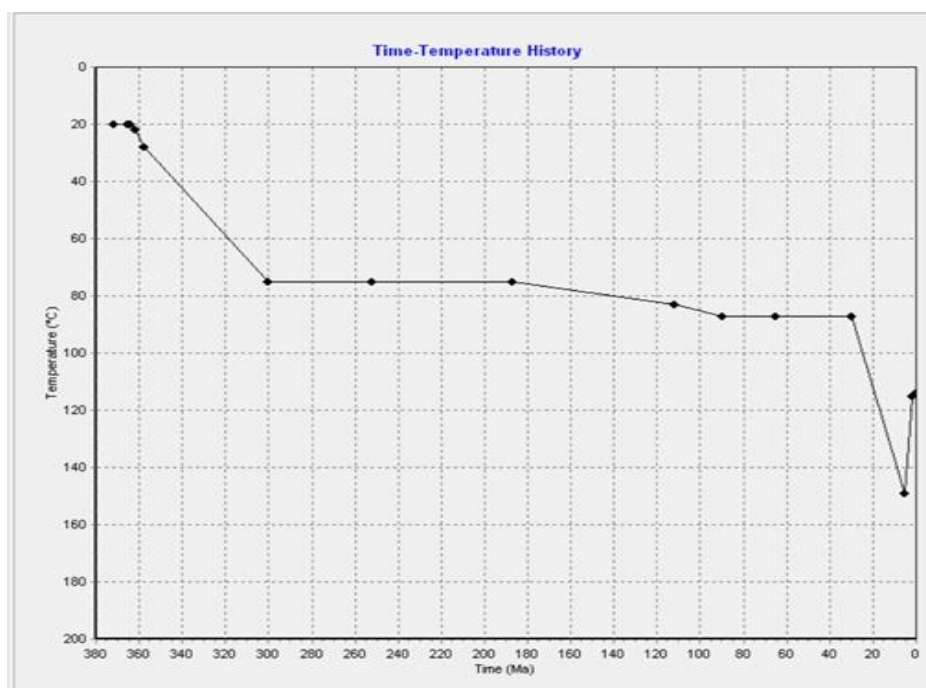


Fig. A30. Thermal history of the well NC_UT 1958. Ketcham et al., 2007a and Laslett et al., 1987 equations have been used to determine AFT ages and Farley, 2000 and Flowers et al., 2009 equations have been used to determine AHe ages.

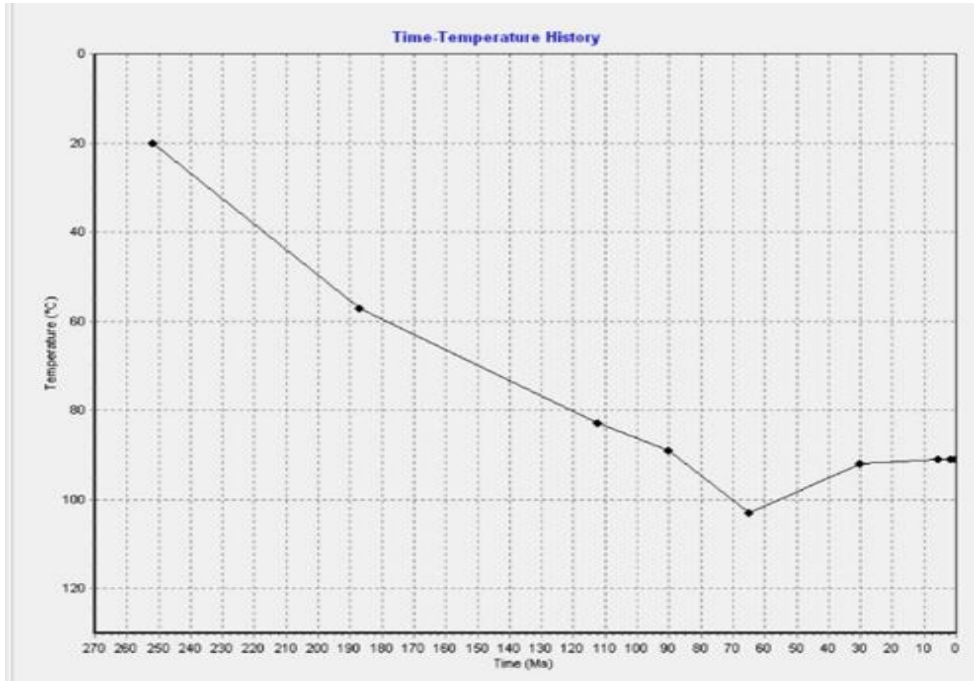


Fig. A31. Thermal history of the well A_LT 2229.6-2240.7. Ketcham et al., 2007a and Laslett et al., 1987 equations have been used to determine AFT ages and Farley, 2000 and Flowers et al., 2009 equations have been used to determine AHe ages.

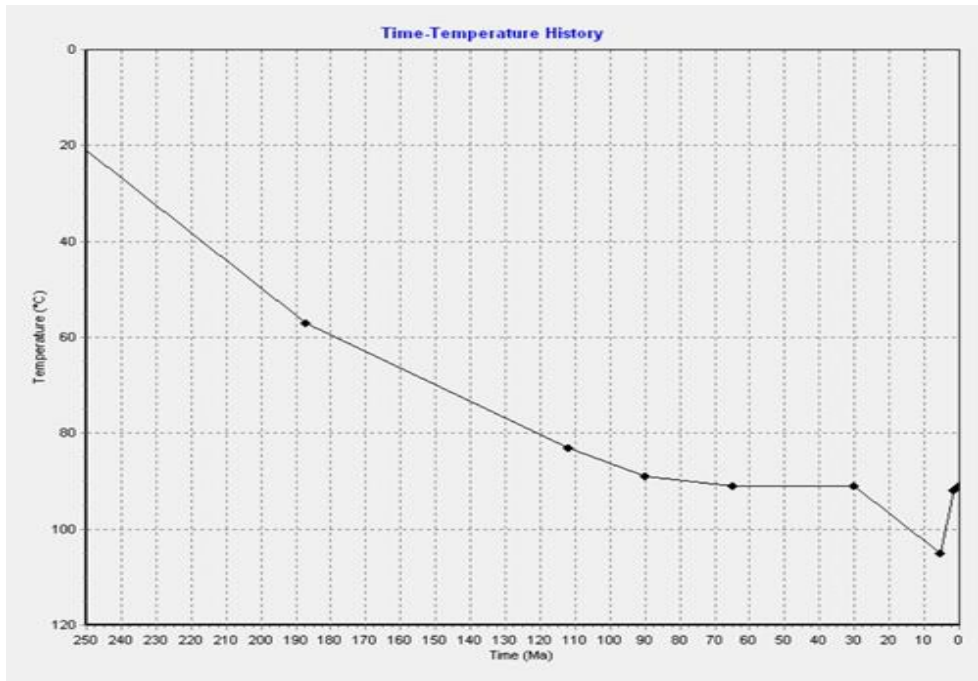


Fig. A32. Thermal history of the well A_UT 2229.6-2240.7. Ketcham et al., 2007a and Laslett et al., 1987 equations have been used to determine AFT ages and Farley, 2000 and Flowers et al., 2009 equations have been used to determine AHe ages.

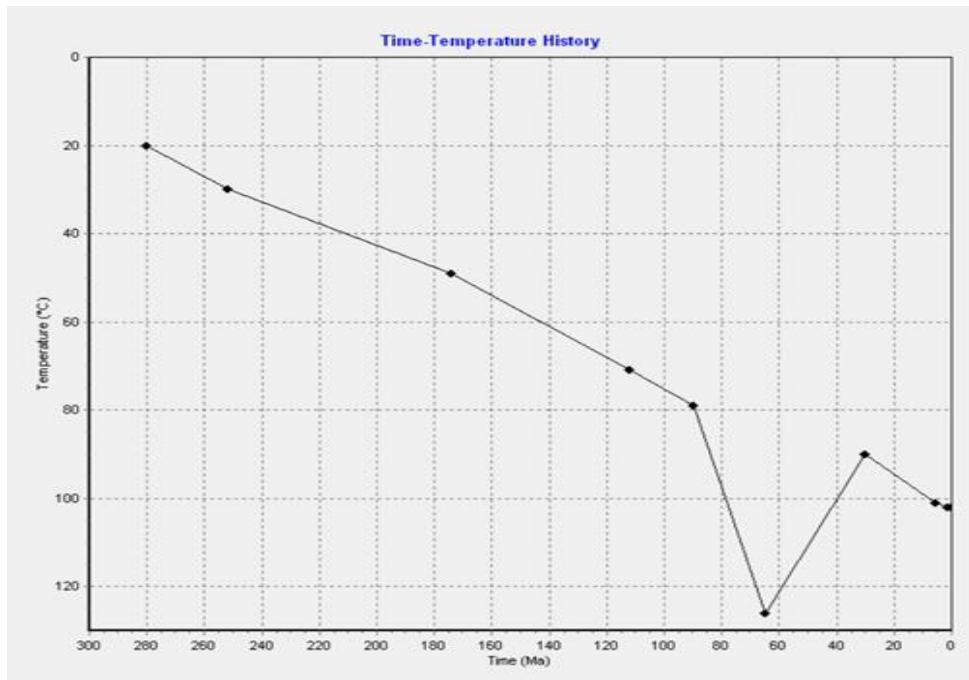


Fig. A33. Thermal history of the well BR_LT 3014. Ketcham et al., 2007a and Laslett et al., 1987 equations have been used to determine AFT ages and Farley, 2000 and Flowers et al., 2009 equations have been used to determine AHe ages.

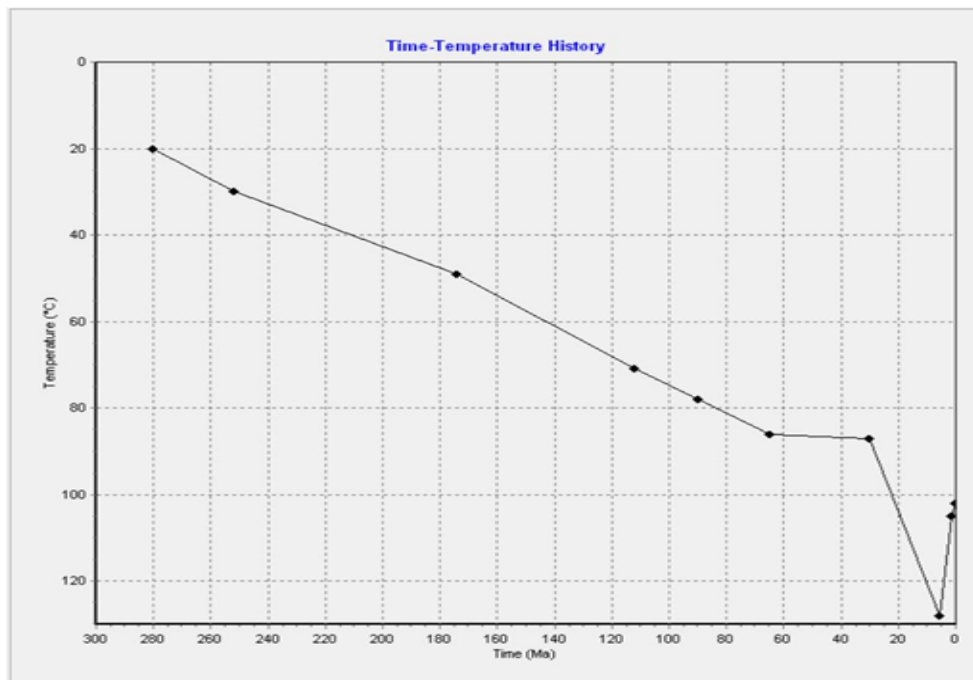


Fig. A34. Thermal history of the well BR-1_UT 3014. Ketcham et al., 2007a and Laslett et al., 1987 equations have been used to determine AFT ages and Farley, 2000 and Flowers et al., 2009 equations have been used to determine AHe ages.

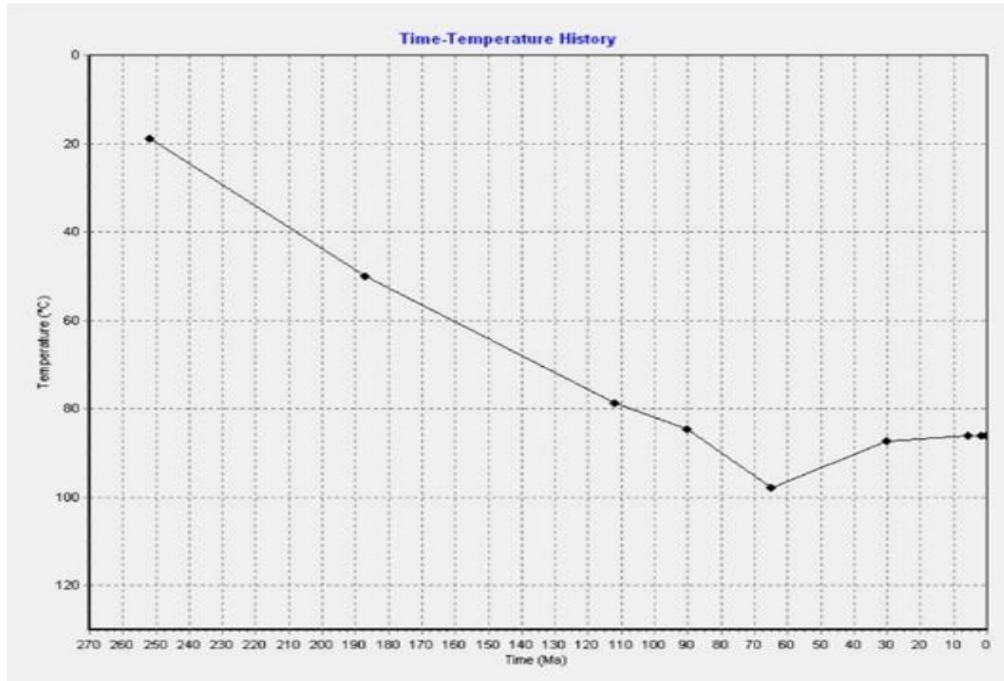


Fig. A35. Thermal history of the well A_LT 2229.6-2240.7 with temperature reduced of the 5%. Ketcham et al., 2007a and Laslett et al., 1987 equations have been used to determine AFT ages and Farley, 2000 and Flowers et al., 2009 equations have been used to determine AHe ages.

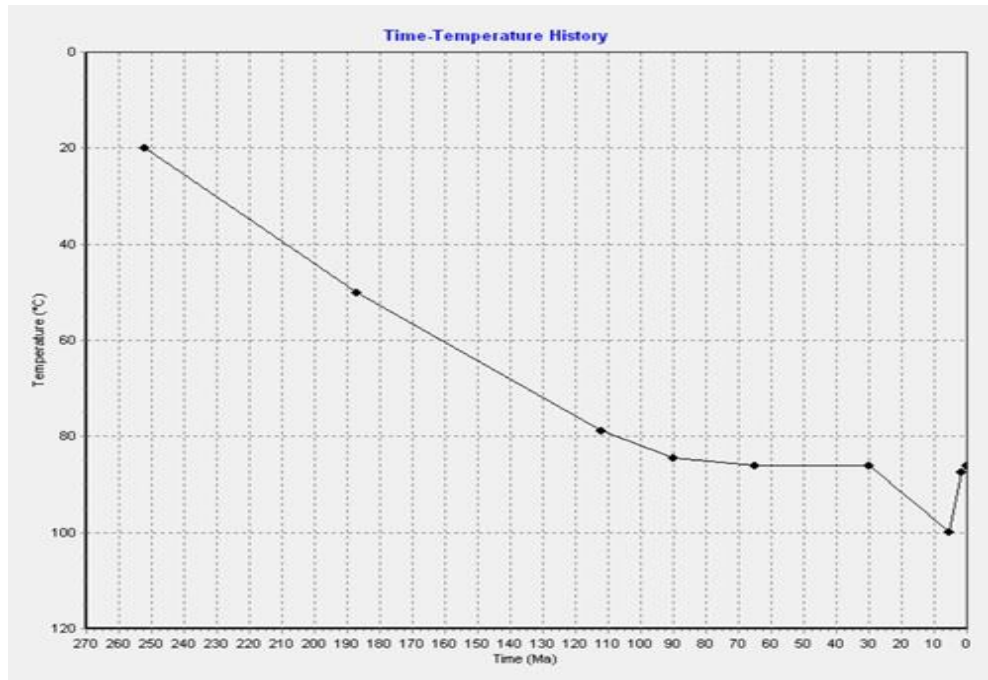


Fig. A36. Thermal history of the well A_UT 2229.6-2240.7 with temperature reduced of the 5%. Ketcham et al., 2007a and Laslett et al., 1987 equations have been used to determine AFT ages and Farley, 2000 and Flowers et al., 2009 equations have been used to determine AHe ages.



Fig. A37. Thermal history of the well BR_LT 3014 with temperature reduced of the 5%. Ketcham et al., 2007a and Laslett et al., 1987 equations have been used to determine AFT ages and Farley, 2000 and Flowers et al., 2009 equations have been used to determine AHe ages.

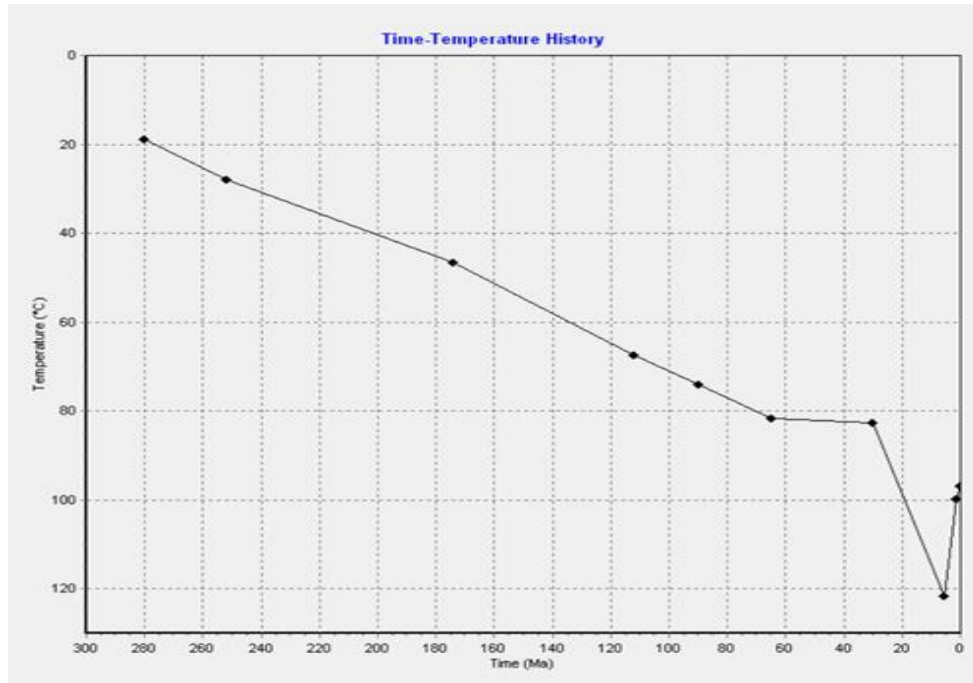


Fig. A38. Thermal history of the well BR_UT 3014 with temperature reduced of the 5%. Ketcham et al., 2007a and Laslett et al., 1987 equations have been used to determine AFT ages and Farley, 2000 and Flowers et al., 2009 equations have been used to determine AHe ages.